The Henryk Niewodniczański
INSTITUTE OF NUCLEAR PHYSICS
Polish Academy of Sciences
152 Radzikowskiego Str., 31-342 Kraków, Poland

www.ifj.edu.pl/publ/reports/2006

Kraków, December 2006

Report No. 1983/PH

Transverse Momentum Distributions of Charged Particles in Nuclear Collisions at RHIC Energies

Adam Trzupek

Habilitation Thesis

Abstract

The paper reports on measurements of the transverse momentum distributions of produced particles from nuclear collisions at the highest center-of-mass energies provided by the Relativistic Heavy Ion Collider (RHIC). The transverse momentum spectra of charged hadrons produced in d+Au and Au+Au collisions at the top RHIC energy of 200 GeV in the nucleon-nucleon center-of-mass system are presented. For the Au+Au system, the measurements at the lower energy of 62.4 GeV are also reported. The analyzed data were collected by the PHOBOS experiment during several RHIC data-taking runs from 2001 to 2004.

The main emphasis of this paper is the measurement of particle production at very low transverse momenta, a possibility uniquely available to the PHOBOS detector. A new non-standard method was developed to extract yields of $(\pi^+ + \pi^-)$, $(K^+ + K^-)$ and $(p+\overline{p})$ at the lowest transverse momentum values accessible at RHIC. The results do not confirm the prediction of a significant enhancement in particle production at very low $p_{_T}$. The flattening of proton and antiproton $p_{_T}$ spectra, consistent with the expectations of transverse expansion of the system, is clearly observed down to very low $p_{_T}$. In contrast to Au+Au collisions, such a flattening is not observed in yields of d+Au collisions at $\sqrt{s_{_{NN}}} = 200\ GeV$. The scaling properties of $m_{_T}$ spectra in Au+Au and d+Au collisions, as well as particle ratios, are discussed.

Results obtained from the analysis of the transverse momentum distributions clearly show that the matter produced in nuclear collisions at RHIC energies is strongly coupled and undergoes a rapid transverse expansion. Comparison to the predictions of different models aiming to describe particle production in ultra-relativistic nuclear collisions is discussed.

The characteristics of the system derived from this study of the transverse momentum distributions has provided a significant contribution to the RHIC discovery of a new state of matter, a strongly coupled Quark-Gluon Plasma, with properties resembling those of a perfect fluid. Due to the importance of this discovery the discussion of the properties of this new state of matter, inferred from results other than transverse momentum measurements, is also included.

Contents

Chapter 1

Introduction

The main goal of heavy-ion collisions at relativistic energies is to produce a hot and dense medium at an energy density greater than 1 GeV/fm^3. It is expected that in such extreme conditions a new state of matter, the Quark-Gluon Plasma (QGP), can be formed, consisting of deconfined quarks, antiquarks and gluons with partially restored chiral symmetry [1]. Exploring properties of the created medium is crucial for understanding the physics of dense systems. Evolution models of the universe assert that the whole matter was in the QGP state about 10 μs after the Big Bang, and such systems may also be present in the core of neutron stars.

The Relativistic Heavy Ion Collider (RHIC) at Brookhaven National Laboratory (BNL) is primarily devoted to the study of heavy-ion collisions. Since the first successful acceleration of gold (Au) ions in the year 2000, RHIC gives a unique opportunity to study matter at the highest energy density ever produced in the laboratory. At RHIC, gold ions are collided at the nucleon-nucleon center-of-mass energy of $\sqrt{s_{NN}} = 200\ GeV$, more than an order of magnitude larger than the corresponding energy obtained in the fixed target experiments at the Alternating Gradient Synchrotron (AGS-BNL) and Super Proton Synchrotron (SPS-CERN). A conservative estimate implies that for the most central Au+Au collisions at RHIC the energy density in the collision system is $\epsilon > 3\ GeV/fm^3$ [2] and by far exceeds the critical energy density needed for QGP formation. Four detectors were built at RHIC to study the relativistic heavy-ion collisions in this new energy regime: PHOBOS [3], BRAHMS [4], PHENIX [5] and STAR [6]. The PHOBOS experiment was designed to measure the density of charged particles within almost the full solid angle as well as charged particle spectra near mid-rapidity in a wide range of transverse momentum, from 0.03 GeV/c up to about 5 GeV/c. This report presents measurements of charged hadron transverse momentum (p_T) spectra, obtained using the PHOBOS detector.

The large collision energy available at RHIC allowed, for the first time, to explore the physics of a hot and dense medium through hard partonic scatter-

ings which probe initial/final state effects involved in production of particles with large transverse momenta ($p_T > 5\ GeV/c$). RHIC results on the suppression of high-p_T spectra [7–14] provide direct evidence that in central Au+Au collisions at the highest RHIC energy a new strongly coupled state of matter is formed. Other RHIC results, for example the suppression of the away-side azimuthal correlations of high-p_T particles [15–18] and the strong elliptic flow [18–23], were found consistent with this observation. The experimental data provide convincing evidence that the created medium does not behave like a non- or weakly interacting gas of quarks, antiquarks and gluons (wQGP), as was commonly expected before the RHIC era, but it constitutes a strongly coupled plasma (sQGP) with properties of almost perfect fluid [24, 25].

The measurements of particle spectra at very low p_T provide additional important information on the characteristics of the new state of matter. Studying the particle production at very low transverse momenta ($p_T < 0.2\ GeV/c$) is particularly interesting as the ultra-soft p_T region is associated with long-distance scales accessible only in heavy-ion collisions [26]. Before the RHIC era, it was predicted that the expansion of a weakly interacting system should result in an enhanced production of low-p_T particles. For example, an excess of low-p_T pions could be present if the dense medium produced in heavy-ion collisions behaves like a weakly interacting gas of quarks, antiquarks and gluons and significantly expands and cools before hadronization. Due to the large size of the system before it freezes out, a relatively large number of low-p_T particles could be produced. To study the low-p_T physics, the transverse momentum distributions of charged particles in nuclear collisions were measured with the PHOBOS detector at mid-rapidity in the p_T range 30 to 50 MeV/c for charged pions, 90 to 130 MeV/c for charged kaons and 140 to 210 MeV/c for protons and antiprotons. At RHIC, only the PHOBOS experiment has measured particles at such low transverse momenta. The invariant p_T spectra at very low transverse momenta in Au+Au collisions at $\sqrt{s_{NN}} = 200\ GeV$ [27–29] and 62.4 GeV [30, 31] and in d+Au collisions at $\sqrt{s_{NN}} = 200\ GeV$ [30] were obtained. In central Au+Au collisions, at both 62.4 and 200 GeV, no significant enhancement in particle production at low transverse momentum was found. The results have provided additional indirect evidence that the new state of matter is strongly coupled. The observation that there is no such excess in production of low-p_T particles could be a manifestation of the high level of interactions present in the system. Large pressure gradients, e.g. blast wave, can accelerate low-p_T particles. Also, the production of heavier particles in Au+Au collisions is expected to be modified at low-p_T due to the presence of a collective transverse expansion of the system [32, 33]. Indeed, flattening of proton and antiproton p_T spectra, consistent with the pre-RHIC expectations, is clearly observed down to very low p_T. In contrast to Au+Au collisions, such a flattening is not observed in very low and intermediate transverse momentum particle yields measured in d+Au collisions at $\sqrt{s_{NN}} = 200\ GeV$.

Author's contribution: Since 1992, I have had an opportunity to participate in the international PHOBOS project. As a member of the PHOBOS Collaboration, I was involved in the detector design, preparation of the letter of intent and the proposal of the PHOBOS experiment. Since the beginning of detector construction until now (1994-2006), I have been solely responsible for preparation, implementation and management of the geometrical description of the PHOBOS detector. This geometrical description, has been used in the data processing chain, including on-line data taking, reconstruction procedures and physical analyses as well as in the full Monte Carlo detector simulations.

My main physics interest has focused on the production of particles with very low transverse momenta. I have developed a new method for the reconstruction and identification of low momentum particles. It has to be noted that the low-$p_{_T}$ particle production was the main objective of the PHOBOS experiment which could be achieved due to the unique design of the detector. This objective has been successfully completed. The transverse momentum spectra of $(\pi^+ + \pi^-)$, $(K^+ + K^-)$ and $(p + \overline{p})$ at very low $p_{_T}$ in d+Au and Au+Au collisions at the top RHIC energy of 200 GeV were obtained using this new reconstruction method. For the Au+Au system at the lower energy of 62.4 GeV the $p_{_T}$ spectra were also measured. The new physical results have already been published [2, 27, 31] and presented at conferences [28–30, 34]. The reconstruction method, I have developed, is now used in several ongoing analyses focusing on systematic properties of low-$p_{_T}$ particles yields like their dependence on energy, collision centrality or system size.

Thesis outline: The physics motivations for relativistic heavy-ion collisions are presented in Chapter 2. The properties of Quark-Gluon Plasma and its experimental signatures are reviewed. A brief summary of results obtained before the RHIC era including data from both the AGS and SPS experiments is presented in Chapter 3. The RHIC complex is described in Chapter 4. The PHOBOS detector layout and its experimental capabilities are described in Chapter 5. A detailed technical description of the new method for measurement of particles at very low $p_{_T}$ in the PHOBOS experiment is presented in Chapter 6. For completeness the measurements of identified particles at intermediate momenta as well as (unidentified) high-$p_{_T}$ charged hadron yields are also included. The main physics results on the invariant momentum spectra, in the full $p_{_T}$ range of the PHOBOS experiment, are shown in Chapter 7. Some interesting properties of the medium produced in central Au+Au collisions inferred from the particle momenta distributions are discussed in this Chapter. The general characteristics of the medium formed in Au+Au collisions are given in Chapter 8. The summary and conclusions are presented in Chapter 9. Details on systematic error analysis of low-$p_{_T}$ particle yields are given in Appendix A while invariant inclusive $p_{_T}$ spectra at very low transverse momentum are presented in tabular form in Appendix B.

Chapter 2

Quantum Chromodynamics and Ultra-Relativistic Heavy-Ion Collisions

Measurements performed in experiments of relativistic heavy-ion collisions provide crucial data for a better understanding of the physics of dense and hot matter. Relying on Quantum Chromodynamics (QCD), the well established theory of strong interactions, new phenomena were predicted to occur in the dense system produced in nuclear collisions. Basic properties of QCD like asymptotic freedom, confinement, chiral symmetry breaking and formation of Quark-Gluon Plasma are reviewed in this Chapter. Selected experimental signatures of QGP in relativistic heavy-ion collisions are also presented.

2.1 Quantum Chromodynamics Lagrangian

The basic ingredients of QCD are quark and gluon fields. The large number of elementary particles, discovered in the last century, led physicists to formulate a successful model in which all hadrons (mesons and baryons) are built from quarks and gluons, also called partons [35]. Six different quark types, called flavors, have been observed to date. Quarks in hadrons are bound by exchanges of intermediate bosons, called gluons. Quarks and gluons carry a "strong charge", called color, which is a source of strong interactions between partons. There are three/eight color states of quarks/gluons and a net neutral color charge for each hadron.

Strong interactions between partons are described by the Quantum Chromodynamics Lagrangian (in units $\hbar = c = 1$) [36]:

$$\mathcal{L}_{QCD} = \sum_j \bar{q}_j^k (i\gamma^\mu (D_\mu)_{kl} - m_j \delta_{kl}) q_j^l - \frac{1}{4} F_{\mu\nu}^a F_a^{\mu\nu}, \tag{2.1}$$

where q_j^k denotes the quark field of flavor j, mass m_j and color state k while γ^μ are the Dirac matrices. The covariant derivative D_μ is:

$$(D_\mu)_{kl} = \delta_{kl}\partial_\mu + ig\sum_a A_\mu^a \frac{(\lambda^a)_{kl}}{2}, \tag{2.2}$$

where A_μ^a represents eight gluon fields and g is the coupling constant of the theory. λ^a are the eight 3×3 Gell-Mann matrices. The colored matrices obey *non-Abelian* commutation relations $[\lambda_a, \lambda_b] = if_{abc}\lambda_c$ where f_{abc} are the structure constants of $\mathrm{SU}_c(3)$ group. The gluon field strength tensor $F_{\mu\nu}^a$ is defined in the following way:

$$F_{\mu\nu}^a = \partial_\mu A_\nu^a - \partial_\nu A_\mu^a - g f_{abc} A_\mu^b A_\nu^c. \tag{2.3}$$

The QCD Lagrangian is invariant under local $\mathrm{SU}_c(3)$ gauge transformations. It is interesting to note that due to this constraint gluons must be massless as a term m^2AA breaks this symmetry. One can also see from Eq. 2.1, that the QCD Lagrangian does not contain flavor changing interactions. As a result, quark flavors are conserved.

Once the QCD Lagrangian is known, partonic systems, like nucleons can be studied by means of Feynman's path integrals [37]. However, evaluation of the integrals turned out to be very difficult due to the *non-Abelian* structure of the theory. Presently available analytical methods are not sufficient. In order to study properties of systems composed from strongly interacting quarks and gluons, a QCD lattice gauge theory was developed [38, 39]. In this approach the QCD Lagrangian is formulated on a discrete space-time lattice of spacing a. Physical observables are computed by evaluating path integrals on the lattice with Euclidean signature ($t \rightarrow i\ t$), using Monte Carlo techniques. Physical results are found in the limit when $a \rightarrow\ 0$. The path integrals technique can also be used to compute the partition function which encodes the properties of a partonic system in thermodynamical equilibrium, like energy density, pressure or entropy. Usually, it is assumed that this partonic system reproduces the high density medium produced in the relativistic heavy-ion collisions.

2.2 Asymptotic Freedom, Confinement and Chiral Symmetry Breaking

The last terms of Eqs 2.2 and 2.3 imply that in QCD quark-gluon and gluon-gluon interactions are possible. This feature of QCD has important consequences on parton interactions as the vacuum polarization induced by a single quark can have a contribution from gluons in addition to $q\bar{q}$ pairs. While the polarization of $q\bar{q}$ pairs partially cancels out the quark field at some finite distance (called the screening effect) the contribution from gluons is opposite and leads to color

augmentation (the anti-screening effect), i.e. color charge of the gluons produced in the quantum fluctuations enhances the quark's own color. As the gluon contribution prevails, a decrease of the strong coupling constant, $\alpha_s = g^2/(4\pi)$, with increasing momentum transfer (i.e. decreasing distance between quarks) is observed. This phenomenon is called asymptotic freedom and its theoretical description [42, 43] was awarded the Nobel Prize in 2004. The small value of α_s at high energies has important consequences for accurate descriptions of processes with large momentum transfer, like hard parton scatterings. Cross sections for many processes with small coupling constant are precisely calculated [44] using expansions in powers of α_s provided by QCD perturbation theory (pQCD).

Quarks and gluons have never been seen as free particles in laboratory. This observation led to postulate that quarks and gluons must be confined within elementary particles. The confinement of quarks is not yet fully understood within QCD [39]. The lattice calculations indicate that the energy required to separate a pair of quarks increases with distance, at the rate of $\sim 1\ GeV/fm$ [39]. Therefore, separation of a single quark is not possible as at large distances ($>\ 1\ fm$) there is enough energy in the system to produce a new quark and antiquark pair (current masses of light quarks are low, of the order of 10 MeV/c^2). As a result, in high energy collision experiments, like p+p, instead of free quarks being "kicked" out from the nucleons, a large production of $q\bar{q}$ pairs is observed.

After some simple algebra, one can see that the QCD Lagrangian exhibits global chiral (flavor) symmetry in the limit when the mass term in Eq. 2.1 is neglected [45]. According to lattice QCD calculations [39], the QCD ground state (vacuum) is not "empty" but it is filled up with a condensate of $q\bar{q}$ pairs which does not preserve the chiral symmetry. The phenomenon when the symmetry of the Lagrangian is not preserved at the level of the ground state is called *spontaneous symmetry breaking*. In the sector of the three lightest quarks (i.e. *up*, *down* and *strange*), the octet of massless particles, Goldston bosons [46], which are required by the chiral symmetry breaking in QCD, is represented by the pseudo-scalar octet composed from pions, kaons and η. It is believed that spontaneous chiral symmetry breaking is the underlying mechanism behind the dynamical generation of hadron masses. It is interesting to note that the Higgs mechanism is believed to give mass to elementary particles including *up* and *down* quarks which are more than a hundred times lighter than the proton. Therefore, the large fraction of the proton mass is a dynamic mass which could originate from interactions of its constituents with the QCD vacuum containing the quark condensate.

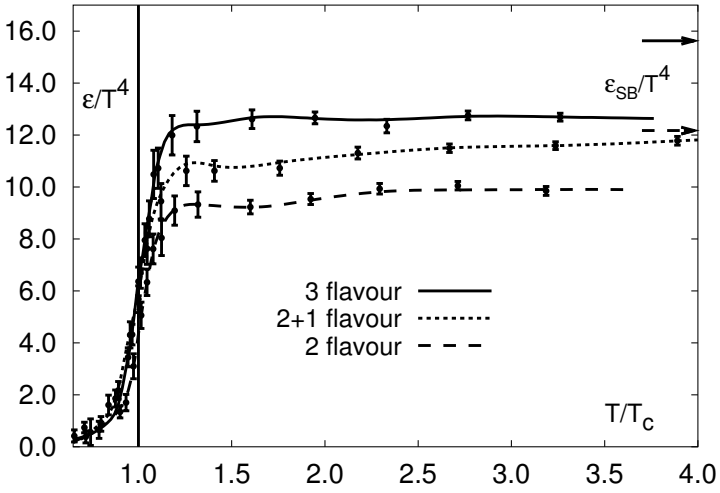

Figure 2.1: *The scaled energy density, ϵ/T^4, as a function of temperature scaled by the critical temperature T_c, calculated with lattice QCD for 2 (dashed line) and 3 (solid line) flavors of light quarks and for two light and one heavier quark flavors (dotted line). ϵ_{SB}/T^4 represents the energy density for an ideal gas of non-interacting and massless quarks and gluons [39, 40].*

2.3 Quark-Gluon Plasma

Interesting quantitative predictions for a thermalized system of quarks and gluons, relevant to relativistic heavy-ion collisions, were obtained using lattice QCD calculations. Results [39, 40] presented in Fig. 2.1, show that the energy density, ϵ, of the system at zero net-baryon number, abruptly increases with increasing temperature, T. This change indicates that a phase transition takes place in the system. The hadronic matter, composed of $q\bar{q}$ and qqq bound states, changes to a phase in which quarks do not reside in bound states but rather constitute a "quark soup" at temperatures larger than a critical temperature of $T_c \approx 170\ MeV$ [39, 40], or $\approx 10^{12}\ K$ (It has be noted that very recent calculations [41] imply that the phase transition may take place at higher $T_c \approx 192\ MeV$). The new phase at high temperature, composed of deconfined quarks and gluons, is called the Quark-Gluon Plasma [47], in analogy to plasmas of electrically ionized gases (originally QGP was called the "quark soup" [48, 49]). The transition to QGP takes place at the critical energy density of $\epsilon_c \approx 1\ GeV/fm^3$ which is about six times larger than the typical energy density of normal, cold nuclear matter. An important property of the QGP state is the screening effect which weakens the attractive interaction of q and $\bar{q}$ pairs.

The impact of the deconfinement of quarks and gluons in a QGP on the energy density can be studied within a simple model assuming that the QGP

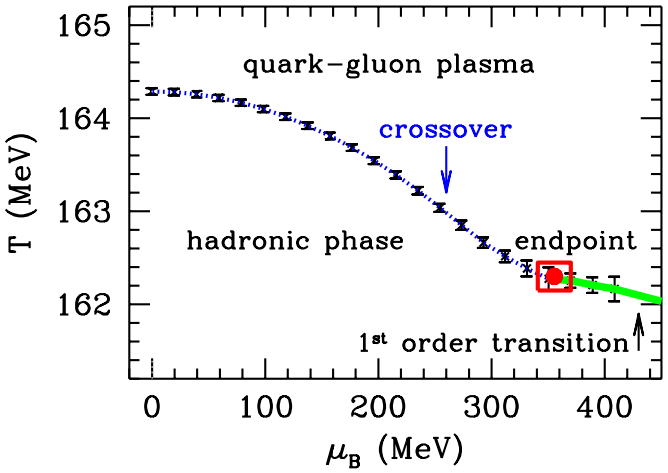

Figure 2.2: *The QCD phase diagram [50] showing different phases as a function of temperature, T, and baryochemical potential, μ_B. See text for details.*

consists of an ideal gas of non-interacting (and massless) quarks and gluons. In such a system, according to the Stefan-Boltzmann law, bosonic and fermionic degrees of freedom contribute $\frac{\pi^2}{30}T^4$ and $\frac{7}{8}\frac{\pi^2}{30}T^4$, respectively, to the total energy density [101]. Therefore, the energy density of a system composed from gluons, quarks and antiquarks of 2 (3) flavors equals $37\frac{\pi^2}{30}T^4$ ($47.5\frac{\pi^2}{30}T^4$). These energy densities are shown by arrows in Fig. 2.1. In the case of a hadronic phase, dominated by pions, a much smaller energy density of $3\frac{\pi^2}{30}T^4$ is expected. One can see that lattice calculations at large T are close to Stefan-Boltzmann limit, thus, for the two decades before the RHIC era, the common belief was that the new state of matter created in the relativistic heavy-ion collisions would be composed from weakly interacting quarks, antiquarks and gluons.

The QCD vacuum structure might be considerably modified in the QGP environment. It is expected that the formation of a QGP is accompanied by the restoration of chiral symmetry in the dense medium. Lattice QCD results [39] show that the quark condensate, $< \psi\bar{\psi} >$, tends to zero with increasing temperature, indicating that at large T the empty, chirally symmetric vacuum is a preferred ground state of QCD.

The lattice results, presented in Fig. 2.1, are relevant to the relativistic heavy-ion experiments at RHIC where (at mid-rapidity) the net-baryon density or the baryochemical potential, μ_B, approaches zero. It is interesting to note that the lattice results at $\mu_B = 0$ are also important for the universe evolution models which assume that the whole universe was in the QGP state shortly (about 10 μs) after the Big Bang.

A QCD phase diagram, based on a recent calculation [50], is presented in Fig. 2.2 where hadronic and QGP phases are shown as a function of temperature,

T, and baryochemical potential, μ_B. It should be noted that at $\mu_B > 0$ lattice calculations are less certain and a complete QCD phase diagram (in the plane $T - \mu_B$) for the real case with two light *up* and *down* quarks and a heavier *strange* quark has not yet been resolved. According to a model of QCD [50], a first order phase transition between hadronic matter and QGP is expected at large baryochemical potential, $\mu_B > 350\ MeV$, while at lower μ_B a continuous crossover is predicted, see Fig. 2.2. The end point of the first order transition line is called the Tricritical Point. A smooth crossover transition is expected to occur at RHIC energies while the region close to the Tricritical Point might be accessible to the heavy-ion AGS and SPS experiments.

At extremely large values of $\mu_B > 1\ GeV$ and low T a new phase of partonic matter was predicted. It is expected that attractive quark-quark interactions could lead to the formation of colored diquark pairs, in analogy to Cooper electron pairs, which give rise to color superconductivity [51]. It is predicted that the superconductive phase should change to a QGP at temperatures higher than $\approx 50\ MeV$ because the thermal motion of quarks and gluons should melt the diquark condensate. Although the color superconductive phase is not reachable in relativistic heavy-ion collisions it could be searched for in cosmological object cores of extreme energy densities [52].

2.4 Experimental Signatures of Quark-Gluon Plasma

Different ideas were proposed to identify signals of the QGP (signatures) in nuclear collisions. Particularly interesting signatures relevant to the AGS, SPS and RHIC experiments are briefly summarized in this Section.

Strangeness Enhancement. If a QGP is produced in nuclear collisions it will rapidly cool down and eventually thousands of new particles, mostly pions, will be produced in the full phase-space, including the mid-rapidity region. The time needed to reach the equilibrium was estimated to be shorter than the expected lifetime of the dense medium produced in the collision [53]. Therefore, there is a good chance that in a thermalized system with an initial composition mostly of deconfined *down* and *up* quarks and gluons, the abundance of *strange* quarks will increase due to gluon splitting. This increased abundance of *strange* quarks should be reflected in an enhanced production of strange hadrons, like K, Λ, Ξ or Ω. However, it should be noted that any final strangeness enhancement in the hadron spectrum represents the abundance at chemical freeze-out, i.e. the point at which inelastic collisions cease, and when the QGP no longer exists.

Direct Photon and Low-Mass Dileptons Production. Dileptons and photons, once produced in the medium, should stay intact since their mean free path is relatively large. These particles are free from the final state strong inter-

actions, hence, their yields depend on the full volume of the system and provide substantial information on the early stage of heavy-ion collisions. In contrast, hadrons are expected to be emitted from the surface and suffer from inelastic interactions in the final state. The "penetrating" signals from thermal photons and dileptons may have a potential to differentiate between the QGP phase and the dense hadron system as an enhanced production of these particles was predicted from the QGP state [54].

The distribution of the invariant mass of dileptons, i.e. $\mu^+\mu^-$ or e^+e^- pairs, combines contributions from different resonances, from the so called "hadronic coctail". The spectrum at low invariant mass ($< 2\ GeV/c^2$) can probe properties of resonances which decay within or close to the dense medium, like the ρ-meson ($\tau_\rho = 1.3\ fm/c$). The dense partonic system is expected to have a significant impact on particle properties, e.g. it was predicted that the chiral symmetry restoration could shift meson masses or change their decay widths [55]. At higher invariant masses ($> 2\ GeV/c^2$), the spectrum is dominated by the annihilation of thermal and primary quark and antiquark pairs.

Suppression of Quarkonia Production. The quarkonium states, composed from heavy quarks, $c\bar{c}$ or $b\bar{b}$, are rarely produced by primary parton interactions in the initial phase of the collision. It was predicted that the mutual interaction of the heavy quark and antiquark may be weaken in QGP due to the screening effect, leading to "melting" of quarkonium states [56]. As a result, a smaller production of J/ψ particles should be observed in central heavy-ion collisions in comparison to the extrapolation from the data of proton or light ion induced reactions.

Disoriented Chiral Condensate. The formation of a QGP could be accompanied by chiral symmetry restoration. The QGP is a short lived state, it lasts for a few fm/c, or $\approx 10^{-23}\ sec$ [53]. After this time, the system has to evolve back to the hadronic phase with spontaneously broken chiral symmetry. Based on effective models of QCD [57, 58], it was predicted that the system is reaching its ground state through an intermediate state with "chirally disoriented vacuum condensate". If states with disoriented chiral condensates (DCC) were possible then very large event-by-event fluctuations in the ratio of the number of neutral pions to the number of charged pions were expected to occur.

Signatures of Particle Production at Very Low-p_T. Several new phenomena in particle production at very low-p_T were anticipated as a consequence of the QGP formation. It was predicted that in nucleus-nucleus collisions, an enhanced production of soft particles could signal new long-wavelength phenomena [26, 59, 60]. It was commonly assumed that a QGP produced in a nucleus-nucleus collision can form a non- or weakly-interacting system of quarks and gluons which could significantly expand before hadronization. Due to the large size of the system before it freezes out a relatively large number of low-p_T particles could be produced. Therefore, an observation of an enhanced production of

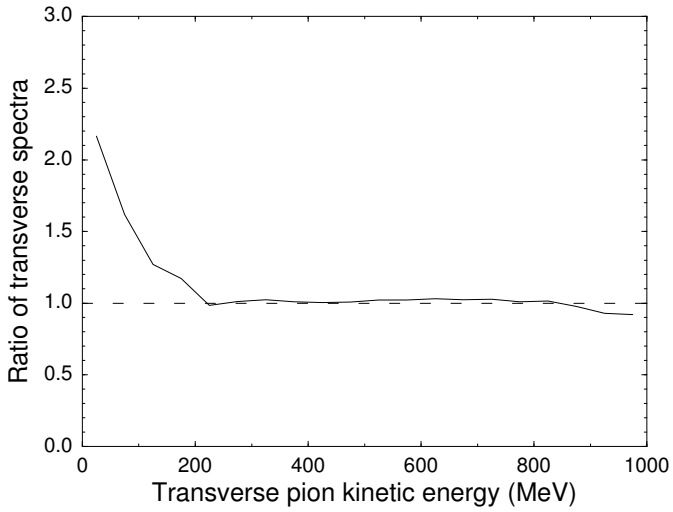

Figure 2.3: *The ratio of the pion spectrum predicted by the DCC model [59] to the Bose-Einstein equilibrium spectrum. The Bose-Einstein formula was fitted to the pion spectrum within the energy interval 0.2 - 1 GeV and extrapolated to low-p_T.*

pions at very low-p_T has a potential to signal new physics at large scales.

Enhanced production of low-p_T ($p_T < 0.2\ GeV/c$) pions was also considered as a signature of DCC in nucleus-nucleus collisions. The yield of pions at very low-p_T, predicted by a model [59] incorporating DCC, is significantly larger than the yield extrapolated from intermediate p_T using the Bose-Einstein equilibrium spectrum, see Fig 2.3.

Interesting studies were performed using a recent optical model to evaluate the geometry of the pionic source [60]. The transverse momentum dependence of experimentally measured HBT radii in relativistic gold ion collisions at an energy of $\sqrt{s_{NN}} = 200\ GeV$ is rather well reproduced in this model. The model, asserting that the chiral symmetry is restored in the pionic source, also predicts a strong modification of the pion spectrum at very low-p_T, within the momentum range from 30 to 60 MeV/c. Therefore, it is interesting to see experimentally whether particle yields at very low p_T exhibit this same structure as predicted by the optical model with restored chiral symmetry.

The soft part of identified particle p_T spectra ($p_T < 2\ GeV/c$) reflects the overall system dynamics from the very beginning of the heavy-ion collision to the final, free-streaming state when hadrons stop interacting at kinetic freeze-out. If the thermal equilibrium is reached in the system one could expect that the collective transverse expansion (transverse flow) should also build up. It is expected that the transverse flow velocity, u_T, and the inverse slope parameter

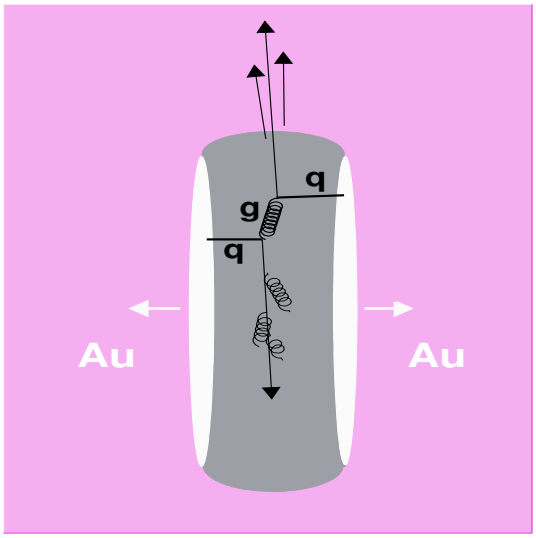

Figure 2.4: *A schematic view of a hard quark-quark scattering. One of two away-side jets is quenched due to induced gluon radiation in dense medium produced in relativistic heavy-ion collisions.*

of the transverse mass[1] ($m_{_T}$) spectra, T_{eff}, are related by the formula [61–63]:

$$T_{eff} \approx T_{fo} + \frac{1}{2} m_h < u_{_T}^2 > \ , \tag{2.4}$$

where T_{fo} is the temperature of the system at kinetic freeze-out. Therefore, in a system with a collective transverse expansion, an increase of the inverse slope parameter, with particle mass should be observed. Such a behavior is seen at SPS [62, 64] as well as at RHIC energies where the effect appears to be stronger [65–67]. The flattening of the spectra, i.e. increasing of the slope parameter, is well reproduced by hydrodynamical models [68–70] incorporating transverse flow. Also other mechanisms were proposed to explain this effect like initial state parton interactions [71, 72] or final state hadron reinteractions [73]. If the flattening of hadron spectra is a transverse flow effect, this may suggest that the evolution of the system occurs in the thermal equilibrium. Such an evolution is a basic assumption of both hydrodynamical/thermal models and lattice QCD calculations. According to these models, the yield of particles at very low momenta is most sensitive to the collective transverse expansion of the system.

Suppression of Particle Production at High-$p_{_T}$. The single particle spectra at high transverse momentum can provide important information on properties of the medium produced in nuclear collisions. The small fraction ($< 1\%$) of particles produced at large transverse momenta ($> 2\ GeV/c$) originates from short-range hard partonic scatterings which occur early in nuclear collisions, see Fig. 2.4. These partons propagate through the dense medium created in nuclear collisions before they fragment into jets of particles with a leading high-$p_{_T}$ hadron

[1] $m_{_T} = \sqrt{p_{_T}^2/c^2 + m_h^2}$, where m_h is particle mass

measured in the detector. It was predicted [74] that interactions of hard-scattered partons with a hot and dense medium formed later in the collision can lead to a strong suppression of high-p_T particle yields in nuclear collisions when compared to the yields in p+p collisions scaled by the number of binary nucleon-nucleon interactions. Observation of a strong high-p_T suppression, called also "jet quenching", could be a direct signature that in nuclear collisions a new state of matter, e.g. a QGP, is formed with partonic energy losses much larger than those from cold hadronic matter.

2.5 Color Glass Condensate

The idea of the Color Glass Condensate [75] is closely related to the initial conditions in the relativistic heavy-ion collisions. It is expected that parton densities at small x in the nuclei prior to collisions increase with the increasing energy. Here, x is the Bjorken scaling variable describing (in the infinite momentum frame) the fraction of the nucleon momentum carried by a parton. It is a well known effect that, at the highest energy of $e + p$ collisions at HERA, the density of gluons, $G(x, Q^2)$, significantly increases at low x and large momentum transfer, Q^2 [76, 77]. This increase can be caused by the gluon radiation from high-x, fast partons. It is expected that this increase will eventually be slowed down (or saturated) due to the fusion of the low-x gluons at high density [78]. A crude estimate for the onset of saturation can be obtained by assuming that in a hadron the fusion process limits the rise of the gluon density at momenta lower than a given saturation momentum, Q_s^2. As the saturation scale, Q_s^2, increases with decreasing x, one may expect that at sufficiently small values of x the perturbative limit is reached, i.e. $Q_s^2 >> \Lambda_{QCD}^2$. In this limit, the momentum dependence of the gluon fusion cross-section takes the form [79]:

$$\sigma \approx \frac{\alpha_s(Q^2)}{Q^2} \tag{2.5}$$

while the number of gluons per unit transverse area is given by:

$$n \approx \frac{xG(x, Q^2)}{\pi R^2} , \tag{2.6}$$

where R is the hadron radius. For the onset of saturation one could expect that $n\sigma \approx 1$, or equivalently

$$Q_s^2 \approx \alpha_s(Q_s^2)\frac{xG(x, Q_s^2)}{\pi R^2} . \tag{2.7}$$

In the relativistic heavy-ion collisions the gluon density per unit transverse area increases due to coherent contributions from different nucleons in a nucleus. As

a result, the saturation momentum scale, Q_s^2, increases by a factor of $A^{1/3}$, where A is the number of nucleons in the nucleus, while the number of low-x gluons decreases.

The initial wavefunctions of the relativistic heavy nuclei could be described within the saturation region using the Color Glass Condensate formalism [75]. In this approach the nuclei prior the collision are viewed as systems of frozen partons and dynamical fields. The frozen partons are fast moving, relativistically contracted color sources (e.g. large-x quarks), while dynamical classical fields, A_μ represent highly populated low-x gluons. The dynamical fields are determined by solving the Yang-Mills equations with the source given by the frozen charges. The concept of the Color Glass Condensate is important because it is proposed from first principles of QCD as a universal approach to describe the properties of energetic particles and, consequently, can influence the properties of a system composed from strongly interacting particles formed in the relativistic heavy-ion collisions. "Glass" in the name refers to silica which is disordered and acts like a solid (frozen) material on short time scales but like a liquid on long time scales.

Chapter 3

Heavy-Ion Collisions Before the RHIC Era

In the search for a new state of matter, existing accelerators at Brookhaven National Laboratory and CERN were at first adopted to provide relativistic heavy-ion collisions. In the Alternating Gradient Synchrotron at BNL heavy-ions (e.g. gold ions) were for the first time accelerated to the relativistic energy of 11.7 $A\ GeV$. The high energy beams were collided with fixed, stationary nuclear targets, providing a rather modest center-of-mass energy (per nucleon) of $\sqrt{s_{_{NN}}} \approx\ 5\ GeV$. The energy in the center-of-mass frame is available for particle production, thus, it is a relevant scale for probing the properties of the dense medium created in the relativistic nuclear collisions. The collision energy was significantly increased at the Super Proton Synchrotron at CERN. Lead ions at the highest energy of 158 $A\ GeV$ were provided to the fixed target SPS experiments. The corresponding center-of-mass energy of $\sqrt{s_{_{NN}}} =\ 17.3\ GeV$ was reached. It has to be noted that the search for the QGP in these fixed target experiments was performed in a baryon-rich environment. A significant baryon stopping is observed in heavy-ion collisions at the AGS [80, 81] and SPS [82–84] energies. Particularly interesting experimental results obtained in the AGS and SPS experiments, related to QGP signatures, include [85]: the enhancement of strange particle production [84, 86], the suppression of the quarkonium J/ψ production [87] and the enhanced production of photons [88] and dileptons [89, 90]. Short descriptions and explanations of these phenomena are presented in this Chapter.

- The data obtained in experiments at the AGS and SPS clearly show the enhancement of strange particle production [84, 86], expected as a positive signature of a QGP. For example, results from the NA57 experiment show that the yields of strange baryons, Λ, Ξ and Ω per participating (wounded) nucleon in Pb+Pb collisions at $\sqrt{s_{_{NN}}} =\ 17.3\ GeV$ are larger than corresponding yields in p+Be and p+Pb reactions. Interestingly, the measured

particle ratios are quite consistent with thermal model predictions with a single temperature and baryochemical potential supporting the idea that thermal equilibrium is reached in the relativistic heavy-ion collisions [91]. This is particularly remarkable for the production rates of rare baryons and antibaryons containing multiple *strange* quarks.

The energy evolution of the strangeness production with the energy of colliding nuclei was analyzed in the NA49 experiment [92]. A non-monotonic behavior of the K^+/π^+ ratio, a horn like structure, was observed in central Pb+Pb collisions with maximum at an energy around 30 $A\ GeV$. This abrupt behavior was related to the onset of quark and gluon deconfinement when a large number of degrees of freedom is released [93]. Other explanations based on string or thermal models were not successful [94, 95].

- Direct photon production in central Pb+Pb collisions at $\sqrt{s_{_{NN}}} = 17.3\ GeV$ was measured by WA98 experiment [88]. The invariant yield of direct photons show a 10-20% excess at $p_{_T} > 1.5\ GeV/c$ with respect to the photon production in proton induced reactions scaled by the number of binary nucleon-nucleon interactions of the Pb+Pb collisions. However, the absolute yields suffer from large systematic uncertainties. Nevertheless, these measurements provide a valuable constraint on the initial temperature of the system.

- In the distribution of the invariant mass of e^+e^- pairs in central Pb+Au collisions at $\sqrt{s_{_{NN}}} = 17.3\ GeV$ obtained by the CERES experiment [89], a strong enhancement was observed in the mass region from 0.2 GeV/c^2 to 0.6 GeV/c^2 with respect to the yield calculated from known hadronic sources. An interesting explanation of this enhancement was proposed in a model where $\pi^{\pm}$ annihilation and in-medium modification of ρ-meson induced by chiral symmetry restoration were included.

- One of the most appealing signatures of QGP in heavy-ion collisions comes from measurements of the J/ψ quarkonium state. The hadronic production of J/ψ is observed as the high mass resonance in the dilepton mass distribution. The J/ψ resonance is easily seen over the Drell-Yan continuum and has a maximum at 3.1 GeV. The ratio of J/ψ to Drell-Yan cross sections in Pb+Pb collisions at $\sqrt{s_{_{NN}}} = 17.3\ GeV$ measured as a function of the collision transverse energy [87], $E_{_T}$, shows substantial suppression for $E_{_T} > 30\ GeV$ in comparison to the extrapolations from models invoking the absorption of charmonium states in a dense hadronic system with $\sigma_{abs} = 6.4 \pm 0.8\ mb$. The model gives a reasonable prediction for the ratio at lower $E_{_T}$. These results were predicted as a consequence of QGP formation long before the experimental data were available.

The results presented in this Chapter are examples of effects which were expected as positive experimental signatures of the presence of a QGP in relativistic heavy-ion collisions [1, 85]. Due to the "multitude" of these positive signatures, some physicists were in favor of a "common assessment" [96] stating that in the early stage of the collision the large deposit of energy turns the nuclear matter into a state of quarks and gluons in a deconfined phase (QGP) already at CERN SPS. However, it should be stressed that each result mentioned above is not unambiguous evidence that a new state of matter has been produced as interpretation without the assumption that the QGP exists is possible [97, 98].

It became obvious that the search for effects indicating that a QGP was produced in relativistic heavy-ion collisions should continue at higher energies, i.e. for partonic systems of larger energy density and temperature. In particular, the limited range of the center-of-mass energy at the SPS is related to rather modest reach in transverse momenta of produced particles. Therefore, at the SPS, the study of particle production at high p_T can only be performed within a few GeV/c range. The range of high-p_T ($p_T \geq 5\ GeV/c$) in nuclear collisions has been fully accessed at RHIC leading to new, remarkable discoveries which will be presented later in this paper.

Chapter 4

Relativistic Heavy Ion Collider

A real break-through in field of heavy-ion collisions came, again, from BNL when RHIC become operational in the year 2000. In this accelerator, two beams of gold ions are boosted to an energy of 100 $A\ GeV$ each, providing the Au+Au collisions at $\sqrt{s_{NN}} = 200\ GeV$. At such high energies the colliding nuclei are significantly longitudinally contracted. At the full RHIC energy the Lorentz factor, γ, in the center-of-mass system amounts to about 100, thus, at this energy the longitudinal size of the gold nucleus, $2R/\gamma \approx 0.15\ fm$, is smaller than a hadron. At such small scales, it seems more natural to view the two colliding nuclei as sheets composed of partonic matter (e.g. the Color Glass Condensate), instead as bundles of individual nucleons. After the collision, the nuclei leave behind a region filled with quarks and gluons. While this region expands, the dense partonic system is approaching thermal equilibrium by mutual interactions. It is commonly expected that, at very high energies, the baryon number density or baryochemical potential in the system will be close to zero, as the majority of valence quarks during the collision should preserve their original direction of motion, carrying away the initial excess of baryon number.

4.1 The Accelerator

The RHIC accelerator is the first purpose-built relativistic heavy-ion collider [99]. It consists of two intersecting rings of 3834 m in circumference, see Fig. 4.1. Two ion beams, guided by 1740 superconducting, helium-cooled magnets, are brought into collision at the four experimental locations. The acceleration process at the RHIC complex starts at the Tandem Van de Graaff facility which can deliver more than 40 types of ions ranging from hydrogen to uranium. The Tandem feeds pre-accelerated particles in the booster synchrotron which are then injected into the AGS accelerator. Gold ions in the AGS are boosted from an injection energy of 1 $A\ GeV$ to a fully relativistic energy of 9.8 $A\ GeV$ before they are transferred into the RHIC rings for final acceleration. The highest energy of each

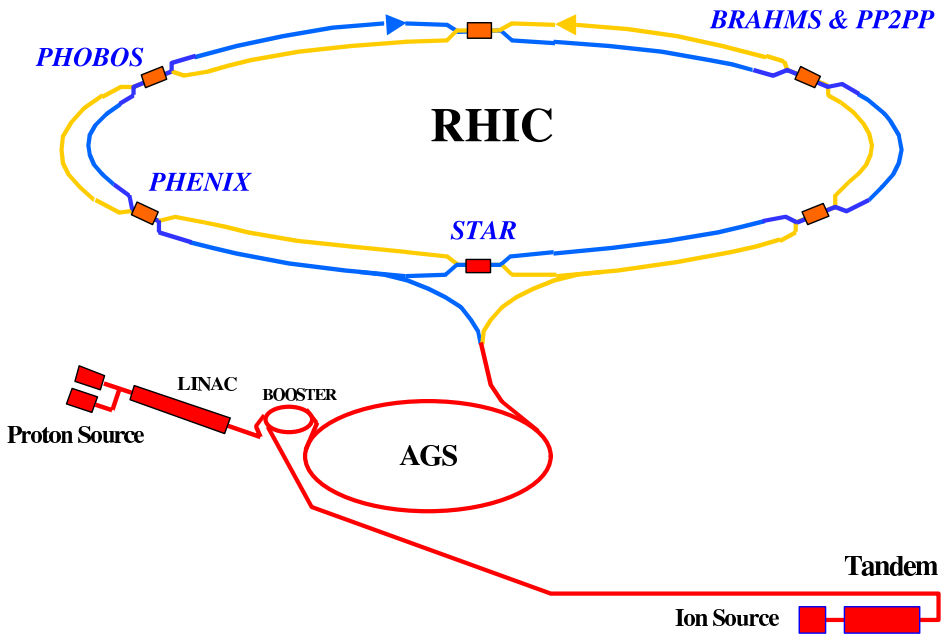

Figure 4.1: *A schematic view of the RHIC complex.*

gold ion beam achieved at RHIC is 100 $A\,GeV$. Protons, delivered by the LINAC facility, can be accelerated in RHIC to an energy of up to 250 GeV.

Nominally, one beam of gold ions consists of 60 bunches and each bunch has of the order of 10^9 ions. A luminosity of the order of 10^{26}-10^{27} $cm^{-2}s^{-1}$ was attained for Au+Au collisions at $\sqrt{s_{NN}} = 200\ GeV$, which corresponds to a collision rate of tens of kHz.

4.2 The Heavy-Ion Experiments at RHIC

There were four detectors built at different beam intersection regions (IR) at RHIC: PHOBOS [3], BRAHMS [4], PHENIX [5] and STAR [6]. The location of each detector is depicted in Fig. 4.1. Each experiment has unique features which allow for a complete and complementary study of the properties of nuclear collisions. Concise reviews of the main physical results obtained by all four RHIC experiments were presented in "White Papers" published in one volume of Nuclear Physics A [2, 100–102].

PHENIX. PHENIX is the largest detector at RHIC utilizing different experimental techniques to measure many aspects of nuclear collisions including direct photons, dileptons or quarkonium states. One of the main components of the PHENIX detector is the central magnetic spectrometer. The two arm spectrom-

eter measures charged particles in the pseudorapidity[1] range $|\eta| < 0.35$ and each arm covers a range of 90^o in azimuth. Trajectory curvatures in the magnetic field are used to determine particle charge and momentum. Identification of charged hadrons, like charged pions, kaons, protons, antiprotons, deuterons, is provided by time of flight counters (TOF) within the $p_{_T}$ range from 0.25 GeV/c up to a few GeV/c.

STAR. The second largest detector built at RHIC is the STAR detector. The detector has excellent tracking capabilities provided by the large acceptance Time Projection Chamber (TPC) placed inside a solenoidal magnetic field. The TPC extends over a large cylindrical volume of length $\pm 2.1\ m$ along the beam axis and has a radius of $0.5 - 2\ m$. The tracking capabilities over the full azimuthal angle coverage and a rather large pseudorapidity range, $|\eta| < 1$, is the unique property of the STAR detector. Particle momentum and charge are obtained from the curvature of particle trajectories in the magnetic field. The TPC detector also provides identification of charged particles, like pions, kaons, protons, antiprotons or electrons, at intermediate transverse momenta. The identification capability of TPC is extended to higher transverse momenta, up to a few GeV/c, by the Time of Flight Counters. In the range of $2.5 < p_T < 10\ GeV/c$ particles can be identified in the TPC detector exploiting the relativistic rise of the ionization energy loss.

The measurements at mid-rapidity are extended to $|\eta| > 1$ by a pair of forward time projection chambers (FTPC), located along the beam pipe at both sides of the nominal interaction point, and an end-cap electromagnetic calorimeter. Measurements in the forward direction are important for both the RHIC heavy-ion and spin programs.

BRAHMS. The BRAHMS detector was design to measure only a small number of particles produced within a specific range of angles in each RHIC collision. The momentum, energy and other characteristics of the particles are measured very precisely. The main components of the BRAHMS detector are the two magnetic spectrometers that can rotate in the horizontal plane around the nominal interaction point. Therefore, the detector covers a wide rapidity range from -0.1 to 4 for pions and from -0.1 to 3.2 for protons. The tracking system in both the mid-rapidity range and the forward spectrometers is based on signals from both a TPC and drift chambers. Particle identification is provided by TOF and Čerenkov detectors. The measurement of identified particle spectra at large rapidity range is the unique capability of the BRAHMS detector.

[1]The pseudorapidity is defined as $-ln(tan(\theta/2))$ where θ is the polar angle of a particle relative to the beam axis.

Chapter 5

The PHOBOS Experiment at RHIC

5.1 The Detector

The PHOBOS experiment was design to measure global characteristics of nucleus-nucleus collisions by detecting charged particles within almost the full solid angle as well as identified charged particles produced in a small fraction of phase space, near mid-rapidity. Particularly, the detector was optimized to measure identified particles at very low and intermediate momenta. The measurement at very low-$p_{_T}$, as low as 30, 90 and 140 MeV/c for charged pions, kaons and for protons and antiprotons, respectively, is the unique property of the PHOBOS experiment at RHIC.

The PHOBOS detector layout, illustrated in Fig. 5.1 and Fig. 5.2, was described in the "Proposal to Study Very Low $p_{_T}$ Phenomena at RHIC" [103–105] and was approved by the RHIC Program Advisory Committee in 1994. The main components of the detector are the multiplicity array and the two-arm magnetic spectrometer.

The multiplicity array consists of an octagonal barrel of silicon strip detectors surrounding the interaction region. This barrel is augmented by six rings of silicon pad detectors located symmetrically on both sides of the nominal interaction point along the beam pipe[1] and the inner layers of the Vertex Detector. The multiplicity array is a detector which covers a solid angle of almost 4π and thus a wide range of pseudorapidity ($|\eta| < 5.4$). The segmentation of silicon detectors,

[1]The nominal interaction point defines the origin of the coordinate system used in the PHOBOS experiment (and hereafter). The Z-axis of PHOBOS coordinate system is parallel to the beam pipe and oriented clockwise in Fig. 4.1 or toward the left side in Fig. 5.1. The Y-axis is top vertical while the X-axis completes the right handed coordinate system, i.e. it is located in horizontal plane, perpendicular to the accelerator beam pipe and pointing outside from the center of the RHIC accelerator ring.

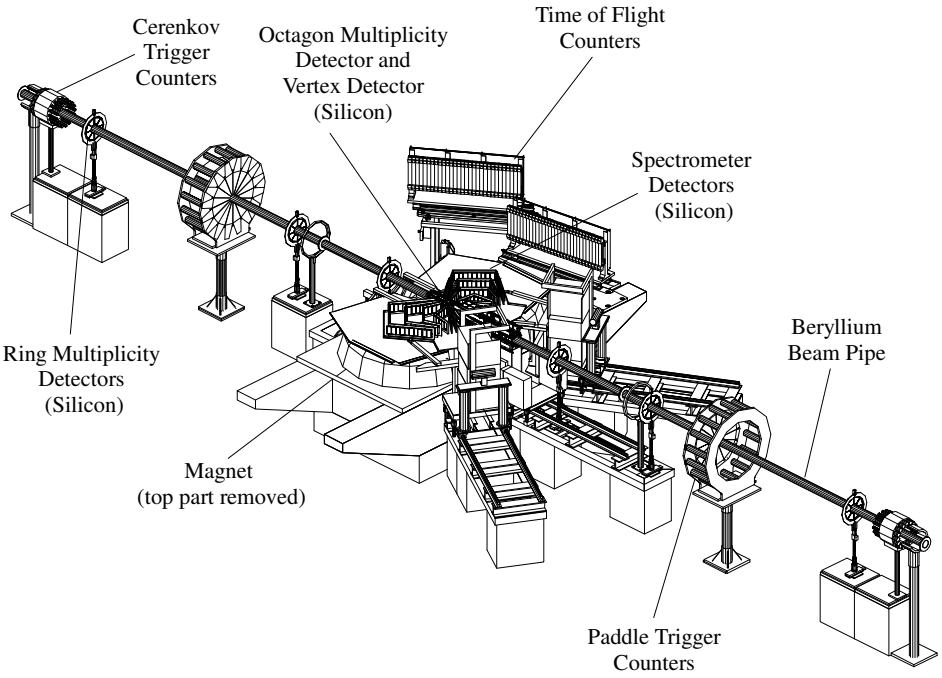

Figure 5.1: *A schematic view of the PHOBOS detector layout in year 2001 during the second physics run when gold ions were for the first time collided at the full RHIC energy of* $\sqrt{s_{_{NN}}} = 200\ GeV$.

described in detail in Ref. [3], allows one to measure charged particles in fine pseudorapidity intervals of $\Delta\eta \approx 0.1$. The segmentation in the azimuthal angle, ϕ, is about 0.2/0.1 radians for the Octagon/Ring array. The Vertex Detector is composed from two pairs of silicon layers located at the top and the bottom of the multiplicity octagon detector. The detector covers a pseudorapidity range of $|\eta| < 0.92$ and 25% of the azimuthal angle. The Vertex Detector is used for precise determination of the interaction point as well as charged particle multiplicity measurements.

A small fraction of charged particles (about 1%) is measured by means of the Spectrometer which is placed in a 2 T magnetic field. The Spectrometer and magnet were design to assure good capability to measure charged pions, kaons, protons and antiprotons at very low and intermediate transverse momenta and charged hadrons at higher $p_{_T}$. It consists of two arms which are located horizontally on either side of the beam pipe covering a pseudorapidity range from about 0 to 2 and azimuthal angle range of 12^o. Each arm consists of 16 layers of silicon detectors. There are 274 silicon sensors, each approximately 300 μm thick, in both arms. The location of all silicon sensors in the Spectrometer was determined by a combination of optical surveys and a final alignment procedure using reconstructed particle tracks. This procedure allowed for an accuracy of

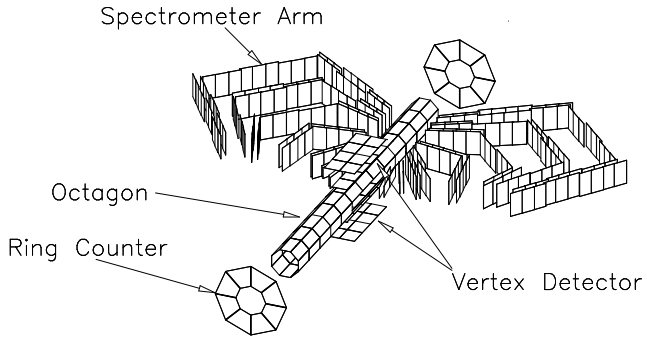

Figure 5.2: *The geometrical layout of active (i.e. sensitive to traversing particles) elements of the multiplicity array. Only one of three pairs of Ring Multiplicity Detectors, the closest to the interaction point, is shown. All silicon wafers of both spectrometer arms are illustrated.*

100 μm to be attained. Silicon sensors in the Spectrometer have a fine pixelization in 5 different types [3]. Six inner planes, those closest to the beam pipe, are in an approximately magnetic field free region, as illustrated in Fig. 5.3. The π-shaped layers are located in a non-uniform magnetic field, oriented vertically in the Spectrometer area, with maximum of 2.2 T. The bottom part of the PHOBOS dipole magnet is shown in Fig. 5.1.

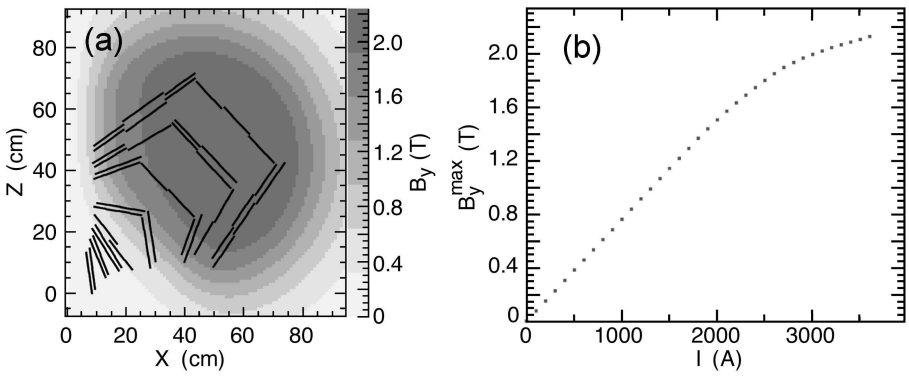

Figure 5.3: *The map of the vertical component of the PHOBOS magnetic field, B_y, in the horizontal plane (y=0) with an outline of the silicon detectors in one Spectrometer arm (a). The panel (b) shows the maximum B_y as a function of the excitation current.*

The silicon sensor design and read-out system of the PHOBOS detector are presented in detail in [3]. The electronics are capable of measuring ionization energy losses of charged particles over a large dynamic range. Therefore, it is possible to measure energy losses of both minimum and highly ionizing particles. The large dynamic range, the weak magnetic field in proximity of the interaction

region and the small amount of dead material allow for reconstruction of low-momentum particles in the first silicon layers of the Spectrometer. To minimize backgrounds from secondary interactions, the PHOBOS experimental area was equipped with a 1 mm-thin, 3 inches in diameter and 12 m-long beryllium beam pipe.

5.2 Details of Experimental Data Samples

The PHOBOS experiment was taking data for six years, from 2000 to 2005. The first two runs (Run-01 and Run-02, see Table 5.1) were mainly devoted to Au+Au collisions. The full RHIC energy of $\sqrt{s_{_{NN}}} = 200\ GeV$ was obtained gradually with two intermediate energies of 56 and 130 GeV. Run-03 was mainly devoted to d+Au collisions at $\sqrt{s_{_{NN}}} = 200\ GeV$ which serve, together with p+p interactions, as a reference sample for Au+Au collisions at the same energy. The performance of the RHIC accelerator significantly increased over time. The integrated luminosity at the PHOBOS intersection for Au+Au collisions at full energy was estimated to be about 35 μb^{-1} in 2002 while two years later the corresponding luminosity increased to 600 μb^{-1}. The large data samples collected in 2004 and 2005 allow for a detailed study of nuclear collisions on system size and energy. A summary of the experimental data collected by PHOBOS is presented in Table 5.1.

Table 5.1: *Summary of data collected by the PHOBOS experiment. The number of events represent the total number of events stored on tapes.*

Year	Run Name	Ions	$\sqrt{s_{_{NN}}}\ [GeV]$	Number of Events [M]
2000	Engineering Run	Au+Au	56	1.8
	Run-01	Au+Au	130	4.3
2002	Run-02	Au+Au	200	34
		Au+Au	19.6	0.76
		p+p	200	23
2003	Run-03	d+Au	200	146
		p+p	200	50
2004	Run-04	Au+Au	200	215
		Au+Au	62.4	22
		p+p	200	28
2005	Run-05	Cu+Cu	200	400
		Cu+Cu	62.4	110
		Cu+Cu	22.5	20
		p+p	410	110

The analyses presented in this paper are based on the Au+Au data at energy of $\sqrt{s_{_{NN}}} = 62.4\ GeV$ and $\sqrt{s_{_{NN}}} = 200\ GeV$ collected during Run-04 and Run-02, respectively. The sample of d+Au collisions at $\sqrt{s_{_{NN}}} = 200\ GeV$ was also used for comparison with the Au+Au results obtained at the same energy.

5.3 Event Triggering

The event triggering system was significantly enhanced over the six years of data taking by the PHOBOS experiment, i.e. 2000-2005. At the beginning, the primary event trigger was based on Paddle Trigger Counters [3]. The timing information from Paddles was used to make real-time decisions to trigger on inelastic Au+Au interactions. The Paddle Trigger Counters consist of two arrays of 16 plastic scintillator detectors each (see Paddle Trigger Counters in Fig. 5.1) located at $\pm 3.21\ m$ from the nominal interaction point along the beam pipe and covering pseudorapidity range of $3 < |\eta| < 4.5$. Particles produced in collisions close to the nominal interaction point arrive at the two arrays of Paddle Trigger Counters in approximately the same time, measured with a relative resolution of $2\ ns$. Thus, by setting criteria on the measured time difference one can select mostly interactions of colliding ions (beam-beam interactions) and suppress background events, e.g. from interactions of single beam ions with residual gas of the beam pipe vacuum (beam-gas interactions). During off-line analysis additional rejection of beam-gas interactions is obtained using the Zero Degree Calorimeters (ZDC). The ZDC calorimeters (not shown in Fig. 5.1) are located at both sides of the nominal interaction point, at Z = $\pm 18.5\ m$, and at $\theta = 0^o$ relative to the Z-axis, The calorimeters are placed behind the beam deflection RHIC DX-magnets which steer beam ions in the intersection area. Therefore, the ZDCs can only detect the energy of neutrons as charged fragments of colliding ions are deflected in the magnetic field of DX magnets. As a result, the ZDC detectors do not provide a good measure of the collision centrality [108, 109]. Only the timing capabilities of these calorimeters are used in PHOBOS to suppress beam-gas events and to determine the accelerator luminosity at the PHOBOS intersection.

The on-line trigger was significantly improved after two rings of ten Čerenkov Counters (T0 detector), surrounding the beam pipe, were implemented in the PHOBOS detector during d+Au Physical Run in 2003. The coincidence of high resolution timing signals from these two sets of Čerenkov counters (T0) was used, in addition to the Paddle Trigger Counters and ZDC as a primary trigger, to select real collisions. In the Au+Au run in 2004 the T0 Čerenkov Counters covered pseudorapidity range of $4.4 < |\eta| < 4.9$ and were located at $\pm 5.2\ m$ away from the nominal interaction point along the beam pipe. In d+Au collisions, due to asymmetric charged particle pseudorapidity distribution the counter in the positive hemisphere (on the "deuteron side") were located at $2.46\ m$ to increase their

triggering efficiency. Therefore, the pseudrapidity range covered by Čerenkov counters in the d+Au run was $-4.9 < \eta < -4.4$ and $3.6 < \eta < 4.1$. For part of the d+Au data set, a further on-line selection of events was accomplished by using two arrays of horizontally segmented scintillator hodoscopes (SpecTOF detector, not shown in Fig. 5.1). The arrays were positioned behind the Spectrometer to detect signals from particles traversing the Spectrometer. A combination of spatial coincidence from the hodoscopes with the known vertex position was used to trigger on high-p_T particles traversing the Spectrometer.

5.4 Vertex Determination

The determination of the interaction point in the PHOBOS experiment is based on primary particles. As the multiplicity of produced charged particles in d+Au is much smaller than that in central Au+Au collisions, different vertexing algorithms were used in the analysis of Au+Au and d+Au data. In Au+Au collisions, the Vertex Detector provides a good reconstruction of the collision vertex along Z-axis, with a resolution better than 0.2 mm [3, 106]. However, this detector is not capable of attaining a reasonable resolution in the transverse direction as strips of silicon wafers in the Vertex Detector are parallel to X-axis. To improve the reconstruction a method using the first silicon layers of the Spectrometer was developed. Requiring a consistent vertex position obtained from the Spectrometer and Vertex Detectors, in combination with the known position of the beam orbit, a resolution better than 0.3 mm in the vertical direction and better than 0.5 mm in the X direction was achieved. The large number of produced particles in the most central events makes the algorithm 100% efficient with efficiency defined as the probability of finding a valid vertex within 0.5 cm of the true vertex position.

Due to the low particle multiplicity in d+Au collisions the Vertex and Spectrometer Detectors are not sufficient to determine the vertex position for a significant fraction (about 50%) of events. For these events a new, more efficient, vertex algorithm was developed, utilizing the hit positions and energy deposited in the Octagon Detector. Using this algorithm the vertex position along the beam direction can be determined with resolution of 1.4 cm for the peripheral d+Au events and 0.8 cm for the most central collisions. The transverse position of vertex was centered at the known location of the beam orbit.

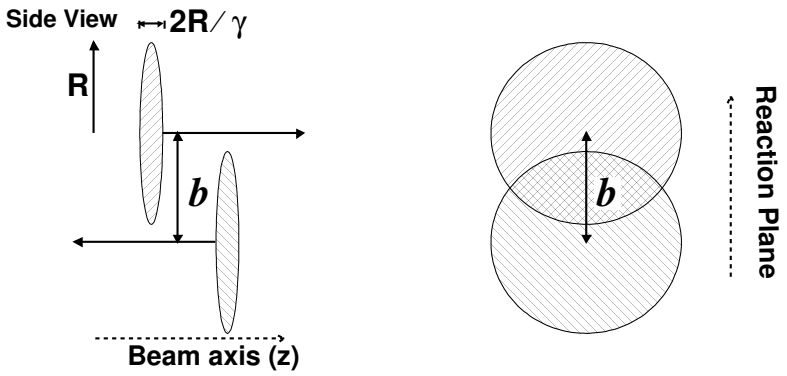

Figure 5.4: *A schematic view of a relativistic ion collision at the impact parameter b in the center-of-mass system. The relativistic contraction in the longitudinal direction by the Lorentz factor γ (left panel: side view) and the almond overlap region of the colliding nuclei (right panel: view along the beam axis) are illustrated. The reaction plane is the plane defined by the beam axis and the impact parameter.*

5.5 Centrality Determination

A schematic view of a relativistic ion collision is illustrated in Fig. 5.4. In the center-of-mass system (the laboratory in the case of the RHIC collider), the two nuclei can be viewed as two thin disks, each one representing a relativistically contracted nucleus. The transverse distance between the centers of colliding ions is called the impact parameter. For a given impact parameter, nucleons located in the overlap region, shown in Fig. 5.4, can participate in inelastic nucleon-nucleon interactions. These nucleons are called participating or wounded nucleons. The number of participating nucleons, N_{part}, as well as the number of binary inelastic nucleon-nucleon interactions, N_{coll}, can be calculated using the Glauber model [107]. The dependence of N_{part} and N_{coll} on the impact parameter, calculated for Au+Au collisions at $\sqrt{s_{NN}} = 200\ GeV$, is shown in Fig. 5.5. One can see that for the most central Au+Au collisions (smallest impact parameters) almost all nucleons are wounded and $N_{coll} \approx 1200$.

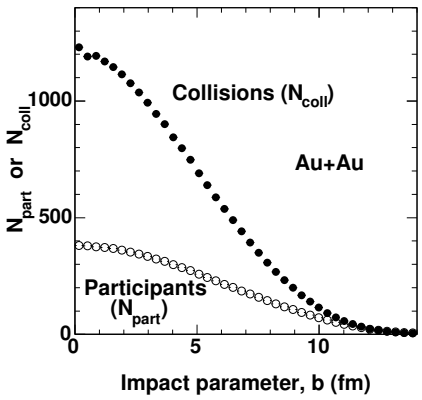

Figure 5.5: *N_{part} and N_{coll} as a function of the impact parameter, calculated for Au+Au collisions at $\sqrt{s_{NN}} =$ 200 GeV using the Glauber model.*

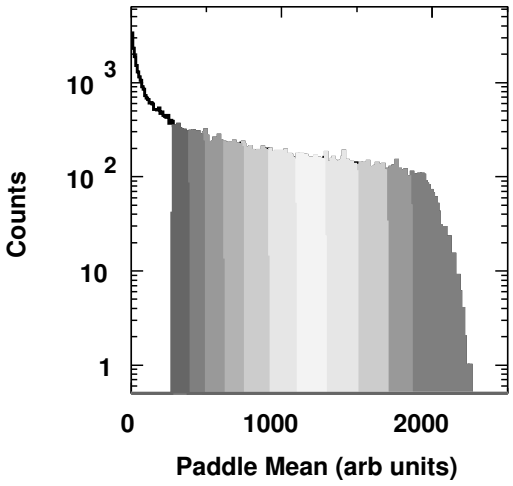

Figure 5.6: *The distribution of the average ionization energy losses in the Paddle Trigger Counters divided into classes of events of different centrality. The histogram was done for Au+Au collisions at* $\sqrt{s_{NN}} = 200\ GeV$.

In the PHOBOS experiment, the large acceptance of the Paddle Trigger Counters, covering the pseudorapidity range of $3 < |\eta| < 4.5$ and 2π in azimuth, were used for the centrality determination in Au+Au collisions [108, 109]. Apart from timing information, ADC signals of the Paddle Trigger Counters (ionization energy losses of charged particles) were also measured. The ADC signal measured in the Paddle Trigger Counters is proportional to the multiplicity of charged particles produced within the Paddle detector acceptance. The multiplicity, in turn, is strongly correlated with the collision geometry. The distribution of the summed ADC signals is "sliced" to separate events into classes of different centralities, as shown in Fig. 5.6. All experiments at RHIC agreed to express the collision centrality as a fraction (in %) of the total cross-section with smaller numbers corresponding to more central data. For example, an interval 0-15% denotes a class of the 15% most central events. To provide the centrality parameters for a class of events the distribution of ADC signals in the Paddle Trigger Counters is modeled using Monte Carlo (MC) simulations based on the HIJING [110] event generator and a full GEANT [111] simulation of the detector response. Both MC simulated and experimentally measured distributions were found to be in a good agreement. Dividing the sample of MC events using the same criteria as for experimental data allows one to associate centrality parameters (N_{part}, b), available from the Glauber model implemented in HIJING, to experimentally selected classes of events. In the HIJING calculations, the default value for the inelastic nucleon-nucleon cross-section of 41/36 mb was used, for Au+Au collisions at 200/62.4 GeV energy. For the data presented here, Au+Au events were divided

Table 5.2: *Details of the centrality classes used in the analysis of Au+Au data at energy of* $\sqrt{s_{NN}} = 62.4\ GeV$ *and* $\sqrt{s_{NN}} = 200\ GeV$*. Calculated values of* $\langle N_{part} \rangle$ *and* $\langle N_{coll} \rangle$ *and systematic uncertainties are presented for six centrality ranges.*

Centrality	$\left\langle N_{part}^{62.4} \right\rangle$	$\langle N_{coll}^{62.4} \rangle$	$\left\langle N_{part}^{200} \right\rangle$	$\langle N_{coll}^{200} \rangle$
45–50%	61 ± 7	76 ± 12	65 ± 4	107 ± 16
35–45%	86 ± 9	120 ± 16	93 ± 5	175 ± 25
25–35%	130 ± 10	215 ± 22	138 ± 6	300 ± 39
15–25%	189 ± 9	370 ± 24	200 ± 8	500 ± 60
6–15%	266 ± 9	590 ± 21	276 ± 9	780 ± 86
0–6%	335 ± 11	820 ± 25	344 ± 11	1050 ± 105

Table 5.3: *Values for* $\langle N_{part} \rangle$ *and* $\langle N_{coll} \rangle$ *and the systematic uncertainties for the four centrality ranges of d+Au collisions at energy of* $\sqrt{s_{NN}} = 200\ GeV$*.*

Centrality	$\langle N_{part} \rangle$	$\langle N_{coll} \rangle$
70–100%	3.3 ± 0.7	2.2 ± 0.6
40–70%	6.7 ± 0.9	5.4 ± 0.8
20–40%	10.9 ± 0.9	9.7 ± 0.8
0–20%	15.5 ± 1.0	14.6 ± 0.9

into six centrality intervals. The values and systematic uncertainties for $\langle N_{part} \rangle$ and $\langle N_{coll} \rangle$ at both 62.4 and 200 GeV are listed in Table 5.2.

The centrality cuts for d+Au analysis were based on the sum of ADC signals (E_{Ring}) from all six Ring Multiplicity Detectors covering a wide pseudorapidity region of $3.0 < |\eta| < 5.4$. For each of the four ranges of E_{Ring}, shown in Table 5.3, $\langle N_{part} \rangle$ and $\langle N_{coll} \rangle$ were obtained from the Glauber model calculation using HIJING [110] and a full detector simulation provided by GEANT [111]. The percentage numbers refer to the fractional cross-section in the unbiased HIJING distribution. The determination of $\langle N_{part} \rangle$ and $\langle N_{coll} \rangle$ takes into account the bias introduced in the centrality by the on-line and off-line event selection in the relatively low-multiplicity d+Au events.

5.6 Multiplicity Measurements

The PHOBOS experiment has a unique capability to measure charged particle multiplicity within almost the full solid angle, covering a pseudorapidity range of $|\eta| < 5.4$ and 2π in azimuth. There are several different methods used to estimate the charged particle density. In the η and ϕ plane, a combination of data from the single-layer Octagon ($|\eta| < 3$) and Ring ($3 < |\eta| < 5.4$) Multiplicity Detectors form an energy deposition map of signals in silicon pads. To measure the charged particle density the data are analyzed using two different techniques. In the "analog" method, the deposited energy in a silicon detector pad, normalized to the average energy of a single particle derived from MC simulations, is used to estimate the number of particles traversing the pad after accounting for the orientation of the Si-wafer relative to the interaction point. The "digital" approach treats each pad as a binary counter and assumes Poisson statistics to estimate the total occupancy in various regions of pseudorapidity. Both methods were found to give consistent results. A typical result on the charged particle density [112] is presented in Fig. 5.7.

At mid-rapidity, the Vertex Detector and the first layers of the Spectrometer are used to count "tracklets". "Tracklets" are two-hit tracks which point back to the event vertex. Therefore, the number of produced particles within the Vertex Detector acceptance should be proportional to the number of "tracklets". A set of "tracklets" for a single event in the Vertex Detector is drawn in Fig. 5.8.

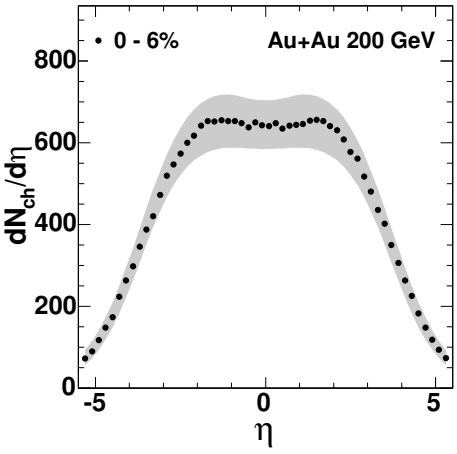

Figure 5.7: *The pseudorapidity density of charged particles produced in the 6% most central Au+Au collisions at an energy of* $\sqrt{s_{NN}} = 200$ *GeV [112]. The grey band shows the systematic uncertainty.*

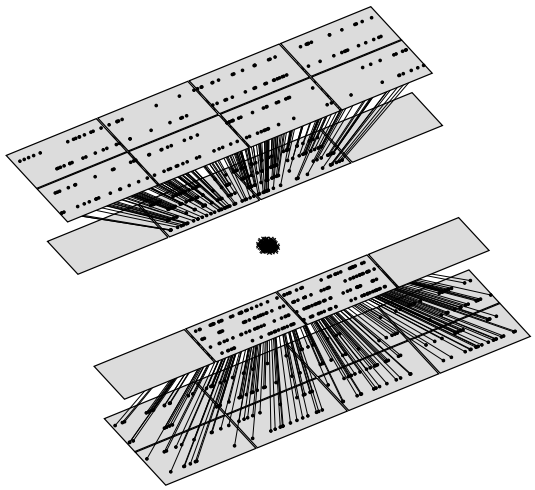

Figure 5.8: *"Tracklets" in the Vertex Detector constructed from hits of a single Au+Au collision. The "tracklet" counting method allows the density of particles produced at mid-rapidity to be calculated.*

5.7 Momentum Measurements

In the PHOBOS detector charged particles can be measured in a wide range of transverse momentum. The fine segmentation of silicon sensors in the Spectrometer [3] allows the particle trajectories in the magnetic field to be determined from the measured hit positions. A schematic view of a particle trajectory in one arm of the Spectrometer is illustrated in Fig. 5.9. The particle charge and momentum are obtained from the curvature of the trajectory. This method was used to determine particle momenta within the range from 0.2 GeV/c up to about 5 GeV/c. The momentum resolution can be calculated using MC simulated tracks. At momenta of about 0.5 GeV/c the difference between the reconstructed and "true" momentum was found to be about 1% while at 4 GeV/c the momentum resolution deteriorates to 4%. The momentum measurement, using the trajectory curvature in the magnetic field, is restricted to particles which pass through all layers of the Spectrometer.

In the PHOBOS experiment a new technique was developed to search for low-p_T particles which range out in the first silicon layers. Momenta of particles measured with this technique range from 30 to 50 MeV/c for pions, from 90 to 130 MeV/c for kaons and from 140 to 210 MeV/c for protons and antiprotons. The reconstruction procedure is described in detail in the next Chapter.

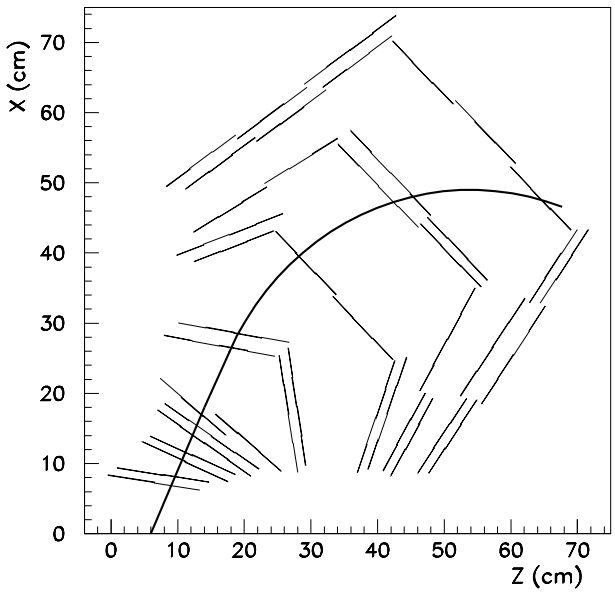

Figure 5.9: *A schematic view of a particle trajectory (solid line) in one arm of the Spectrometer. The trajectory originates at the vertex location of* $Z_{vtx} = 6$ *cm and in the magnetic field-free region, close to the vertex, the particle follows a straight line. Entering into the strong magnetic field (of* 2.2 *T at maximum) the particle trajectory is bent with the curvature depending on particle momentum and charge.*

5.8 Particle Identification

Charged particles, like pions, kaons, protons or antiprotons, traversing through the Spectrometer ionize silicon atoms by means of multiple Coulomb interactions. The mean energy deposited in the detector by a particle through this process is described by the Bethe-Bloch formula [113]. According to the formula, the mean specific ionization energy loss (or stopping power) is very large at small velocities, $\beta << 1$. In the non-relativistic limit the energy loss is dominated by a term proportional to β^{-2}. In the relativistic limit, $\beta \approx 1$, the mean energy loss rises logarithmically with increasing particle momentum. In solid materials, like silicon, this logarithmic increase is suppressed due to the screening effect induced by the atom polarization. Therefore, the mean specific energy loss for all high energy particles is roughly the same and is called the Minimum Ionizing Peak (MIP). One MIP for 300 μm thick silicon detectors in the PHOBOS Spectrometer amounts about 80 keV. The energy deposited in a thin silicon wafer by a single particle significantly fluctuates around the mean value due to statistical fluctuations in the number of Coulomb interactions as well as in the energy loss per single atomic ionization. Fluctuations in the energy loss are well described by the Landau-Vavilov distribution, which is characterized by a long tail extending to large energy values. The PHOBOS Spectrometer has the capability to measure the energy deposited in each single pad of silicon detectors up to about 100 MIP. This feature allows for the identification of particles at both very low and intermediate $p_{_T}$.

The PHOBOS charged particle identification capabilities are summarized in Figs 5.10, 5.11 and 5.12. At very small momenta, particles which range out in first silicon layers are reconstructed using the "stopping" algorithm [27]. Stopping particles deposit most of their energy in silicon detectors. For these particles, one could say that the Spectrometer works as a calorimeter measuring almost the total particle energy. According to the Bethe-Bloch formula, for stopping, non-relativistic particles the product of particle energy and stopping power, dE/dx, measured at a given silicon layer should be proportional to hadron mass. In Fig. 5.10, a scatter plot of the total energy deposited in the first five silicon layers, E_{tot}, and the mean $< E \times dE/dx >$ is shown. A clear separation between $(\pi^+ + \pi^-)$, $(K^+ + K^-)$ and $(p + \overline{p})$ is observed. This identification method is described in more details in the next chapter.

Particle identification in the momentum range from about 0.2 GeV/c to 1.2 GeV/c is provided by measurement of ionization energy losses in all silicon layers of the Spectrometer [114]. The mean energy loss is calculated for each reconstructed truck. The energy of each hit is corrected for the particle path length in silicon and the four hits with largest energies are discarded to restrict large fluctuations in energy loss. Three clear bands, corresponding to pions, kaons and protons, can be seen in Fig. 5.11 where dE/dx is shown as a function of momen-

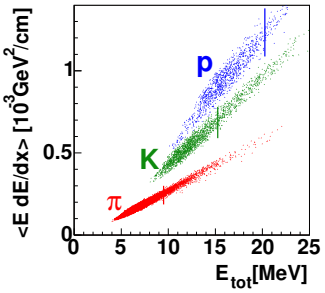

Figure 5.10: *Particle identification at very low transverse momentum is provided by the measurement of stopping particles in the first silicon layers of the Spectrometer [27].*

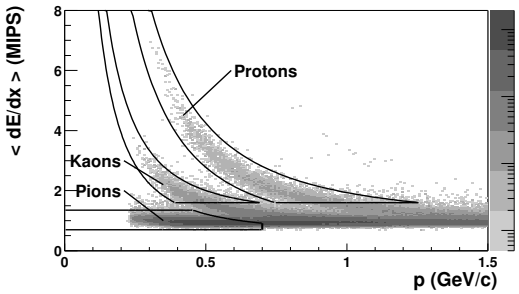

Figure 5.11: *Distribution of the average energy loss in the Spectrometer as a function of momentum is used to identify particles at intermediate p_T [114].*

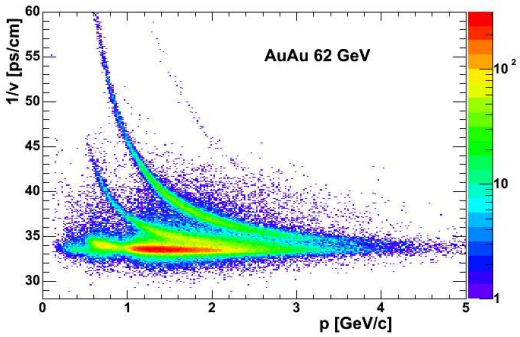

Figure 5.12: *Particle identification at higher p_T is based on the inverse velocity plot provided by the TOF detectors [31].*

0.03

0.3

3

p_T (GeV/c)

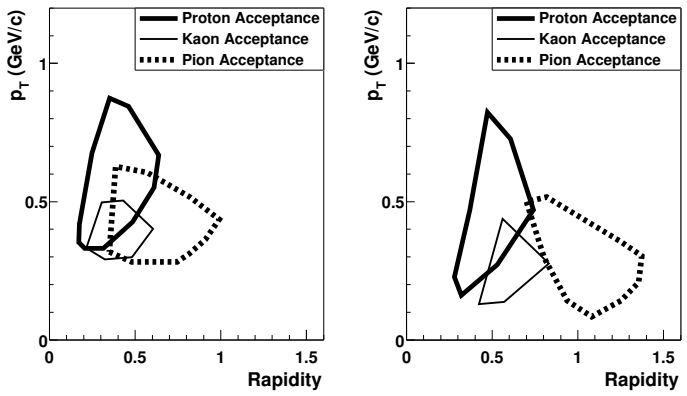

Figure 5.13: *Acceptance contours as a function of transverse momentum and rapidity for pions, kaons, and protons reconstructed in the Au+Au 200 GeV data. The left (right) panel shows the acceptance for particles bending toward (away from) the beam pipe.*

tum. The solid lines represent the cut regions used to count identified particles. The spectrometer geometry and the magnetic field which force particle tracks to bend toward and away from the beam pipe depending on their charge, restrict the acceptance for particle reconstruction to the rapidity and transverse momentum contours presented in Fig. 5.13. As the geometrical layout of the PHOBOS detector leads to an asymmetry in the acceptance and detection efficiency for positively and negatively charged particles for a given magnet polarity, data were taken using both polarities.

Particle identification at higher transverse momenta, up to about 3.5 GeV/c, is provided by the TOF detector [31]. The detector, located at a distance of 5.4 m from the nominal interaction point, see Fig. 5.1, is capable of measuring a particle's time of flight, t_{flight}, with a timing resolution of 140 ps. The particle mass is determined from the following formula:

$$t_{flight} = \frac{Ed}{pc^2} \tag{5.1}$$

where d is the particle trajectory length, p is the particle momentum measured in the Spectrometer while the particle energy, E, is a function of particle mass and momentum. Tracks reconstructed in the Spectrometer are extrapolated to the TOF detector using the Runge-Kutta algorithm. The residual magnetic field in the region between the TOF Counters and the Spectrometer was measured and taken into account in the tracking procedure. To associate a TOF hit with a track reconstructed in the Spectrometer the minimum distance from the TOF hit to the extrapolated particle trajectory is calculated. For example, in the analysis of 62.4 GeV Au+Au data a maximum allowed distance of 4 cm was used

to match the TOF hit with the spectrometer track while in the d+Au 200 GeV data analysis the maximum cut-off value was set at 6 cm. The time of flight, t_{flight}, from the event vertex to the TOF Counters is calculated as a difference of the associated hit timing and the start time obtained from T0 counters. In Fig. 5.12 the inverse velocity, $1/v = t_{flight}/d$, is shown as a function of particle momentum. A good separation of pions and protons up to about 3.5 GeV/c is observed while kaons and pions are clearly separated up to about 2 GeV/c.

5.9 Monte Carlo Simulation of the Detector Response

An important ingredient of most data analyses is the PHOBOS Monte Carlo (PMC) simulation of the detector response. PMC simulations are essential for understanding the detector performance in the particle rich environment of relativistic heavy-ion collisions. PMC simulations also played an important role in the detector optimization [105]. In data analyses, real collision events are mocked up by simulated ones to understand the properties of the reconstruction algorithms in terms of acceptance, efficiency and background contribution.

Two main PMC components can be distinguished. First, nucleus-nucleus collision data (e.g. Au+Au) are simulated using one of the publicly available Monte Carlo generators. In PHOBOS, the following Monte Carlo generators were used to simulate Au+Au and d+Au collisions:

- **HIJING.** Heavy-Ion Jet Interaction Generator (HIJING) [110] is one of the most popular Monte Carlo nuclear collision models used by RHIC experimenters. A basic assumption in this model is that the particle production in the soft sector originates from quark-diquark strings with soft gluon radiation, treated in a way similar to the FRITIOF model [115]. In addition to the gluon radiation in the soft sector, this model introduces mini-jets induced by initial and final state gluon radiation of hard parton scatterings described through pQCD utilizing the PYTHIA code [116]. In the HIJING model the shadowing of nuclear structure functions [110, 117] and jet quenching [74] are included. The latter is attained assuming that hard scattered partons experience energy losses (dE/dx) in the dense partonic medium produced in nuclear collisions.

- **AMPT.** A Multi-Phase Transport (AMPT) model [118] is a Monte Carlo model which uses the HIJING generator to simulate the initial conditions of nuclear collisions, the parton cascade for modeling the partonic scatterings, and A Relativistic Transport (ART) model [119] for describing hadronic scatterings.

- **RQMD.** Relativistic Quantum Molecular Dynamics (RQMD) model [73, 120] assumes that strings and produced resonances can interact during the time evolution of the system produced during nuclear collision. Fragmentation of color strings is performed using JETSET [121]. As a result of string interactions (the formation of color ropes) the pseudo-rapidity densities at mid-rapidity are suppressed.

In the next step, the simulated nuclear collisions are used as an input to the GEANT program [111] which describes the passage of each generated particle through the detector elements. The main part of the GEANT package is the geometrical description of detector apparatus. An extensive effort was made in the PHOBOS experiment to include an accurate description of all detector materials. The detector description includes both active (i.e. sensitive to traversing particles) and inactive elements in the following subsystems:

- **Spectrometer.** The active silicon wafers of the Spectrometer were positioned according to the software alignment procedures which were based on optical survey data. Around volumes of active silicons dead material elements were modeled including electronics, support and cooling system structures as well as many flex cables connecting silicon detectors and racks containing front-end electronics.

- **Octagon, Vertex and Rings Detectors.** Optical survey data were used to position active silicon wafers. A detailed description of the electronics, cables, enclosures and support structures including the ladder support structure of the octagon detector was provided.

- **Paddle Trigger Counters.** The scintillator Paddle Trigger Counters as well as the dead material associated with the detector including PMT tubes, cables and support structures were described.

- **T0.** The description of T0 Čerenkov counters used in the PHOBOS trigger system since the d+Au run was provided both for active (scintillators) and inactive elements.

- **SpecTOF.** A detailed description of the detector based on survey data was provided including both active and inactive elements.

- **TOF.** The two walls of the Time of Flight Counters were described.

- **ZDC.** The description of Zero Degree Calorimeters was provided together with the description of inactive materials around the ZDC detector.

- **Calorimeters.** Three calorimeter detectors were built in the PHOBOS experiment. The calorimeters consisting from thousands of active (fibers) and many inactive volumes were modeled.

- **Magnet.** Magnet coils, yokes and support structures important for background calculations were described.

- **Beam pipe.** Full description of the beam pipe in the PHOBOS experimental area between the two ZDC detectors located at about $\pm 18.5\ m$ was provided. Some elements of the DX magnet were also modeled. The description of the experimental hall including shielding material, concrete support structures, electronics racks, water pipes, cable trays was prepared as well.

Descriptions of geometrical setups corresponding to different Physical Runs are available from an ORACLE data base. The data base, accordingly to a given time stamp, allows to use the same PHOBOS detector description in the data acquisition system (DAQ), data validation and reconstruction as well as in Monte Carlo simulations.

Chapter 6

Measurements of the Transverse Momentum Spectra

Performing measurements of invariant transverse momentum spectra at very low, intermediate and high-p_T in the same detector is unique to the PHOBOS experiment. In PHOBOS, a charged particle's transverse momentum can be measured within the range from 0.03 GeV/c up to about 5 GeV/c using the Spectrometer. Technical aspects of the transverse momentum distribution determination are presented in this Chapter. A new method of track reconstruction and particle identification at very low p_T is presented in detail. Measurement techniques at intermediate and high-p_T are briefly described.

6.1 Particle Yields at Very Low p_T

The measurements of low-p_T particle yields were performed in Au+Au collisions at $\sqrt{s_{NN}} = 200\ GeV$ [27, 29] and 62.4 GeV [30, 31] as well as in d+Au collisions at $\sqrt{s_{NN}} = 200\ GeV$ [30]. The same reconstruction procedure of all data samples was used, with small modifications taking into account different detector geometry setups, Dead Channel Maps (DCM), vertex distributions or trigger configurations. Therefore, in this Section, one data sample (the 15% most central Au+Au collisions at $\sqrt{s_{NN}} = 200\ GeV$) is used to present the reconstruction algorithm.

6.1.1 Reconstruction Procedure

To perform the measurement of particle yields in the low momentum regime a new method was developed to search for particles which range out in the first silicon layers. Based on a Monte Carlo study, searching for particles stopping in the 5^{th} layer was found out to be well-suited for measurements at very low p_T. In this region of the Spectrometer, close to the beam pipe, the residual magnetic

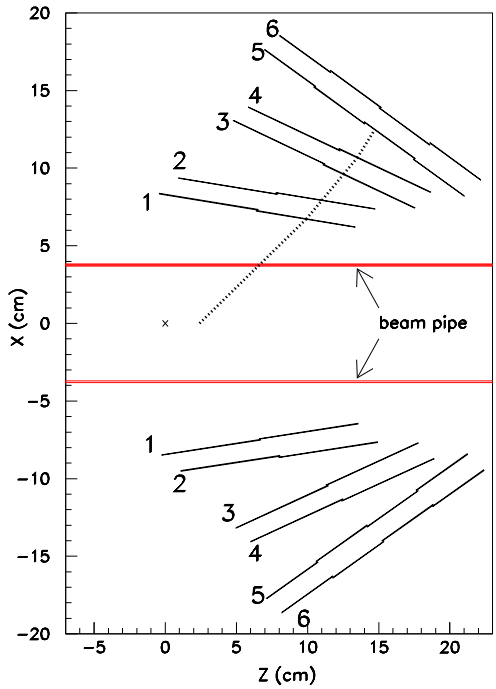

Figure 6.1: *An illustration of a typical stopping particle track. The first silicon layers of the Spectrometer are labeled 1,...,6. The dashed line shows a single π^- track originating at $Z_{vxt} = 2$ cm and stopping in the fifth layer. The origin of the coordinate system, is denoted by $\times$.*

field has negligible effect on the particle trajectories. A typical track of a particle stopping in the fifth silicon layer is shown in Fig. 6.1. As a consequence, in this method there is no charge determination. ADC signals from pads of finely segmented silicon wafers [3] are read-out independently and are processed off-line (calibrated) to determine the ionization energy deposited by charged particles in physical units. A single particle passing through one silicon wafer at a steep angle can produce signals in a few pads as each silicon wafer of the PHOBOS Spectrometer is approximately 300 μm thick. A merging algorithm was applied to sum the energy depositions from neighboring pads and thus provide a precise account of the full ionization energy loss (hit energy). Energy losses of particles ranging out in the fifth layer are much bigger (> 6 times) than the average energy losses of minimum ionizing particle traversing the Spectrometer and are mass dependent. The stopping power of silicon detectors, dE/dx, strongly increases with decreasing particle kinetic energy, as one can see in Fig. 6.2 where dE/dx for stopping protons is plotted as a function of the range. Large

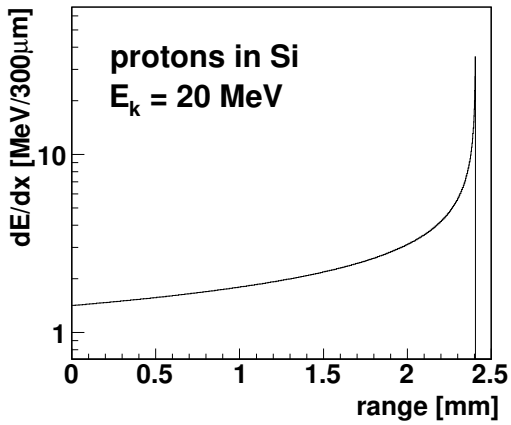

Figure 6.2: *The stopping power (the Bragg Peak), dE/dx (normalized to 300 μm), as a function of the range for protons stopping in silicon. The initial proton kinetic energy was set to $E_k = 20\ MeV$. The plot is based on the PSTAR program [122] which uses methods presented in [123].*

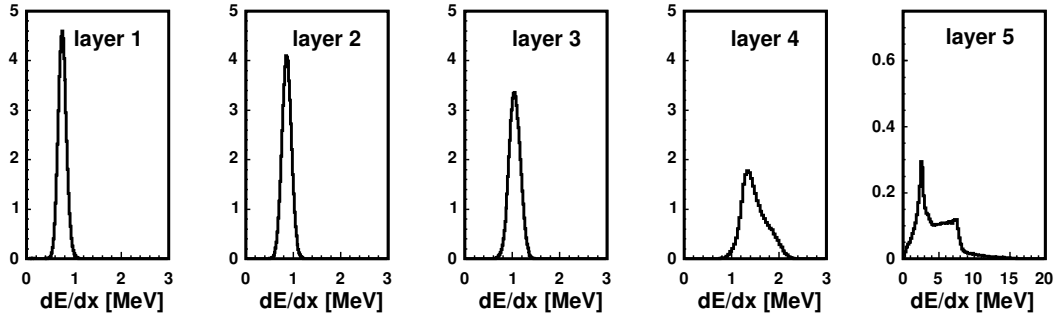

Figure 6.3: *Distributions (normalized to the unit area) of the specific ionization energy loss, dE/dx, in silicon layers 1-5 for simulated charged pions stopping in the fifth layer.*

values of stopping powers make low momentum particles well "visible" on top of all other (faster) particles. The reconstruction of particle trajectories and determination of the particle mass are based on a detailed analysis of the measured energy depositions in the silicon detectors.

A. Stopping Particles. The selection criteria on the energy depositions for potential track candidates are derived from an analysis of single, low momentum particles obtained from GEANT simulations of the PHOBOS detector. In the simulations, all secondary processes, available in the GEANT program, were turned on. To make the simulation accurate in the stopping regime the kinetic energy thresholds for tracking particles were as low as 0.1 MeV. Particles were simulated with $B = 0$ and flat distributions in η and ϕ. The η and ϕ ranges were chosen to cover the Spectrometer area with pseudorapidity range of $-0.55 < \eta < 1.74$ and azimuthal ranges of $-12^o < \phi < 12^o$ and $-168^o < \phi < 192^o$ representing each spectrometer arm - positive (armP) and negative (armN), respectively. The momentum distributions of simulated particles were uniform and limited to the stopping range: $45 - 65$ MeV/c for charged pions; $120 - 170$ MeV/c for charged kaons; $180 - 260$ MeV/c for protons and antiprotons. The samples used to define the reconstruction cuts contain only those low momentum particles whose passage through the detector is terminated in the fifth layer and which give hits in layers 1-5. The kinetic energy of particles stopping in the 5^{th} layer depend on the particle mass and are equal to about 8 MeV for charged pions, 19 MeV for charged kaons and 21 MeV for protons and antiprotons.

B. Selection of Hits with Large Energy Depositions. In Fig. 6.3 the distributions of energy depositions, dE/dx, normalized to 300 μm of silicon, in layers 1-5 are shown for simulated charged pions stopping in the 5^{th} layer. For heavier charged particles (kaons, protons and antiprotons) the energy depositions are larger. The first step of the reconstruction algorithm is to only accept hits with an energy larger than 0.5 MeV, event-by-event. These large energy hits constitute

just a tiny fraction of all hits, $< 1\%$. Due to this cut, the bulk of hits with smaller energy deposits are rejected and only a small fraction of hits belonging to stopping particles are lost (about 1%). To proceed with the reconstruction, at least one large energy hit is required in every silicon layer 1-5 for each spectrometer arm.

C. Formation of Track Candidates. The set of hits with large energy deposits (defined above) is used to form track candidates for low momentum particles. For each event, all possible combinations of 5-hit tracks are formed, with each hit belonging to a different silicon layer 1-5.

D. Preliminary Angular Cut. In this step of the reconstruction process all 5-hit tracks with unreasonably large deviations from a straight-line trajectory are rejected. Particle trajectories should follow a roughly straight line as the magnetic field in the region close to the beam pipe is negligible. The polar, θ, and azimuthal, ϕ, angles are calculated for each track hit using its location in the detector and known position of the Au+Au collision vertex. For each pair of hits from adjacent silicon layers (1-2, 2-3, 3-4, 4-5) angular differences $\Delta\theta$ and $\Delta\phi$ are calculated and compared to the differences obtained for simulated stopping particles. The angular differences for particles passing through the beam pipe and silicon detectors are determined by multiple scattering and are proportional to $1/\beta p$ [113], where β and p are the velocity and momentum of scattered particle. Thus, the largest average scattering of particles stopping in the 5^{th} layer occurs for pions as the typical momentum for stopping pions ($\sim 55\ MeV/c$) is much smaller that those for kaons ($\sim 125\ MeV/c$) and protons ($\sim 200\ MeV/c$). Therefore, at this stage of the reconstruction when particle mass is not known yet, the angular differences are compared to the scattering of stopping pions. The distributions of angular differences of θ and ϕ obtained for each pair of adjacent hits from the sample of simulated stopping pions were cut to reject 0.5% of the largest differences. This procedure provided maximal allowed differences which were used in the reconstruction algorithm: $|\Delta\theta| < (2.2^o, 4.1^o, 2.6^o, 8.0^o)$, $|\Delta\phi| < (2.8^o, 4.3^o, 3.1^o, 7.1^o)$ for each pair of adjacent silicon layers.

E. Mass Hypothesis. The mass of a track candidate is determined by matching its energy deposition, $(dE/dx)_i$, at the first four silicon layers ($i = 1, ..., 4$) to the mean energy depositions of simulated stopping $(\pi^+ + \pi^-)$, $(K^+ + K^-)$ and $(p + \overline{p})$. It is checked for each particle type, if the energy depositions satisfy the following conditions (mass hypothesis):

$$|(dE/dx)_i - < dE/dx >_i | < 1.4\ \sigma_i, \quad i = 1, ..., 4, \tag{6.1}$$

where the mean $< dE/dx >_i$ and RMS, σ_i, are calculated from the dE/dx distributions for simulated stopping $(\pi^+ + \pi^-)$, $(K^+ + K^-)$ and $(p + \overline{p})$. The mean

Table 6.1: *Mean values of dE/dx (in MeV and normalized to 300 μm of silicon) for simulated stopping $(\pi^+ + \pi^-)$, $(K^+ + K^-)$ and $(p + \overline{p})$ for both Spectrometer arms (P, N) as a function of silicon layer. The measured thicknesses of silicon wafers were used here which leads to some small differences between the two spectrometer arms.*

silicon layer number	$(\pi^+ + \pi^-)$		$(K^+ + K^-)$		$(p + \overline{p})$	
	armP	armN	armP	armN	armP	armN
1	0.745	0.762	1.301	1.330	1.733	1.776
2	0.853	0.873	1.490	1.524	1.986	2.038
3	1.037	1.059	1.810	1.847	2.414	2.470
4	1.478	1.493	2.558	2.582	3.436	3.487

Table 6.2: *RMS values, σ (in MeV), of dE/dx distributions for simulated stopping particles for both Spectrometer arms as a function of silicon layer.*

silicon layer number	$(\pi^+ + \pi^-)$		$(K^+ + K^-)$		$(p + \overline{p})$	
	armP	armN	armP	armN	armP	armN
1	0.090	0.094	0.134	0.141	0.165	0.176
2	0.101	0.103	0.152	0.153	0.192	0.191
3	0.124	0.126	0.201	0.203	0.256	0.257
4	0.274	0.281	0.459	0.474	0.617	0.629

and RMS values used in Eq. 6.1 are quoted in Table 6.1 and 6.2.

The mass is determined according to the type of particle for which the condition (Eq. 6.1) is satisfied. Single track candidates can fulfill the mass hypothesis for only one particle type, either for $(\pi^+ + \pi^-)$, $(K^+ + K^-)$ or $(p + \overline{p})$. All track candidates which do not fulfill these conditions are removed from the analysis. The dE/dx values of track candidates (from armN), which satisfy Eq. 6.1, are shown in Fig. 6.4 as a function of the silicon layer.

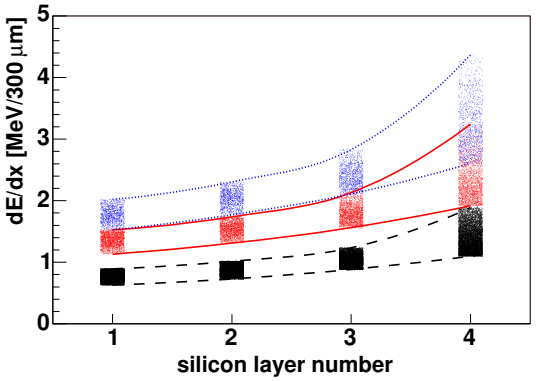

Figure 6.4: *dE/dx values of track candidates in the 15% most central Au+Au collisions at $\sqrt{s_{NN}} = 200$ GeV as a function of silicon layer [27]. Lines show dE/dx bands, which limit the dE/dx values according to Eq. 6.1, obtained from simulated stopping particles. Dashed, solid and dotted lines correspond to $(\pi^+ + \pi^-)$, $(K^+ + K^-)$ and $(p + \overline{p})$, respectively.*

F. Momentum Hypothesis. Reconstruction of MC data indicate that the sample of track candidates, after applying mass cuts defined by Eq. 6.1, is contaminated with tracks of higher momentum particles. To limit this contamination, cuts on the total energy deposited in all five silicon layers, $E_{tot} = E_1 + E_2 + E_3 + E_4 + E_5$, were applied. These cuts are called the momentum hypothesis cuts. The total energy, E_{tot}, has to be corrected for the contribution from annihilation and decay products of stopping particles taking place in the last layer. To this end, instead of using the measured energy deposition in the fifth layer, E_5 is calculated for each track candidate with the help of mass parameters defined as

$$(M_p)_i = (dE/dx)_i \sum_{k=i}^{5} E_k, \tag{6.2}$$

for each first four silicon layers, $i = 1, ..., 4$. E_k denotes the energy deposited in the k^{th} layer. For non-relativistic particles, the mass parameter $(M_p)_i$ depends only on the particle mass, since

$$(dE/dx)_i \sim \frac{1}{\beta^2} \quad and \quad \sum_{k=i}^{5} E_k \sim \frac{m\beta^2}{2}. \tag{6.3}$$

The product of the two terms in Eqs 6.3 results in the β dependence canceling out. For a given particle $(M_p)_i$ values should be the same for every silicon layer $i = 1, ..., 4$. This property of the mass parameter is used to estimate the energy deposition in the last layer. The value, E_5, is then just fitted to minimize the layer dependence of mass parameters. Having estimated E_5, we now can calculate the average mass parameter, M_p, and the total deposited energy, E_{tot}. Maximum values of E_{tot}, used to restrict momenta of reconstructed particles, were adjusted using simulated stopping particles. Fig. 6.5 shows a scatter plot of M_p vs. E_{tot}, for particles stopped in the fifth silicon layer satisfying the selection criteria on dE/dx in the first four layers (Eq. 6.1). Clearly separated bands corresponding to particles of different masses are apparent. Setting the upper limits of E_{tot} equal to $9.5MeV$, $15.25MeV$ and $20.25MeV$

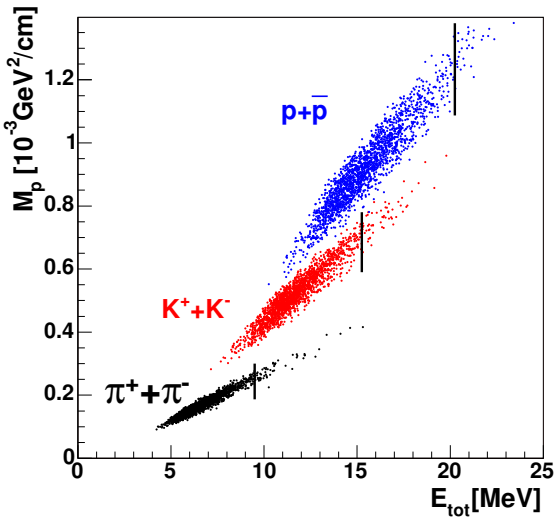

Figure 6.5: *(M_p, E_{tot}) scatter plot for simulated particles (with $\theta > 60^o$) stopping in the fifth layer after restricting dE/dx values using Eq. 6.1. The upper limits on E_{tot} are marked by vertical lines.*

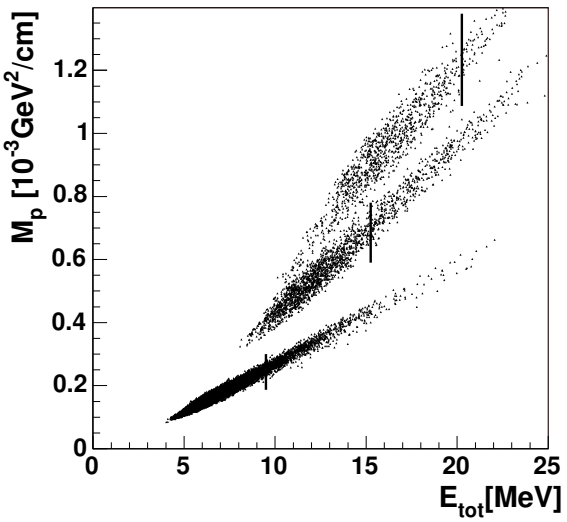

Figure 6.6: (M_p, E_{tot}) *scatter plot for track candidates in experimental data of Au+Au collisions at* $\sqrt{s_{_{NN}}} = 200$ *GeV [27]. The vertical lines (momentum hypothesis) restrict reconstructed tracks to the regime of stopping particles, shown in Fig. 6.5. All track candidates with the emission angles larger than* 60^o *are shown.*

pair of	$(K^+ + K^-)$		$(p + \overline{p})$	
silicon layers	$\Delta\theta$	$\Delta\phi$	$\Delta\theta$	$\Delta\phi$
1-2	1.2	1.8	1.1	1.5
2-3	1.9	2.8	1.9	2.4
3-4	1.2	1.9	1.2	1.6
4-5	3.5	4.7	1.5	4.1

Table 6.3: *Upper limits on the angular differences (in degrees) used to restrict large deviation of* $(K^+ + K^-)$ *and* $(p + \overline{p})$ *trajectories from straight-line.*

for $(\pi^+ + \pi^-)$, $(K^+ + K^-)$ and $(p + \overline{p})$ at $\theta > 60^o$, rejects only a small fraction (<0.5%) of the simulated particles. For smaller emission angles, $\theta \leq 60^o$, the corresponding values are equal 10.25 MeV, 17.0 MeV and 22.5 MeV. The momentum hypothesis imposed on experimental data, see Fig. 6.6, restricts particles momenta to the range of stopping particles. The θ-dependence of this cut is introduced to take into account the larger amount of detector material which particles emitted at smaller angles have to traverse. The observed positive correlation between M_p and E_{tot} results from the calculation of E_5. Fluctuations in the energy losses along the particle path make the calculated energy E_5 smeared around the true value. This effect, however, does not spoil the particle identification, as a clear separation in the M_p and E_{tot} plane is observed both for Monte Carlo (Fig. 6.5) and experimental data (Fig. 6.6).

G. Angular Cut. As discussed in Section 6.1.1.D, in the momentum range of stopping particles, deviations of particle trajectories from the straight-line are smaller for $(K^+ + K^-)$ and $(p + \overline{p})$ than for $(\pi^+ + \pi^-)$. Thus, additional angular cuts on identified $(K^+ + K^-)$ and $(p + \overline{p})$ are imposed to further reject false candidates. The upper limits on the angular differences were calculated in the same way as described in Section 6.1.1.D. The angular cut parameters used to restrict $(K^+ + K^-)$ and $(p + \overline{p})$ trajectories are shown in Table 6.3.

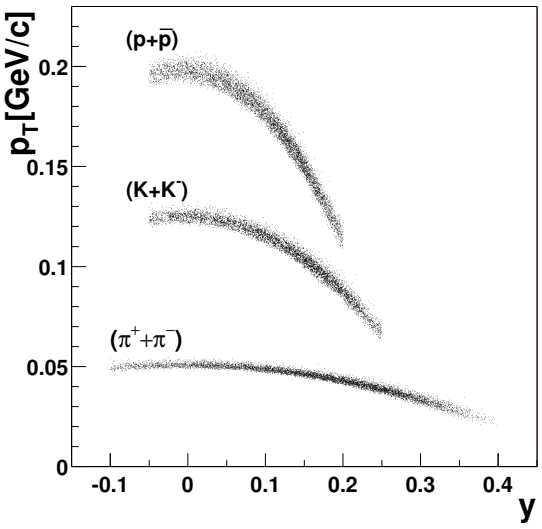

Figure 6.7: *Acceptance plot in transverse momentum (p_T) and rapidity (y) plane for charged pions, kaons and protons/antiprotons.*

H. Track Selection. In the final step of the reconstruction procedure validation of track candidates, which share hits, is performed. For each track candidate χ^2 is calculated from its energy depositions, $(dE/dx)_i$, in silicon layers 1-4:

$$\chi^2 = \sum_{i=1}^{4}((dE/dx)_i - < dE/dx >_i)^2/\sigma_i^2, \tag{6.4}$$

where parameters $< dE/dx >_i$ and σ_i are quoted in Table 6.1 and Table 6.2, respectively. If two tracks share at least one hit the track with the smaller χ^2 is accepted. If the tracks share all hits in the first four silicon layers then the track with the larger energy deposit in the fifth layer is selected, because there is a larger probability that the lower energy hit is random.

I. Momentum of Reconstructed Particles. Particles which pass the detector encounter very small amount of the material contained in the beryllium pipe (1 mm thick) and first silicon layers. Thus, momenta of reconstructed particles are confined to a narrow range at very low p_T. This feature is apparent from the acceptance plot, shown in Fig. 6.7, where each point represents a reconstructed particle from simulated data in the transverse momentum (p_T) and rapidity (y) plane. The measurements are confined to the mid-rapidity region ($-0.1 < y < 0.4$) and cover a narrow range of transverse momentum between 20 and 55 MeV/c for charged pions, 60 and 130 MeV/c for charged kaons and 110 and 210 MeV/c for protons and antiprotons. At larger rapidities, tracks with smaller transverse momenta are reconstructed due to a smaller $sin\theta$ factor in the p_T definition. For measured particles, the total momentum is determined using MC simulations. It is assumed that each reconstructed track has a momentum which corresponds to an average momentum of simulated particles at a given θ.

	Number of tracks
Preliminary angular cut	525000
Mass hypothesis	32400
Momentum hypothesis	26200
Angular cut	24500
Track selection	16900

Table 6.4: *A summary of all reconstructed tracks in both arms of the Spectrometer in 2 million events of the 15% most central Au+Au collisions at* $\sqrt{s_{_{NN}}} = 200\ GeV$.

The transverse momentum resolution of this method is estimated to be 5%. For each reconstructed track, the θ and φ emission angles are defined by the vertex position and the position of the first hit (in layer 1). The angular resolution is of the order of 1^o.

The reconstruction procedure was applied to the data of Au+Au collisions at $\sqrt{s_{_{NN}}} = 200\ GeV$ and 62.4 GeV as well as to d+Au collisions at $\sqrt{s_{_{NN}}} = 200\ GeV$. To match the acceptance of the Spectrometer the interaction vertex along the beam axis was restricted to the range from $-7\ cm$ to $14\ cm$. The trigger, centrality and vertex selection procedures, described in Chapter 5, yielded 2.0×10^6 of the 15% most central Au+Au collisions at $\sqrt{s_{_{NN}}} = 200\ GeV$ from the data collected during the physics Run-02 at RHIC. For that data, the number of tracks obtained in subsequent steps of the reconstruction procedure, is shown in Table 6.4. The total number of reconstructed $(\pi^+ + \pi^-)$, $(K^+ + K^-)$ and $(p + \overline{p})$ in both spectrometer arms is 14000, 1900 and 1000, respectively.

The reconstruction of Au+Au collisions at $\sqrt{s_{_{NN}}} = 62.4\ GeV$ was based on the data collected during Run-04. The full data set was analyzed to limit statistical errors. The trigger and centrality procedures yielded 4.8×10^6 events within centrality interval 0-50%. The reconstruction algorithm, was used to obtain yields of low-$p_{_T}$ $(\pi^+ + \pi^-)$, $(K^+ + K^-)$ and $(p + \overline{p})$ within three centrality bins: 0-15%, 15-30% and 30-50%. The analysis of d+Au data was based on full Run-03 data set. The total number of d+Au minimum bias events selected for the reconstruction was 9.91 M.

6.1.2 Acceptance, Efficiency and Background Corrections

The raw number of reconstructed tracks is used to determine the invariant transverse momentum distributions integrated over azimuthal angle, defined as:

$$Y = \frac{1}{2\pi} \frac{1}{N_{ev}} \frac{1}{p_{_T}} \frac{d^2N}{dp_{_T}dy}, \tag{6.5}$$

where N denotes the number of produced particles as a function of transverse momentum, $p_{_T}$, and rapidity, y. To determine the invariant transverse momentum distributions, the reconstructed $(\pi^+ + \pi^-)$, $(K^+ + K^-)$ and $(p + \overline{p})$ samples are

Table 6.5: *Phase space regions used in the determination of particle p_T spectra.*

$< p_T >$, (GeV/c)	Δy	Δp_T, (GeV/c)	$Z_{vtx}(cm)$
PIONS			
0.031	$0.3 \div 0.4$	$0.020 \div 0.040$	$-7 \div -1$
0.044	$0.2 \div 0.3$	$0.031 \div 0.054$	$-4 \div 6$
0.048	$0.1 \div 0.2$	$0.040 \div 0.056$	$2 \div 9$
0.053	$-0.1 \div 0.1$	$0.045 \div 0.060$	$7 \div 12$
KAONS			
0.096	$0.15 \div 0.25$	$0.060 \div 0.125$	$-4 \div 5$
0.116	$0.10 \div 0.15$	$0.098 \div 0.132$	$0 \div 9$
0.123	$0.05 \div 0.10$	$0.110 \div 0.135$	$3 \div 11$
0.128	$-0.05 \div 0.05$	$0.118 \div 0.138$	$9 \div 13$
PROTONS, ANTIPROTONS			
0.143	$0.15 \div 0.20$	$0.105 \div 0.175$	$-7 \div 5$
0.172	$0.10 \div 0.15$	$0.140 \div 0.200$	$-3 \div 8$
0.190	$0.05 \div 0.10$	$0.165 \div 0.213$	$1 \div 11$
0.206	$-0.05 \div 0.05$	$0.185 \div 0.225$	$7 \div 13$

divided into narrow $(\Delta y, \Delta p_T)$ bins, shown in Table 6.5. Particles from a given bin of y and p_T are restricted to a certain vertex range due to the detector geometry. For each $(\Delta y, \Delta p_T)$ bin, the expression Eq. 6.5 can be written as:

$$Y = \frac{1}{2\pi} \frac{1}{< p_T >} \frac{N_{rec}^{corr}}{\Delta p_T \Delta y}, \tag{6.6}$$

where $< p_T >$ denotes the mean transverse momentum within the Δp_T interval, while the total number of particles, N_{rec}^{corr}, in the $(\Delta y, \Delta p_T)$ bin is obtained from the following formula:

$$N_{rec}^{corr} = 15 < C_Y^{eff} * N_{rec} > . \tag{6.7}$$

In Eq. 6.7 the raw number of reconstructed tracks per event, N_{rec}, are corrected for acceptance and efficiency factors by C_Y^{eff}. C_Y^{eff} accounts for geometrical acceptance, reconstruction and particle identification inefficiencies, absorption in the beam pipe and particle decays. These correction factors are computed for each arm within the azimuthal angle restricted to the spectrometer acceptance, i.e. to $\pm 12^o$. Therefore, the multiplier 15 is required to obtain the number of particles in the full azimuthal angle. For each $(\Delta y, \Delta p_T)$ window, the correction factors, C_Y^{eff}, are calculated within 1 *cm*-bins of the Z_{vtx} range and the mean in Eq. 6.7 is calculated over the full Z_{vtx} interval, quoted in Table 6.5.

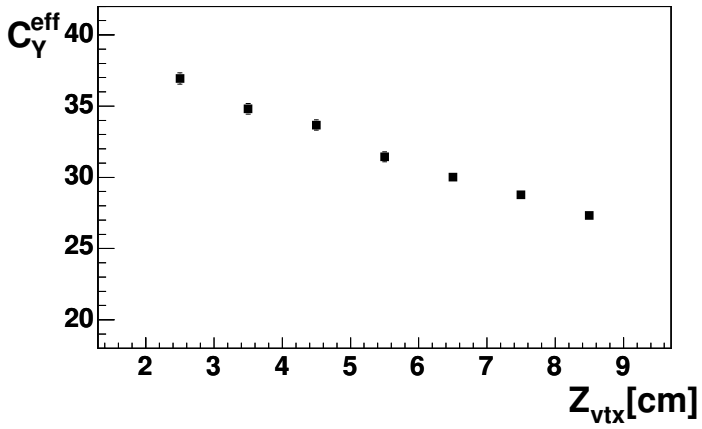

Figure 6.8: *Acceptance and efficiency corrections as a function of Z_{vtx} for reconstructed pions with rapidity and transverse momentum within the range:* $0.1 < y < 0.2$ *and* $40\ MeV/c < p_{_T} < 56\ MeV/c$. *The correction factors are obtained with the embedding procedure applied to the Au+Au data at* 200 *GeV for the spectrometer arm at the negative side of X-axis.*

The factors C_Y^{eff} are computed using an embedding procedure. In this procedure, a large number of single particles are generated and tracked through the detector using GEANT. Next, the generated raw data from a single particle is embedded into an experimental event and then the whole reconstruction on the combined event is performed. For this procedure, a representative set of real events was selected. The reconstruction is defined as successful if the reconstructed track has the same particle identity (PID) as that of the embedded track and its hits match the hits of the embedded track. The efficiency and acceptance correction (C_Y^{eff}) is then calculated as a ratio of the total number of embedded tracks, N_{emb}, to the number of reconstructed tracks, N_{emb}^{rec}:

$$C_Y^{eff} = \frac{N_{emb}}{N_{emb}^{rec}}. \tag{6.8}$$

In the embedding procedure rapidity and azimuthal angle distributions of simulated particles within $(\Delta y, \Delta p_{_T})$ window are uniform while their $p_{_T}$ distribution is adopted from the HIJING model. Simulations of single particles are done with the same magnetic field configuration, detector geometry and vertex distribution as that of experimental events as well as with the Dead Channel Map (DCM) masking electronic channels which do not work properly. The number of reconstructed tracks within the embedding procedure is about 3×10^5 for each $\pi^{\pm}$, $K^{\pm}$, and $p^{\pm}$ in both arms, while the total number of embedded track is about 30 times larger. As an example, the correction factors for pions, for the phase space window: $0.1 < y < 0.2$ and $40\ MeV/c < p_{_T} < 56\ MeV/c$ are shown in Fig. 6.8.

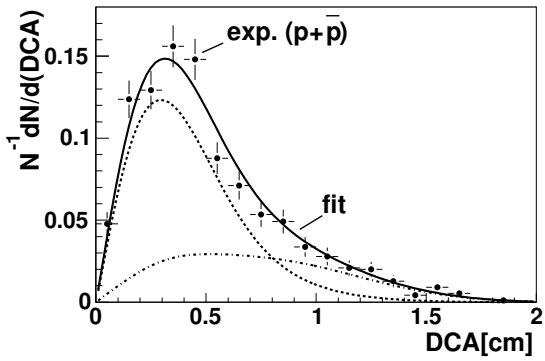

Figure 6.9: *DCA distribution for reconstructed $(p + \overline{p})$ tracks in the data sample (points with the error bars). The result of the fit to the measured distribution (see text for details) is denoted by the solid curve. The dashed (dashed-dotted) curve shows the contribution from primary (background) simulated particles.*

The invariant $p_{_T}$ spectra of $(\pi^+ + \pi^-)$, $(K^+ + K^-)$ and $(p + \overline{p})$ can be obtained by applying Eqs 6.6 and 6.7 to the reconstructed data sample. However, the particle spectra are not yet corrected for backgrounds including feed-down from weak decays, contributions from secondary, misidentified and ghost particles (i.e. particles with at least one random hit in the first four silicon layers).

To estimate the background contamination of the $(p+\overline{p})$ yield, we analyze the distribution of the distance of closest approach (DCA) from the vertex position to the particle trajectory, determined by a straight line passing through the hits in the first and third spectrometer layer. The experimental DCA distribution is found to be significantly broader than the DCA distribution for reconstructed primary proton tracks, see Fig. 6.9. Based on MC studies, it was found that the excess of tracks with large DCA can be attributed to background particles which do not originate at the vertex position. For protons and antiprotons the dominant background contributions include secondary particles produced in the beam pipe and detector material as well as products from weak decays. Hence, the experimental DCA distribution is described by a superposition of the following functions:

$$F_{DCA} = (1 - \alpha_p)F_P + \alpha_p[\beta F_S + (1 - \beta)F_D], \tag{6.9}$$

where the functional forms were taken as the parameterization of the DCA distributions for reconstructed primary protons (F_P), secondary protons (F_S) and protons from weak decays (F_D). The coefficient α_p in the above expression denotes the total background contribution to the measured $(p + \overline{p})$ yield, while β describes the fraction of particles from secondary interactions and particles from weak decays in the background. The parameterized shapes of the DCA distributions for reconstructed primary $(p + \overline{p})$ were obtained from an analysis of single particles successfully reconstructed in the embedding procedure. The shape of

the DCA distributions for secondary and feed-down protons were obtained from full PMC simulations. Analysis of large samples of simulated HIJING events (about 400 thousand Au+Au events) was necessary to obtain a reasonable parameterization. However, even with the large number of simulated MC events the number of background particles is too low to obtain a good estimate of the β parameter. Therefore, instead of disentangling the two background components, we fit the experimental distribution with one free parameter describing the fraction of the total background, α_p, while a relative contribution from secondary and feed-down protons is fixed with β varied from 0 to 1. An example of the fit assuming equal weights of the two background components is shown in Fig. 6.9. The fitted fraction of background particles, α_p, averaged over a whole range of β values is $0.31 \pm 0.04(stat.) \pm 0.19(syst.)$. The large systematic error assigned to this fraction reflects the dependence of the total background estimate on the relative importance of secondary and feed-down contributions. The determined fraction of background particles agrees with the estimate of 0.34 ± 0.03, obtained directly from the reconstruction of HIJING events. However, we cannot rely solely on HIJING simulations as a measure of the background in $(p + \overline{p})$ data, since HIJING largely overestimates the yields of low momentum protons and antiprotons. The ratio of the measured $(p + \overline{p})$ yield corrected for the background to the HIJING prediction is: $f_p = 0.183 \pm 0.014$.

The method of the background determination (based on DCA distributions) could be applied to $(p + \overline{p})$ as the DCA distribution of reconstructed primary $(p+\overline{p})$ is narrower than the distribution of protons and antiprotons from secondary interactions and decays. This requirement is not fulfilled for primary $(\pi^+ + \pi^-)$ and $(K^+ + K^-)$ as pions and kaons are subject to larger multi-scatterings than primary $(p+\overline{p})$ (see Section 6.1.1.D). Thus, to estimate backgrounds in pion and kaon samples we rely on Monte Carlo simulations. The background corrections to the yields of charged pions and kaons can be estimated from the reconstructed tracks of simulated events. The truth information available in Monte Carlo data is used to classify reconstructed particles as coming from primary particles, from secondaries (e.g. low-p_T proton originating from a primary π^- interacting with the beryllium pipe), from feed-down from weak decays, misidentified and random (i.e. ghost) particles. A breakdown of these different contributions are shown in Table 6.6. Interestingly, there is no $(\pi^+ + \pi^-)$ contamination in reconstructed $(K^+ + K^-)$ and $(p + \overline{p})$ samples, although the abundance of $(\pi^+ + \pi^-)$ is much larger, indicating that the reconstruction procedure is a robust method for pion separation from kaons and protons.

As noted previously, the HIJING model does not describe correctly the $(p+\overline{p})$ yields. Thus, it is important to "tune" HIJING yields to match the experimental one for a better estimation of the background correction factors. This adjustment is crucial for evaluating the background correction for charged kaons which is dominated by misidentified protons (see Table 6.6). For illustration, the charged

Table 6.6: *Fractions (in %) of primary and background particles in the samples of reconstructed $(\pi^+ + \pi^-)$, $(K^+ + K^-)$ and $(p + \overline{p})$ in the 15% most central Au+Au fully simulated HIJING events.*

$(\pi^+ + \pi^-)$ **sample**	
Primary $(\pi^+ + \pi^-)$	77.4 ± 4.1 %
Secondary $(\pi^+ + \pi^-)$	2.3 ± 0.5 %
$(\pi^+ + \pi^-)$ from decays	8.8 ± 1.1 %
$(K^+ + K^-)$ identified as $(\pi^+ + \pi^-)$	2.1 ± 0.5 %
$(p + \overline{p})$ identified as $(\pi^+ + \pi^-)$	2.1 ± 0.5 %
$(\mu^+ + \mu^-)$ identified as $(\pi^+ + \pi^-)$	1.2 ± 0.4 %
Random hits in layers 1-4	6.2 ± 0.9 %
total background	22.6 ± 1.7 %
$(K^+ + K^-)$ **sample**	
Primary $(K^+ + K^-)$	76.0 ± 8.2 %
Secondary $(K^+ + K^-)$	0.0 %
$(K^+ + K^-)$ from decays	1.0 ± 0.7 %
$(p + \overline{p})$ identified as $(K^+ + K^-)$	20.5 ± 3.5 %
Random hits in layers 1-4	2.5 ± 1.1 %
total background	24.0 ± 3.5 %
$(p + \overline{p})$ **sample**	
Primary $(p + \overline{p})$	67.0 ± 7.1 %
Secondary $(p + \overline{p})$	10.7 ± 2.3 %
$(p + \overline{p})$ from decays	20.5 ± 3.3 %
$(K^+ + K^-)$ identified as $(p + \overline{p})$	1.3 ± 0.8 %
Random hits in layers 1-4	0.4 ± 0.4 %
total background	33.0 ± 3.8 %

kaon yields will be used to demonstrate the tuning procedure. First, we define the tuning factors, f_{ID}, which account for differences in the yield of primary particles from the HIJING model and from experimental measurement:

$$f_{ID} = (1 - \alpha_{ID}) \frac{Y_{exp}^{ID}}{Y_{Hij}^{ID}}, \tag{6.10}$$

where Y_{exp}^{ID} is the acceptance and efficiency corrected measured yield, Y_{Hij}^{ID} is the HIJING yield of primary particles, while $(1 - \alpha_{ID})$ is the fraction of primary particles in the measured yield. In the following, we assume that background contributions scale with the total number of reconstructed tracks. This assumption is, to a good approximation, valid for the reconstructed HIJING events. Taking, the appropriately tuned HIJING particle yields of reconstructed primary kaons ($Y_{p,Hij}^{K}$), protons misidentified as kaons ($Y_{m,Hij}^{K}$), ghost tracks ($Y_{r,Hij}^{K}$) and

$< p_T > (GeV/c)$	α_π	f_π
0.031	0.31 ± 0.04	0.80 ± 0.06
0.044	0.27 ± 0.02	0.71 ± 0.03
0.048	0.22 ± 0.02	0.75 ± 0.03
0.053	0.22 ± 0.02	0.86 ± 0.03

Table 6.7: *Background contributions (α_π) and HIJING tuning factors (f_π) for charged pions as a function of transverse momentum.*

from weak decays ($Y^K_{d,Hij}$) we can calculate f_K and α_K from the two following equations:

$$(1-\alpha_K) = \frac{Y^K_{p,Hij} f_K}{(Y^K_{p,Hij} + Y^K_{r,Hij}) f_K + Y^K_{m,Hij} f_p + Y^K_{d,Hij}} \tag{6.11}$$

$$(1-\alpha_K) Y^K_{exp} = Y^K_{p,Hij} f_K. \tag{6.12}$$

Using the acceptance and efficiency corrected yield of charged kaons (Y^K_{exp}), the previously determined tuning factor f_p, the true HIJING yields and Eqs 6.11 and 6.12 allow the fraction of primary kaons and the tuning factor f_K to be calculated. The results are $1-\alpha_K = 0.90 \pm 0.04$ and $f_K = 0.61 \pm 0.02$. The estimated kaon background is significantly lower than the value quoted in Table 6.6, due to the larger ratio of proton to kaon yields in the HIJING model than in the experimental data. The kaon background is dominated by misidentified protons.

The same procedure was applied to charged pions using the already known tuning factors f_p and f_K. The large statistics available for the reconstructed pions allows the background corrections to be determined for each p_T bin separately. In Table 6.7 charged pion background estimates and the tuning factors are shown for each p_T bin. As one can see from Tables 6.6 and 6.7 the tuning procedure has a minor impact on background corrections of charged pions, giving the same background levels in the data and in simulations. In this case, feed down from weak decays and ghost tracks are the main source of the background contamination.

Various sources of systematic error related to the background determination as well as to the analysis method and detector effects were investigated. A detailed description of the procedure used to calculate each systematic error contribution is presented in Appendix A. The final systematic uncertainties are shown in Table 6.8. The individual contributions from different sources of systematic

Source	$\pi^+ + \pi^-$	$K^+ + K^-$	$p + \overline{p}$
Method	7.5	12.1	13.5
Detector	3.8	7.7	9.9
Background	9.0	10.0	27.5
Total	12.3	17.5	32.2

Table 6.8: *Systematic errors (%) related to background corrections, the analysis method, and detector effects on the measured particle yields in the 15% most central Au+Au collisions at* $\sqrt{s_{NN}} = 200\ GeV$.

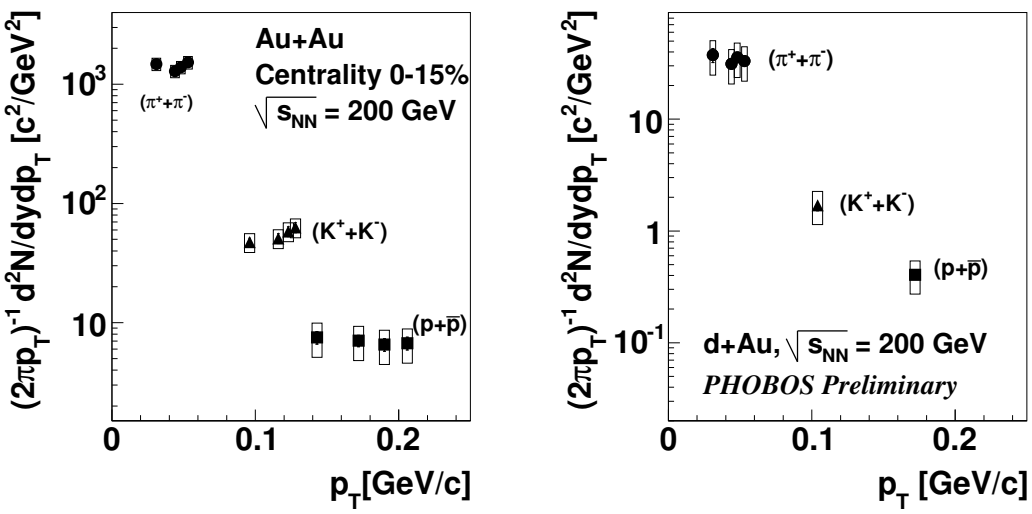

Figure 6.10: *Invariant p_T spectra of $(\pi^+ + \pi^-)$, $(K^+ + K^-)$ and $(p+\overline{p})$ in the 15% most central Au+Au (left panel) [27] and in d+Au collisions (right panel) [30] at $\sqrt{s_{NN}} =$ 200 GeV. The boxes show the systematic uncertainties.*

uncertainty are added in quadrature to derive the total systematic error for these measurements: 12% for $(\pi^+ + \pi^-)$, 18% for $(K^+ + K^-)$ and 32% for $(p + \overline{p})$.

6.1.3 Invariant p_T Spectra

Data tables of the fully (acceptance, efficiency and background) corrected p_T spectra of $(\pi^+ + \pi^-)$, $(K^+ + K^-)$ and $(p + \overline{p})$ in Au+Au collisions at $\sqrt{s_{NN}} =$ 200 GeV [27] and 62.4 GeV [30, 31] as well as in d+Au collisions at $\sqrt{s_{NN}} =$ 200 GeV [30] are presented in Appendix B. The statistical errors quoted in these tables take into account the limited number of reconstructed tracks, errors connected with the acceptance and efficiency correction procedure as well as the statistical errors of the background corrections which depend on the statistics of different types of reconstructed tracks from the Monte Carlo data. The results for the 15% most central Au+Au and for d+Au collisions at $\sqrt{s_{NN}} =$ 200 GeV are also depicted in Fig. 6.10. Due to the low statistics of reconstructed $(K^+ + K^-)$ and $(p + \overline{p})$ tracks in d+Au sample, only one data point for each particle type was calculated.

6.2 Identified Particle Yields at Intermediate p_T

In PHOBOS, identified particle yields at intermediate p_T were obtained in Au+Au collisions at $\sqrt{s_{NN}} = 62.4\ GeV$ [30, 31] and in d+Au collisions at $\sqrt{s_{NN}} = 200\ GeV$ [30, 124]. Analyses at very low and intermediate p_T were performed in parallel to provide comparable results in terms of centrality and trigger cuts used to select events. In this Section some technical details of particle reconstruction and invariant yield determination at intermediate p_T are presented. The same reconstruction procedure, with some minor modifications, was used to obtain p_T spectra in Au+Au and d+Au collisions as well as in the analyses of antiparticle to particle ratios [114, 125].

6.2.1 Analysis Procedure

The measurement of identified particles at intermediate momenta in the PHOBOS experiment is based on the Spectrometer and Time of Flight Counters. Signals from the active elements (silicon) in the Spectrometer are used to construct particle trajectories. Particle momentum and charge are obtained from the trajectory curvature in a $2\ T$ magnetic field and particle identification is provided by the specific energy loss (dE/dx) in the Spectrometer and by the Time of Flight Counters. In this Section the particle reconstruction method is briefly described. More details on the algorithms presented here can be found in [31, 125].

A. Track Finding. In the Spectrometer, tracks are combined from straight track fragments reconstructed in the region outside the magnetic field, i.e. in the first six silicon layers as shown in Fig. 6.11, and from curved track fragments

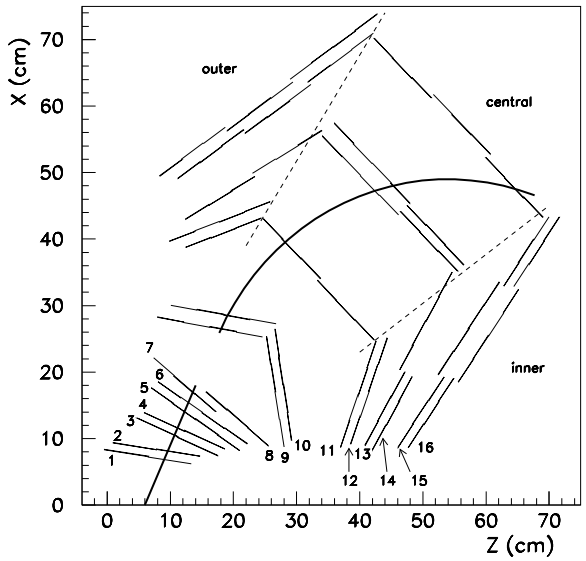

Figure 6.11: *Straight and curved track fragments (solid thick lines) reconstructed by the PHOBOS track finding algorithm. Different silicon layers, labeled by 1,...,16, are depicted by thin solid lines. The central, inner and outer regions of π-shaped layers, labeled by 11,...,16, are separated by dashed lines.*

composed of hits measured by silicon located inside the magnetic field, in layers 9,...,16. The reconstruction is performed independently in both spectrometer arms.

Straight line fragments are obtained by means of a road-following algorithm. The algorithm starts with a construction of "track seeds" which are composed of two hits from first two silicon layers. In this process, the polar, θ, and azimuthal, ϕ, angles are calculated for each hit using its location in the detector and known position of the Au+Au collision vertex. To limit particle trajectories to straight lines, it is required that $\Delta\theta$ and $\Delta\phi$ between constituent hits of a "track seed" are less than maximum cut-off values. In the next step of the algorithm, hits from the third layer are added to a "track seed" only if $\Delta\theta$ and $\Delta\phi$ between the "track seed" hit from the second layer and the hit belonging to the third layer are again less than maximum cut-off values. If there are two hits which fulfill the angular criteria for a given track, then a new, clone track is created so that one hit could be added to the track and the second hit to the clone track. In the procedure one missing hit is allowed and it stops when all six layers, 1-6, are processed. Additionally it is required that out of two tracks which share more than one hit only one track, with the larger straight line χ^2 fit probability, is accepted.

In the tracking algorithm, curved track fragments are searched for independently in the central and the outer wing regions of silicon layers located in the magnetic field, see Fig. 6.11. In the procedure lookup tables are used to map two-hit combinations on consecutive layers into $(1/p, \theta)$ plane, where θ is the polar angle at the primary interaction vertex and p is the total momentum. The lookup tables which relate the particle origin and momentum with positions of the particle hits in the Spectrometer were calculated for 0.5 cm vertex bins in the range $-15\ cm\ <\ Z_{vxt} <\ 10\ cm$ using PHOBOS Monte Carlo simulations for positive and negative pions separately. The curved track fragments are reconstructed using an algorithm which selects clusters of matching hits in $(1/p, \theta)$ space. Curved and straight track pieces are finally matched based on θ, dE/dx values of all hits and on a fit to the full track in the yz-plane. Additionally, to reduce the background contamination, it is required for the particle tracks to have the distance of closest approach (DCA) from the vertex position to the particle trajectory smaller than 3.5 mm. Full tracks are not allowed to share more than two hits. The track selection is based on the χ^2 of a full track fit, described in the next Section. The efficiency of the tracking algorithm was estimated to be about 90%.

B. Momentum Determination. The momentum of a given track is set by a procedure which minimize the χ^2 formula:

$$\chi^2 = \sum_{i=1}^{N} \left(\frac{x_i - f(\alpha)}{\sigma_i} \right)^2, \tag{6.13}$$

where x_i is the measured hit position at layer i and $f(\alpha)$ is a hypothetical, ideal

particle trajectory in a non-uniform magnetic field. The trajectory depending on a set of parameters, α, including particle momentum and vertex location is obtained by the Runge-Kutta algorithm. The residual, $x_i - f(\alpha)$, is calculated as a minimal distance between the hit in layer i and the trajectory. Errors of the residuals, σ_i, are calculated from diagonal elements of the covariance matrix:

$$\sigma_i =< (x_i - \bar{x_i})(x_i - \bar{x_i}) >, \tag{6.14}$$

which takes into account the detector pixelization and multiple scattering. The minimization technique searches for a trajectory of lowest χ^2 which determines the final momentum vector corresponding to the reconstructed track.

C. Particle Identification. The basic idea of the particle identification method in the PHOBOS detector was already described in Section 5.8. A slightly different approach was adopted to obtain identified particle $p_{_T}$ spectra at lower $p_{_T}$ in Au+Au collisions at $\sqrt{s_{_{NN}}} = 62.4\ GeV$ and in d+Au collisions at $\sqrt{s_{_{NN}}} = 200\ GeV$. In the latter method, the momentum range, presented in Fig. 5.11, was split into small bins then for each bin the dE/dx histogram was fitted with Gaussian functions to determine pion, kaon, proton and antiproton yields. In the Spectrometer, good separation of pions and protons up to about 1.2 GeV/c is obtained while kaons and pions are clearly separated up to about 0.6 GeV/c.

6.2.2 Invariant $p_{_T}$ Spectra

The measured raw yields of identified particles, obtained with the reconstruction algorithm described in the previous Section, need to be corrected in order to obtain the primary particle invariant $p_{_T}$ spectra defined by Eq. 6.5. The dominant correction is the geometrical acceptance of the detector and the efficiency of reconstructing particle tracks. The $p_{_T}$ yields are also corrected for the momentum resolution of the track reconstruction algorithm, secondary and ghost particles, DCM as well as for weak decays.

The dominant acceptance and efficiency correction, in the analysis of 62.4 GeV data, was computed using a technique similar to the embedding procedure presented in Section 6.1.2. To obtain the correction for the Spectrometer and TOF detectors, single particles were simulated in a wide range of transverse momentum, up to $p_{_T} \leq 6\ GeV/c$, and reconstructed using the algorithm described in the previous Section. The fraction of reconstructed to simulated particles allows the correction factor to be calculated. The corrections (which are momentum dependent) were computed for all species. In the procedure, when calculating acceptance and efficiency corrections, momenta of simulated particles were smeared to account for the momentum resolution of the reconstruction algorithm. The effect of the momentum smearing is of the order of 2-3%.

The contribution of secondary and ghost particles was studied using the full Monte Carlo simulations of Au+Au collisions, based on the HIJING model and

GEANT. It turned out that the reconstruction cuts are very efficient in rejecting both these types of background particles. The contribution from secondary particles was found to be less than 1% while the contribution from ghost particles increases from 2% (peripheral) to 5% (central) for Au+Au collisions at $\sqrt{s_{NN}} = 62.4\ GeV$.

The correction for feed-down from weak decays is important for proton and antiproton yields which are contaminated from a significant contribution from decays of Λ, $\bar{\Lambda}$ and Σ. However, the yields of these particles in Au+Au collisions at $\sqrt{s_{NN}} = 62.4\ GeV$ have not been published yet. Therefore, in the study of feed-down correction existing data of Au+Au collisions at $\sqrt{s_{NN}} = 130\ GeV$ [126] were extrapolated. Large ratios of $\Lambda/p = 0.89$ and $\bar{\Lambda}/\bar{p} = 0.95$ were measured at $\sqrt{s_{NN}} = 130\ GeV$. The calculation of the feed-down correction was based on the GEANT code which was used to compute the relative reconstruction efficiency of primary protons and protons from weak decays of Λ and Σ particles, assuming that $\Lambda/p = 0.9$ and $\Sigma/p = 0.3$. For the analysis of systematic errors, a reasonable range of the ratios were considered as the data for 62.4 GeV are not yet known. This procedure yielded a momentum dependent feed-down correction for proton spectra which amounts to about 30% at low p_T and decreases to a few percent in the p_T range of a few GeV/c. For the antiproton yield, due to the larger ratio of $\bar{\Lambda}/\bar{p}$, a 20% larger correction was applied.

The feed-down correction for kaon and pion yields were neglected as the contribution was estimated to be less than 1%.

The final identified particle yields corrected for detector effects as well as for feed-down from weak decays in Au+Au collisions at $\sqrt{s_{NN}} = 62.4\ GeV$ [30, 31] are shown in Fig. 6.12.

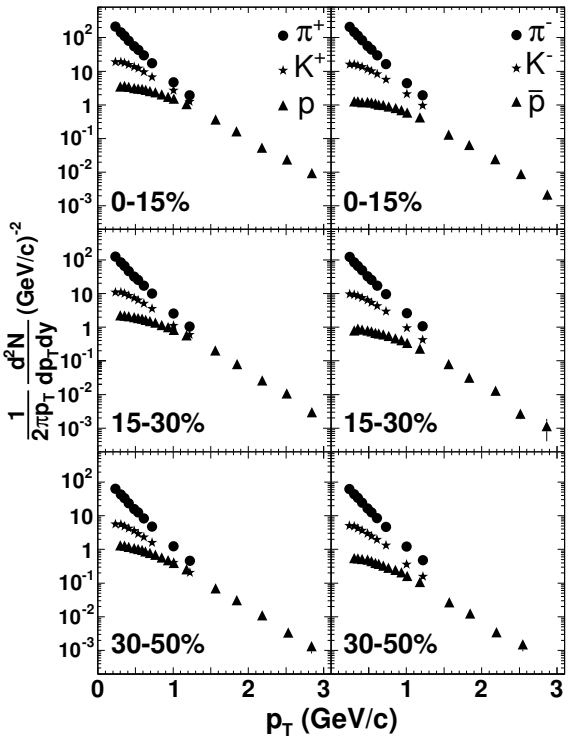

Figure 6.12: *p_T spectra of $\pi^{\pm}$, $K^{\pm}$, p and $\bar{p}$ in Au+Au collisions at $\sqrt{s_{NN}} = 62.4\ GeV$ within three centrality intervals: 0-15%, 15-30% and 30-50% [30, 31].*

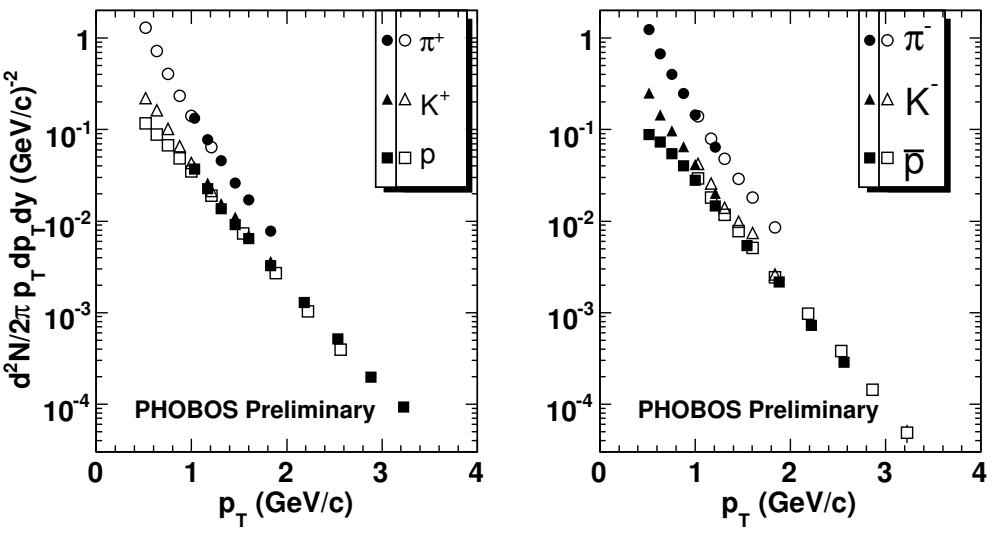

Figure 6.13: *p_T spectra of $\pi^{\pm}$, $K^{\pm}$, p and $\bar{p}$ in minimum bias d+Au collisions at $\sqrt{s_{NN}} = 200$ GeV [30, 124]. The full (open) symbols correspond the data collected with the positive (negative) magnetic field polarity.*

The identified particle spectra of charged pions, kaons, protons and antiprotons in d+Au collisions at $\sqrt{s_{NN}} = 200\ GeV$ [30, 124], corrected for detector effects and background particles, are presented in Fig. 6.13. Similarly to the d+Au yields at very low p_T, the spectra at intermediate p_T represent minimum bias results.

6.3 Charged Particle Yields at High p_T

The p_T spectra of charged particles ($h^+ + h^-$) were measured by PHOBOS over a wide range of transverse momentum for different systems, including Au+Au [7, 127] and d+Au [12]. In the full range of p_T, extending up to about 5 GeV/c, particle momentum and charge can be obtained from the trajectory curvature in the magnetic field, however, the particle identification at high p_T is not possible in the PHOBOS detector.

6.3.1 Analysis Procedure

The reconstruction procedure of charged particle trajectories and particle momenta follows the procedure described in Section 6.2.1. This procedure was used to obtain raw transverse momentum distributions in Au+Au collisions at $\sqrt{s_{NN}} = 200\,GeV$ and $62.4\,GeV$ as well as in d+Au collisions at $\sqrt{s_{NN}} = 200\,GeV$ as a function of centrality.

6.3.2 Invariant p_T Spectra

To obtain the invariant spectra, the raw yield of reconstructed particles are corrected for geometrical acceptance, the efficiency of the tracking algorithm and the distortion due to binning and momentum resolution. The correction procedure [7] is similar for all charged particle spectra obtained in the PHOBOS experiment. Using the MC simulations, the acceptance and efficiency correction factors were obtained by the embedding procedure described in the previous Section. Using this procedure, the correction factors as a function of p_T and multiplicity were extracted. The acceptance and efficiency corrections vary as a function of p_T and vertex position, and are different for the two charge signs in a given field polarity.

MC simulations based on HIJING and GEANT are used to obtain correction factors for the contribution of secondary particles to the charged particle spectra. In the analysis of Au+Au data at 200 GeV the contamination by secondary particles varies with p_T from about 4% at $p_T = 0.3\ GeV/c$ to 2% at $p_T = 2.5\ GeV/c$. The reconstruction of HIJING events also showed a rate of ghost tracks after all quality cuts of less than 4% at $p_T \approx 0.5\ GeV/c$ and less than 2% at $p_T \approx 2.5\ GeV/c$.

Finally, the spectra are corrected for the effects of the finite bin-width and the momentum resolution. The resolution was determined using track embedding and the full reconstruction and fitting procedure. For embedded MC tracks it was found that a momentum resolution is $\Delta p/p = 1 - 9\%$ for the momentum range of 0.3 to 10 GeV/c. The corresponding correction was performed for each centrality interval separately, taking into account the non-Gaussian tails in the p_T-resolution function. At $p_T \approx 4\ GeV/c$, the correction varies from a factor of 0.92 for the most peripheral events to 0.89 for the most central events. The largest contributions to the systematic uncertainty of measured spectra come from the overall tracking efficiency (5–10% uncertainty) and the reduction in overall acceptance due to malfunctioning channels in the silicon detectors (5% uncertainty).

In PHOBOS, the charged particle yields ($h^+ + h^-$), corrected for detector effects, were obtained for Au+Au collisions at $\sqrt{s_{NN}} = 200\ GeV$ [7] and 62.4 GeV [127] and in d+Au collisions at $\sqrt{s_{NN}} = 200\ GeV$ [12]. The charged particle yields in Au+Au collisions at $\sqrt{s_{NN}} = 200\ GeV$ were obtained using the Run-02 data sample. To optimize the precision of the vertex and track finding, only events with a reconstructed primary vertex position between $-10\ cm < Z_{vtx} < 10\ cm$ along the beam axis were selected. The selected Au+Au sample contained 5.84 million events in six centrality intervals, see Table 5.2. For that analysis, particles within a rapidity interval of $0.2 < y_\pi < 1.4$ (assuming the pion mass for calculating y_π) were selected. The final p_T spectra in Au+Au collisions

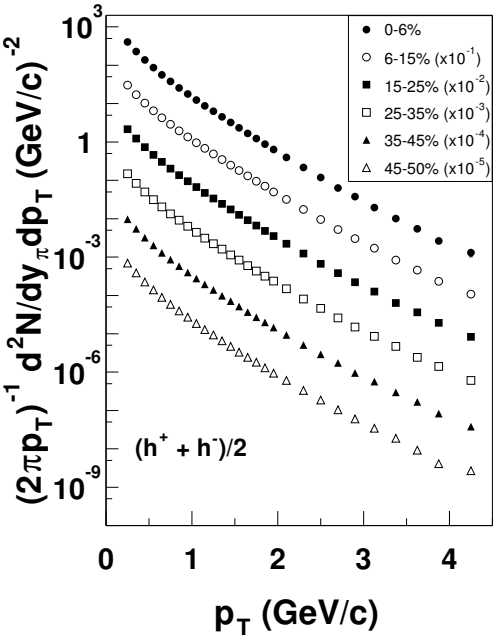

Figure 6.14: *Invariant yields of charged hadrons, $\frac{h^+ + h^-}{2}$, as a function of p_T for 6 centrality intervals in Au+Au collisions at $\sqrt{s_{NN}} = 200\ GeV$ [7]. For clarity, yields for consecutive centrality intervals are scaled by factors of 10.*

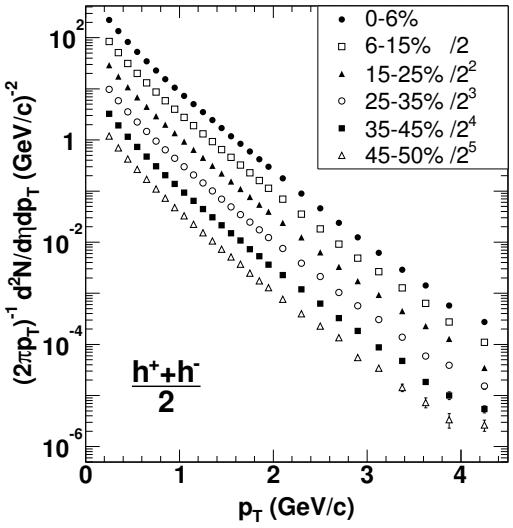

Figure 6.15: *Invariant yields of charged hadrons in Au+Au collisions at $\sqrt{s_{NN}} = 62.4\ GeV$ [127] as a function of p_T for 6 centrality intervals. For clarity, data for consecutive intervals are scaled by factors of 2.*

at $\sqrt{s_{NN}} = 200\ GeV$ are shown in Fig. 6.14.

To obtain invariant yields of charged hadrons in Au+Au collisions at $\sqrt{s_{NN}} = 62.4\ GeV$ events from the Run-04 sample were selected. The track reconstruction procedure used in this analysis follows the procedure described in Section 6.2.1. The correction procedures and the associated systematic uncertainties are similar to those obtained in the analysis of Au+Au data at energy of $\sqrt{s_{NN}} = 200\ GeV$. In Fig. 6.15, we present the invariant yields of charged hadrons in Au+Au collisions at $\sqrt{s_{NN}} = 62.4\ GeV$ as a function of transverse momentum, obtained by averaging the yields of positive and negative hadrons.

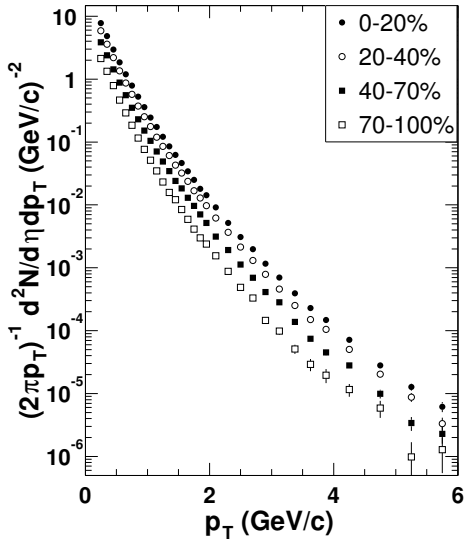

Figure 6.16: *Invariant yields of charged hadrons, $\frac{h^+ + h^-}{2}$, as a function of p_T for four centrality intervals in d+Au collisions at $\sqrt{s_{NN}} = 200\ GeV$ [12].*

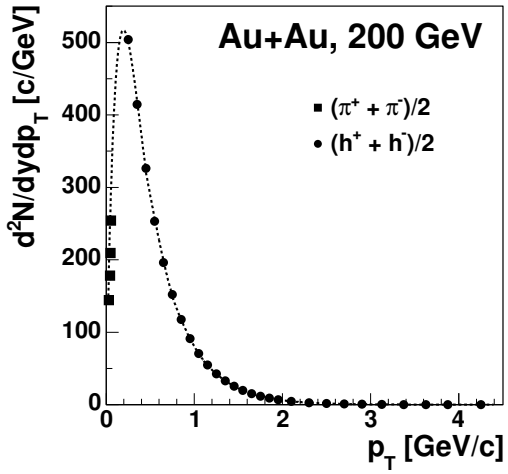

Figure 6.17: *Particle density for charged pions and hadrons as a function of p_T in the 15% most central Au+Au collisions at energy of $\sqrt{s_{NN}} = 200\ GeV$. The data for charged pions at very low p_T (squares) [27] and at intermediate and high p_T (full circles) [7] are shown. A line is drawn to interpolate between points.*

Fig. 6.16 shows the final p_T spectra in d+Au collisions at $\sqrt{s_{NN}} = 200\ GeV$. The d+Au data at energy of $\sqrt{s_{NN}} = 200\ GeV$ were collected during Run-03. The primary trigger and event selection used were described in Section 5.3. The analyzed sample was limited to the range of vertex positions from $-15\ cm$ to $+10\ cm$. As the accuracy of vertex determination in d+Au collisions is worse than in Au+Au collisions the vertex location was not used during the d+Au tracking. The contamination by secondary and feed-down particles was found to be small, due to the proximity of the tracking detectors to the collision vertex and the requirement for the reconstructed track to point back to the beam orbit to within 0.4 cm. The centrality cuts used in the analysis of d+Au data are based on the signal from charged particles measured in the Ring Multiplicity Detectors, E_{ring}, as described in Section 5.5.

In summary, in this Chapter we have shown that the PHOBOS detector has an excellent and unique capability to measure charged particles in a wide range of the transverse momentum. The full p_T reach, from 0.03 up to 4.5 GeV/c, is presented in Fig. 6.17 where particle density, $d^2N/dydp_T$, in the 15% most central Au+Au collisions at $\sqrt{s_{NN}} = 200\ GeV$ is shown as a function of the transverse momentum. The results for charged pions, depicted by squares in Fig. 6.17, represent yields measured in the lowest p_T range at RHIC, accessible only in the PHOBOS experiment.

Chapter 7

Transverse Momentum Spectra from Nuclear Collisions at RHIC

This Chapter is devoted to the physical results obtained from the study of the charged particle transverse momentum distributions measured in the full p_T range of the PHOBOS experiment. As already pointed out in Section 2.4, the study of particle production at very low transverse momenta ($p_T < 0.2\ GeV/c$) is particularly interesting as the low-p_T region is associated with long-distance scales accessible only in heavy-ion collisions. Exploring this exciting physics at very low-p_T is unique to the PHOBOS experiment. It is also the main subject of this paper. Therefore, it is important to compare the measurements at very low, intermediate and at high p_T to see if the data constitute a consistent picture of the dense medium produced in the relativistic heavy-ion collisions at RHIC.

7.1 Transverse Expansion of the System Produced in Au+Au Collisions

To verify if an enhanced production of particles at very low p_T is measured in nuclear collisions, one can compare the p_T spectra at very low and intermediate transverse momenta. Fig. 7.1 shows the transverse momentum distributions of $(\pi^+ + \pi^-)$, $(K^+ + K^-)$ and $(p + \overline{p})$ in the 15% most central Au+Au collisions at energy of $\sqrt{s_{NN}} = 200\ GeV$, measured by STAR [67], PHENIX [66] and BRAHMS [65] experiments at intermediate p_T together with PHOBOS data at very low p_T [27], as presented in Section 6.1.2. The $(p + \overline{p})$ spectra obtained by the BRAHMS and STAR experiments are not shown in Fig. 7.1 as they were not corrected for feed-down from weak decays. The PHOBOS results are compared with extrapolations to low p_T from fits to the transverse momentum distributions (solid lines) measured at intermediate p_T by the PHENIX experiment with the functions:

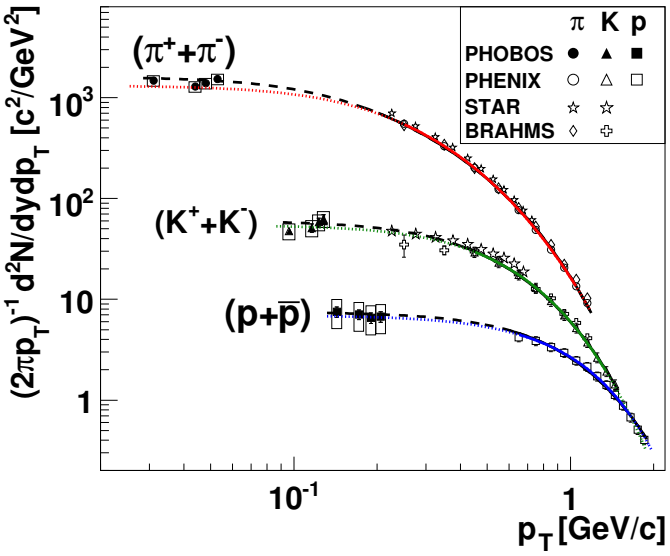

Figure 7.1: *p_T spectra in the 15% most central Au+Au collisions at $\sqrt{s_{NN}} = 200\ GeV$. Closed symbols represent PHOBOS data at very low-p_T [27]. Intermediate p_T measurements from BRAHMS [65], PHENIX [66] and STAR [67] are depicted by open symbols. The fits to PHENIX measurements (solid curves) are extrapolated to very low p_T (dashed and dotted curves) for comparison with the PHOBOS data. See text for details.*

$$f = \frac{A}{e^{m_T/T_{fit}} + \epsilon}. \tag{7.1}$$

Here, $\epsilon = -1(+1)$ for mesons (baryons) and this function reasonably describes the intermediate p_T measurements ($m_T \leq 1\ GeV/c^2$) from PHENIX as well as the STAR and BRAHMS data. The parameters of the fit are shown in Table 7.1. Extrapolations of the functions to low p_T, depicted in Fig. 7.1 by dashed lines, agree well with the measured low-p_T yields. Therefore, we see no enhancement in

Table 7.1: *Parameters of functions, defined by Eq. 7.1, fitted to PHENIX data shown in Fig. 7.1. χ^2 of each fit divided by the number degrees of freedom, ndof, is also quoted. The mean transverse momentum and mean transverse mass of $(\pi^+ + \pi^-)$, $(K^+ + K^-)$ and $(p + \overline{p})$ were obtained using the fitted functions.*

	A $(c/GeV)^2$	T_{fit} (GeV/c^2)	$\chi^2/ndof$	$< p_T >$ (GeV/c)	$< m_T >$ (GeV/c^2)
$(\pi^+ + \pi^-)$	1348 ± 103	0.229 ± 0.005	0.17	0.426	0.460
$(K^+ + K^-)$	264 ± 39	0.293 ± 0.010	0.02	0.682	0.877
$(p + \overline{p})$	89 ± 13	0.392 ± 0.015	0.33	1.039	1.456

the production of particles with very low transverse momenta, that would indicate the presence of unusual long-wavelength phenomena. One can see that the slope parameter, T_{fit}, increases approximately linearly with the particle mass. According to Eq. 2.4 such dependence is consistent with the collective transverse expansion of the medium created in the relativistic heavy-ion collisions. To study the possible expansion in more detail, it is interesting to see how well the blast wave model [33], assuming that particles are produced from an expanding thermal source, describes the p_T spectra at very low transverse momentum. The source function of the model, was fitted to the PHENIX data and then extrapolated into the low-p_T region. One can see that the p_T spectra are quite well described by blast wave functions (BWF) too. Fitting simultaneously pion, kaon, proton and antiproton p_T spectra with BWF allows the determination of the transverse expansion velocity, β_T, and the freeze-out temperature, T_{fo}. The results are $\beta_T/c = 0.8$ and $T_{fo} = 106\ MeV$. The extrapolations of BWF to the low-p_T region are depicted in Fig. 7.1 by dotted lines. The transverse momentum distributions of identified charged particles at very low p_T in Au+Au collisions were also obtained at the energy of $\sqrt{s_{NN}} = 62.4\ GeV$ [30, 31]. The reconstruction algorithm, described in Section 6.1.2, was used to obtain the p_T spectra within three centrality intervals: 0-15%, 15-30% and 30-50%. Low-p_T yields of $(\pi^+ + \pi^-)$, $(K^+ + K^-)$ and $(p + \bar{p})$ near mid-rapidity in Au+Au collisions at $\sqrt{s_{NN}} = 62.4\ GeV$ are corrected for detector effects (acceptance, efficiency) and background particles including feed-down from weak decays and secondary particles produced in the beam pipe and detector material, see Fig. 7.2.

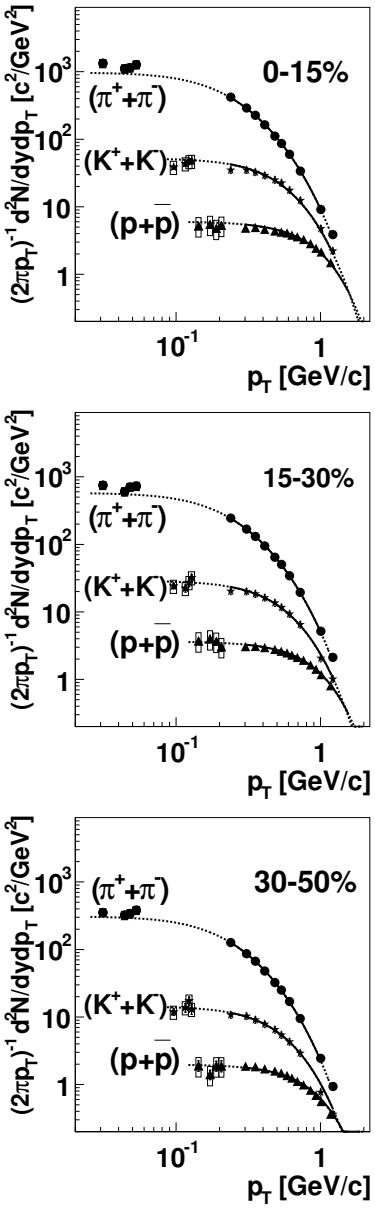

Figure 7.2: *PHOBOS $(\pi^+ + \pi^-)$, $(K^+ + K^-)$ and $(p + \bar{p})$ yields at very low p_T in Au+Au collisions at $\sqrt{s_{NN}} = 62.4\ GeV$ in centrality bins: 0-15%, 15-30% and 30-50%. Blast wave fits to intermediate p_T data (solid lines) are extrapolated to low p_T (dotted lines).*

The transverse momentum distributions at very low p_T are compared to charged particle spectra in Au+Au collisions at $\sqrt{s_{NN}} = 62.4\ GeV$ measured in the intermediate p_T range within the same centrality bins. The intermediate p_T spectra were presented in Section 6.2 in Fig. 6.12. The yields of $(K^+ + K^-)$ and $(p + \bar{p})$ at very low-p_T are quite well described by BWF fitted to the spectra at intermediate transverse momenta. The blast-wave parameters are very similar: $\beta_T/c = 0.78,\ 0.76,\ 0.72$ and $T_{fo} = 103,\ 102,\ 101\ MeV$ in the different centrality bins: 0-15%, 15-30% and 30-50%, respectively. The small disagreement between the measured yield of pions and BWF at very low p_T could be assigned to resonances, which are not included in this model. Therefore, the pion spectra at very low p_T, measured by the PHOBOS experiment, provide an excellent handle on the resonance contribution. The resonance contribution strongly depends on the pion momentum, being the largest at small p_T. Resonances are included in some hydrodynamical models of nuclear collisions presented later in this Chapter.

Summarizing, the data indicate that in Au+Au collisions at both energies, $\sqrt{s_{NN}} = 200\ GeV$ and $62.4\ GeV$, no significant enhancement of particle production is observed at very low p_T. These results also provide indirect evidence that the medium produced in heavy-ion collisions at RHIC is a strongly coupled system. As already discussed in Section 2.4 formation of a system composed of weakly interacting constituents may lead to an enhanced production of particles at very low transverse momenta. The observation that there is no such excess could be a manifestation of high pressure gradients and a significant level of interaction present in the medium which accelerate low-p_T particles and produce large transverse flow.

It should also be noted that the results at very low-p_T are useful to constrain particle yields at $p_T \approx 0$. Different parameterizations have been used to extrapolate the measurements at intermediate p_T to $p_T = 0$ in order to determine the mean p_T and total (integrated) particle yields [65–67]. Measurements at very low p_T provide constraints on the choice of the functional form which best fits the p_T spectra. In Table 7.1 mean values of the transverse momentum and the transverse mass obtained from the fits which well describe the measured low-p_T yields, are quoted.

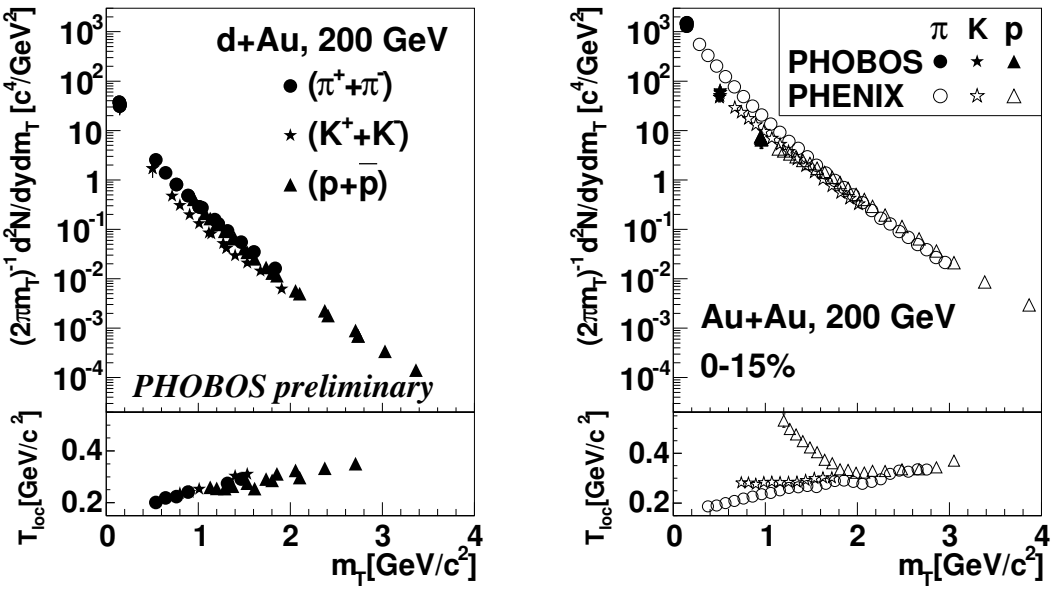

Figure 7.3: *m_T spectra of $(\pi^+ + \pi^-)$, $(K^+ + K^-)$ and $(p + \bar{p})$ at very low and intermediate p_T measured in d+Au [30] (left) and central Au+Au [27, 66] collisions (right) at $\sqrt{s_{NN}} = 200$ GeV. The inverse local slope parameters of m_T spectra are shown in the lower panels of each figure.*

7.2 m_T-Scaling in Au+Au and d+Au Collisions

Motivated by the idea of the Color Glass Condensate, it was predicted that the m_T spectra for different particle species should follow a universal function of m_T [71, 72]. One implication of the m_T scaling described in [72] is that the spectral shapes should be independent of particle mass in a wide range of m_T. An approximate m_T-scaling can be observed in m_T yields of $(\pi^+ + \pi^-)$, $(K^+ + K^-)$ and $(p + \bar{p})$ in d+Au collisions, shown in Fig. 7.3 (left panel). One can see that in d+Au collisions $(\pi^+ + \pi^-)$ and $(p + \bar{p})$ m_T spectra are similar while the $(K^+ + K^-)$ spectrum is systematically lower (by a factor of about 2) due to associated strangeness production.

In order to compare the shapes of the m_T spectra, inverse local slope parameters, T_{loc}, were calculated by fitting locally exponential functions to each spectrum (see lower panels of Fig. 7.3). T_{loc} are obtained from the exponential fits done with a sliding window enclosing 5 consecutive m_T points. The first inverse slope is calculated from the fit to the low-p_T average yield and the first four points at intermediate transverse momenta ($p_T > 0.2$ GeV/c). We can see that for d+Au collisions local slopes are similar for all particle species both at low and intermediate p_T. In contrast, the m_T spectra for the 15% most central Au+Au collisions, shown in Fig. 7.3 (right panel), are similar at higher transverse masses ($m_T > 1.7$ GeV/c^2) while at low m_T a flattening of $(K^+ + K^-)$ and $(p + \bar{p})$ spectra

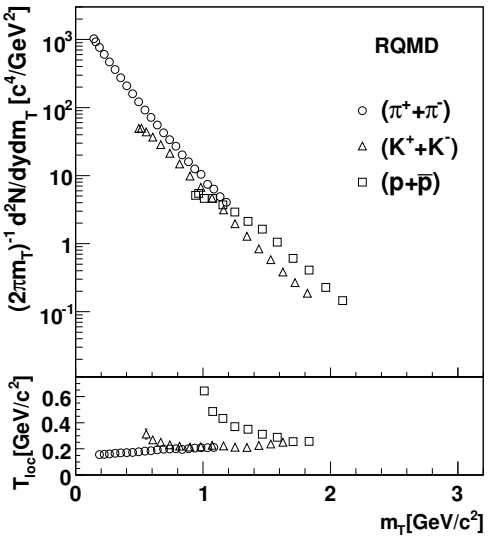

Figure 7.4: *Particle yields in the 15% most central Au+Au collisions at* $\sqrt{s_{NN}} = 200$ *GeV obtained from the RQMD model as a function of* m_T*. The lower panel shows the* m_T *dependence of the local inverse slopes.*

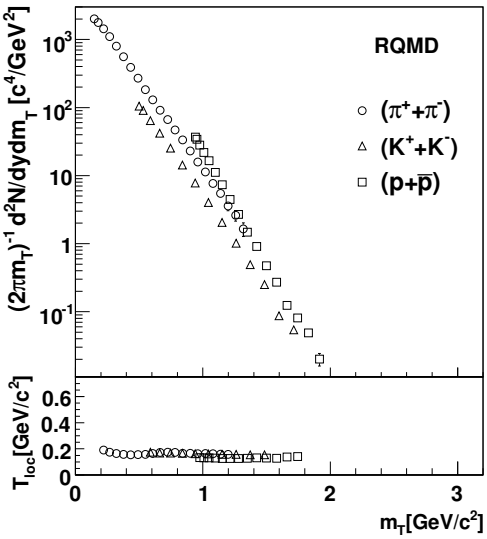

Figure 7.5: *Particle yields in Au+Au collisions obtained from the RQMD model without final state rescatterings as a function of* m_T*. The lower panel shows the* m_T *dependence of the local inverse slopes.*

is observed. This flattening of the $(p + \bar{p})$ spectrum is significantly stronger than the one observed for the spectra of charged kaons. One can also see that the m_T dependence of the local slopes of the $(\pi^+ + \pi^-)$ m_T spectrum for Au+Au collision is consistent with that found for the local slopes of $(\pi^+ + \pi^-)$, $(K^+ + K^-)$ and $(p + \bar{p})$ spectra in d+Au collisions. This observation is consistent with the mass dependent flattening of the spectra at low m_T, expected in the presence of a transverse expansion of the system, and contradicts the suggested m_T scaling in Au+Au collisions [72].

The flattening of the $(p+\bar{p})$ spectrum, clearly observed in the right lower panel of Fig. 7.3, can be explained by transverse flow incorporated in hydrodynamical models, see the next Section, or by final state hadron rescatterings, included e.g. in the RQMD model. As an example, predictions for local slope parameters of Au+Au m_T spectra from the RQMD model are shown in Fig. 7.4. In RQMD, the increase in T_{loc} (the violation of m_T scaling) near the threshold of the $p + \overline{p}$ spectrum ($m_T \approx 0.94\ GeV/c^2$) is caused by final state resonance interactions as switching them off explicitly leads to a perfect m_T scaling down to the lowest p_T, as shown in Fig. 7.5.

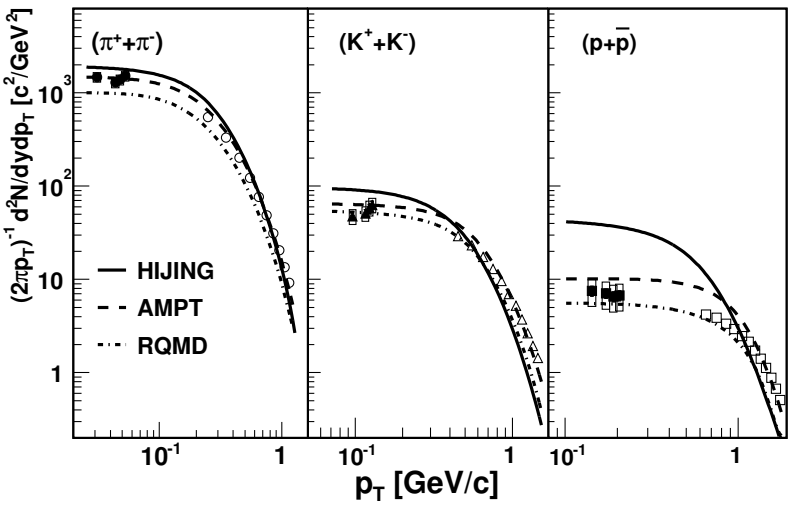

Figure 7.6: *Invariant yields of* $(\pi^+ + \pi^-)$, $(K^+ + K^-)$ *and* $(p+\overline{p})$ *in the 15% most central Au+Au collisions at* $\sqrt{s_{NN}} = 200$ *GeV compared to HIJING (solid line), AMPT (dashed line) and RQMD (dashed-dotted line) model predictions., The closed/open symbols represent the PHOBOS [27]/PHENIX [66] data at very low/intermediate* p_T.

7.3 Low-p_T Data as Unique Model Constraints

The identified charged hadron spectra at very low transverse momentum provide important constraints for models describing soft particle production in relativistic nuclear collisions. The data at very low p_T are compared to various model predictions including Monte Carlo event generators [73, 110, 118], hydrothermal [68, 70, 128, 129] and optical [60] models. Recently, the data were also used to confront predictions of a model which describes the nuclear collisions in the framework of percolation of color sources [130].

Fig. 7.6 shows HIJING, AMPT and RQMD predictions for transverse momentum distributions of identified particles produced near mid-rapidity at very low and intermediate p_T in the 15% most central Au+Au collisions at $\sqrt{s_{NN}} = 200\,GeV$ compared with the PHOBOS and PHENIX experimental results. We can see that HIJING overestimates $(\pi^+ + \pi^-)$, $(K^+ + K^-)$ and $(p+\overline{p})$ yields at low p_T by factors 1.3, 1.6 and 5.5, respectively. The large discrepancy could be a consequence of an absence of a mechanism which leads to a collective transverse expansion of the system. In contrast, in RQMD [73] and AMPT [118] final state rescatterings of hadrons (which generates a flattening of m_T spectra) is included. Therefore, the RQMD model rather correctly reproduces the yields of $(K^+ + K^-)$ and $(p+\overline{p})$ but underestimates the low-p_T yield of charged pions. AMPT reasonably describes $(\pi^+ + \pi^-)$ and $(K^+ + K^-)$ spectra, however, it overestimates the $(p + \overline{p})$ yield at very low p_T by a factor 1.4.

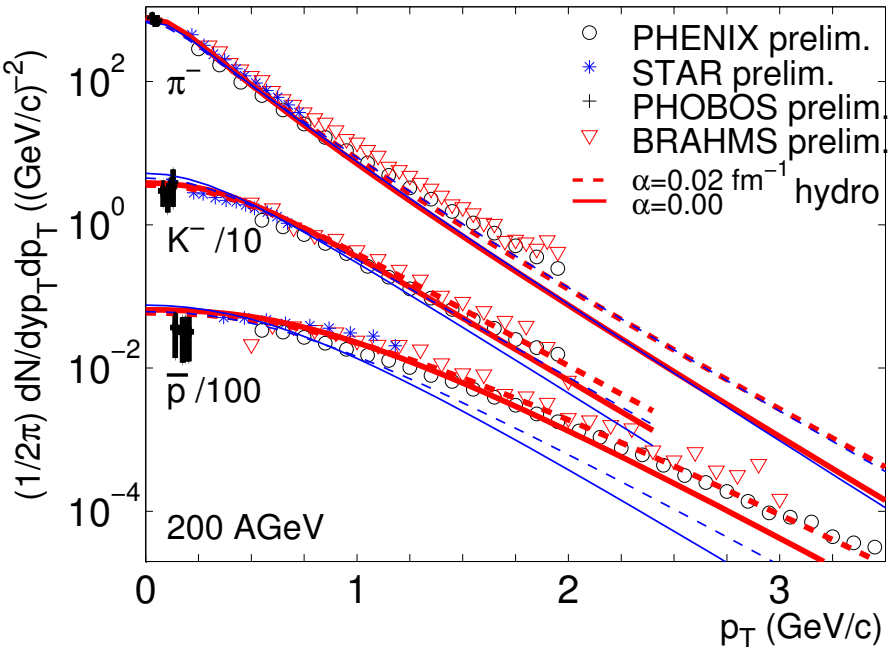

Figure 7.7: π^-, K^- *and* $\bar{p}$ *spectra for central Au+Au collisions at* $\sqrt{s_{NN}} =$ 200 *GeV (kaon and antiproton spectra are scaled by factors of 1/10 and 1/100, respectively). The thick lines represent the results for* $T_{\rm dec} = 100$ *MeV, the thin lines for* 165 *MeV, either with (dashed lines) or without (solid lines) an initial transverse flow (see Ref. [70] for more details).*

An interesting scenario of the dynamical evolution of the medium produced in relativistic heavy collisions at RHIC energies is proposed in hydrodynamical models. The initial system dynamics in these models [69, 70] is based on solutions of the fluid-dynamical equations of motion and on equations of state commonly inspired by lattice QCD calculations. The hydrodynamical evolution is terminated at freeze-out when fluid elements hadronize, traditionally, according to the Cooper-Frye procedure [131]. The hydrodynamical expansion is driven by transverse pressure gradients which accelerate fluid elements, building up collective transverse flow which eventually leads to the $m_{_T}$ flattening of single particle spectra. Fig. 7.7 (from Ref. [70]) shows predictions of hydrodynamical calculations for π^-, K^- and $\overline{p}$ spectra compared to the preliminary experimental data from all RHIC experiments including PHOBOS low-$p_{_T}$ data. The presented results indicate that hydrodynamical models are able to describe the bulk of the particle production within the $p_{_T}$ range from 0.03 to 1.5 GeV/c. According to this model the thermalized quark-gluon plasma in central Au+Au collisions at 200 GeV is formed within time $\tau_0 = 0.6$ fm/c and lives for about $5-7$ fm/c before it hadronizes. A better agreement of the model predictions at higher $p_{_T}$ was

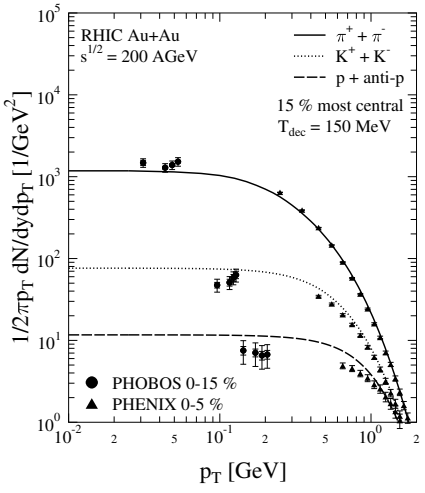

Figure 7.8: *The hydrodynamical model [129] results (lines) compared to the transverse momentum distributions of $(\pi^+ + \pi^-)$, $(K^+ + K^-)$ and $(p + \bar{p})$ in central Au+Au collisions at $\sqrt{s_{NN}} = 200\ GeV$, measured by PHOBOS [27] and PHENIX [66].*

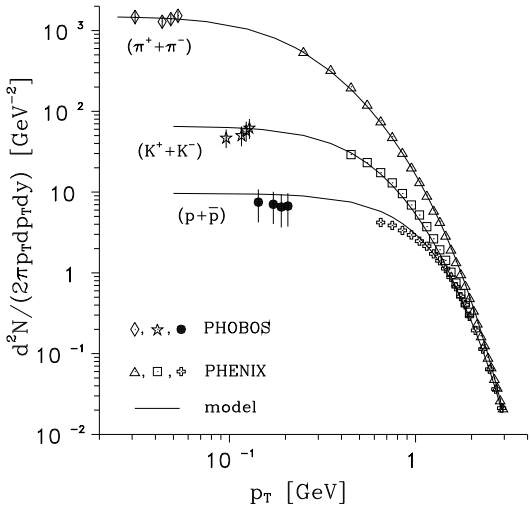

Figure 7.9: *The Cracow Single Freeze-Out Model predictions (lines) for $(\pi^+ + \pi^-)$, $(K^+ + K^-)$ and $(p + \bar{p})$ p_T spectra [128]. The data points represent experimental yields measured by PHOBOS [27] and PHENIX [66] in the 15% most central Au+Au collisions at $\sqrt{s_{NN}} = 200\ GeV$.*

achieved asserting an initial transverse boost in the dynamical evolution which could be produced due to pre-thermal interactions. A detailed description of the model can be found in [70]. In a different version of the hydrodynamical model [129], without initial transverse flow, the PHOBOS spectra are rather well reproduced, as depicted in Fig. 7.8 (from Ref. [129]). However, some differences can be observed. The spectra of kaons and protons obtained in this model are above the data while the predicted pion yield at very low p_T is smaller than experimentally observed. This figure clearly shows, that the invariant p_T spectra obtained in the hydrodynamical model are smooth and flat at very low p_T. The PHOBOS low-p_T spectra were also compared with the predictions of the Cracow Single Freeze-Out Model which turned out to be quite successful in describing particle spectra at RHIC energies [68, 132, 133]. In this model particles are generated from the freeze-out hyper-surface with initial particle phase-space densities provided by statistical distribution functions. The complete spectrum of existing resonances was included in the description. Produced resonances subsequently cascade contributing to particle spectra. One can see in Fig. 7.9 (from Ref. [128]) that the predictions for the pion, kaon and proton and antiproton spectra, obtained in this model, look quite consistent with the experimental data at very low p_T in the 15% most central Au+Au collisions at $\sqrt{s_{NN}} = 200\ GeV$.

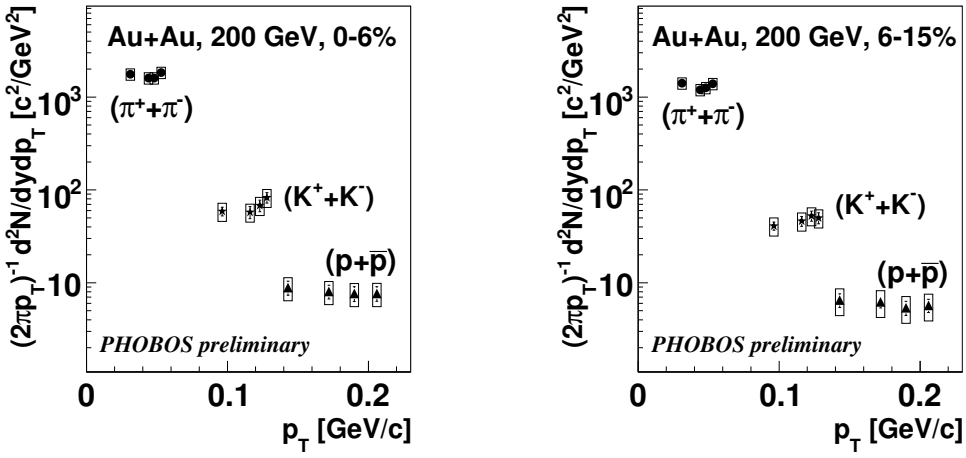

Figure 7.10: *$(\pi^+ + \pi^-)$, $(K^+ + K^-)$ and $(p + \bar{p})$ yields at very low p_T in 0-6% and 6-15% central Au+Au collisions at $\sqrt{s_{NN}} = 200\ GeV$.*

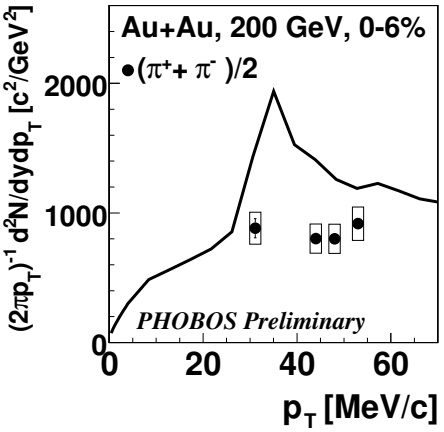

Figure 7.11: *Optical model predictions [60, 134] for the pion spectrum at very low p_T compared to PHOBOS data (see text for details).*

In contrast to the hydrodynamical or Monte Carlo models, a recent optical model [60] predicts a strong p_T dependence of pion spectra at very low transverse momenta. This model, asserting chiral symmetry restoration in an opaque pionic source, turned out to be quite successful in describing the HBT radii measured in relativistic gold ion collisions at $\sqrt{s_{NN}} = 200\ GeV$ [135–137]. The assumption that chiral symmetry is restored has important consequences on pion spectra at very low p_T. The measured spectra of $(\pi^+ + \pi^-)$, $(K^+ + K^-)$ and $(p + \bar{p})$ at very low transverse momentum in the 15% most central Au+Au collisions at $\sqrt{s_{NN}} = 200\ GeV$ were split into two finer centrality bins, in order to confront the extrapolations from the model, which were available only for more central collisions. The method, described in Section 6.1.2, was used to obtain identified charged particle transverse momentum distributions within the centrality intervals 0-6% and 6-15%. Fig. 7.10 shows the final p_T yields, corrected for detector effects and background particles. In Fig. 7.11 the model prediction for the neg-

ative pion spectrum at mid-rapidity for the 5% most central Au+Au collisions at $\sqrt{s_{_{NN}}} = 200\ GeV$ is shown. It was found, by PHOBOS, that the original prediction presented in Ref. [60] was erroneous and had to be corrected in a journal erratum. The solid curve depicts the recently modified and corrected model calculations. In Fig. 7.11, the pion yield measured in the 6% most central Au+Au collisions is compared to the optical model predictions for the spectrum of negative pions at mid-rapidity. The large excess in pion production at $p_{_T} \approx 35\ MeV/c$ is not confirmed experimentally.

7.4 Antiparticle to Particle Ratios

The final transverse momentum distributions are frozen when all processes, including elastic scatterings, stop. Usually, the kinetic freeze-out is expected to occur later and at lower temperature than the chemical freeze-out. The ratios of identified particles at intermediate $p_{_T}$ allow one to study the properties of the system, like the level of equilibrium attained in the primordial state, before kinetic freeze-out. The net-proton density (or proton to antiproton ratio) at mid-rapidity in nucleus-nucleus collisions at AGS and SPS energies is much larger than in nucleon-nucleon interactions as a consequence of large baryon stopping present at these energies. Therefore, as particle abundances are set in at chemical freeze-out, they provide an excellent probe for the level of equilibrium attained in an environment of large baryon number density. The baryon stopping effect is expected to be smaller at higher energies. Nucleus-nucleus collisions at the highest RHIC energy are approaching the net-baryon free regime for which experimental results can be compared to the QCD lattice calculations. This allows models of baryon production and baryon number transport in nuclear collisions at energies ranging from AGS to RHIC to be validated.

The PHOBOS experiment obtained ratios of antiparticles to particles near mid-rapidity for primary charged pions, kaons, and protons produced in the 12% most central Au+Au collisions at energy of $\sqrt{s_{_{NN}}} = 130\ GeV$ [125] and $\sqrt{s_{_{NN}}} = 200\ GeV$ [114]. A Glauber calculation was used to relate the fraction of the cross section to the number of participating nucleons, as described in Section 5.5. The average number of participating nucleons in the 12% most central Au+Au collision was calculated to be 312 ± 10 (syst.) and 317 ± 10 (syst.) at energy of $\sqrt{s_{_{NN}}} = 130$ and $200\ GeV$, respectively. To calculate the primary antiparticle to particle ratios, the number of reconstructed particles was corrected for particles produced in secondary interactions, loss of particles due to absorption in detector material, feed-down particles from weak decays, and possible contamination by misidentified particles. The final antiparticle to particle ratios in the 12% most central Au+Au collisions at $\sqrt{s_{_{NN}}} = 130\ GeV$ and $\sqrt{s_{_{NN}}} = 200\ GeV$ are

Table 7.2: *Ratios of antiparticles to particles produced in the 12% most central Au+Au collisions near mid-rapidity at* $\sqrt{s_{NN}} = 130\ GeV$ *and* $\sqrt{s_{NN}} = 200\ GeV$. *The statistical and systematic (in parenthesis) errors are shown.*

	Au+Au $\sqrt{s_{NN}} = 130\ GeV$	Au+Au $\sqrt{s_{NN}} = 200\ GeV$
$\langle\pi^-\rangle/\langle\pi^+\rangle$	1.00 ± 0.01 (0.02)	1.025 ± 0.006 (0.018)
$\langle K^-\rangle/\langle K^+\rangle$	0.91 ± 0.07 (0.06)	0.95 ± 0.03 (0.03)
$\langle\bar{p}\rangle/\langle p\rangle$	0.60 ± 0.04 (0.06)	0.73 ± 0.02 (0.03)

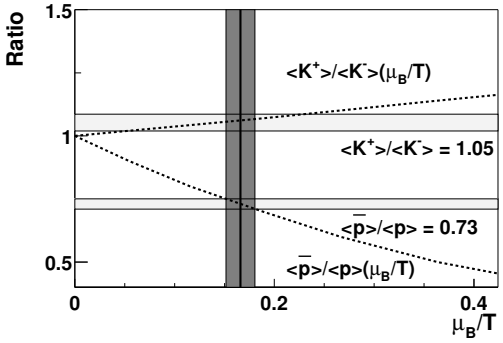

Figure 7.12: *Thermal model [139] calculations (dotted lines) of* K^+/K^- *and* $\overline{p}/p$ *ratios of central Au+Au collisions at* $\sqrt{s_{NN}} = 200\ GeV$. *A good prediction for the experimental ratios (horizontal shaded bars) is achieved at* $\mu_B/T = 0.17 \pm 0.01$ *(vertical shaded bar). See text for more details.*

presented in Table 7.2.

The particle ratios were shown to be consistent with statistical models of particle production [138], assuming chemical equilibrium. These models gave a very good description of the particle ratios at an energy of 130 GeV (200 GeV) with a hadronization temperature of $T_{chem} = 175\ MeV(165\ MeV)$ and a baryochemical potential $\mu_B = 45 \pm 5\ MeV$ $(27 \pm 2\ MeV)$, as shown in Fig. 7.12. The baryochemical potential at 200 GeV is a factor of two smaller than the 130 GeV value and an order of magnitude less than the baryochemical potential at SPS energies. Interestingly, thermal model calculations suggest that, at RHIC energies, particle composition is set at a temperature comparable to the phase transition temperature, T_c.

The results on antiparticle to particle ratios have also been obtained for the 15% most central Au+Au collisions at $\sqrt{s_{NN}} = 62.4\ GeV$ [30]. The results of 0.84 ± 0.02 (stat.) ± 0.08 (syst.) for K^-/K^+ and 0.37 ± 0.01 (stat.) ± 0.06 (syst.) for $\bar{p}/p$ fit smoothly into the energy evolution of the antiparticle to particle ratios from the AGS up to the highest RHIC energy. The energy dependence of

$\langle K^- \rangle / \langle K^+ \rangle$ and $\langle \bar{p} \rangle / \langle p \rangle$ ratios in central heavy-ion collisions near mid-rapidity from AGS to the highest RHIC energy is shown in Fig 7.13. In the most central Au+Au collisions, near mid-rapidity, at $\sqrt{s_{_{NN}}} = 200\ GeV$ the antiproton to proton ratio is $\overline{p}/p = 0.73$ while at SPS the corresponding ratio in fixed-target Pb+Pb collisions at $\sqrt{s_{_{NN}}} = 17.3\ GeV$ is 0.1 [82, 84]. One can see that, a significant baryon stopping is still observed at 62.4 GeV while at the highest RHIC energy the system is approaching the net-baryon free environment.

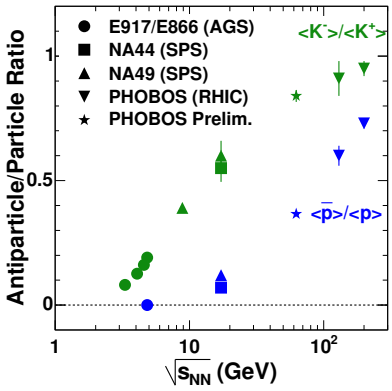

Figure 7.13: *Energy dependence of K^-/K^+ and $\overline{p}/p$ ratios near mid-rapidity for central Au+Au collisions at RHIC [114, 125] and AGS [80, 81, 140] energies and central Pb+Pb collisions at SPS energy [82, 84].*

Summarizing, the particle ratios in central Au+Au collisions at the highest RHIC energy indicate that a high level of equilibrium is attained in the medium at the chemical freeze-out. At this stage of the system evolution the temperature is close to T_c. The critical temperature is obtained using the robust QCD lattice calculations in a net-baryon free environment, similar to the environment formed in the nuclear collisions at RHIC.

7.5 Suppression of High-$p_{_T}$ Particle Yields

The single particle spectra ($h^+ + h^-$) at high transverse momentum provide important information on properties of the medium produced in nuclear collisions as well as provide valuable crosschecks to models describing nucleus-nucleus collisions. The "tail" of transverse momentum distributions at high $p_{_T}$ originates from short-range hard partonic scatterings which occur early in nuclear collisions. Therefore, these hard scattered partons propagate through the dense medium before they fragment into jets of particles with leading high-$p_{_T}$ hadrons measured in the detector. It turns out that comparison of $A+A$, $p+A$ and $p+p$ spectra at high $p_{_T}$ allows for a systematic study of different kinds of effects present in both the initial and final state of nuclear collisions. One of the most remarkable results from RHIC, discussed in this Section, is the observation that the production of high-$p_{_T}$ particles in central Au+Au collisions at $\sqrt{s_{_{NN}}} = 130$ and 200 GeV is strongly suppressed in comparison to the expected particle production based on

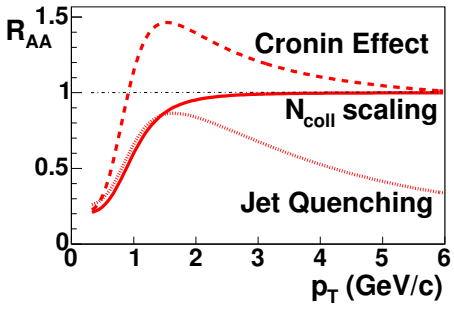

Figure 7.14: *A schematic view of nuclear modification factors showing the Cronin effect ($R_{AA} > 1$, dashed line), N_{coll} scaling ($R_{AA} \approx 1$, solid line) and jet quenching effect ($R_{AA} << 1$, dotted line) at high transverse momentum, $p_T > 2$ GeV/c. See text for details.*

the extrapolation of $p + \bar{p}$ data.

The production of particles at high p_T in nucleus-nucleus collisions is commonly compared to the particle production in nucleon-nucleon interactions. To this end, the nuclear modification factor, R_{AA}, is defined as

$$R_{AA} = \frac{1}{\langle N_{coll} \rangle} \frac{d^2N_{AA}/dp_T d\eta}{d^2N_{NN}/dp_T d\eta}, \tag{7.2}$$

where the spectra in nuclear collisions, $d^2N_{AA}/dp_T dy$, are divided by the spectra in pp or $p\bar{p}$ interactions, $d^2N_{NN}/dp_T dy$, obtained at the same energy and scaled by the number of binary nucleon-nucleon interactions, $< N_{coll} >$. It is expected that a lack of nuclear effects involved in particle production should lead to a perfect scaling with N_{coll} at high p_T, i.e. $R_{AA} = 1$, as illustrated in Fig. 7.14. At lower transverse momentum ($p_T < 2$ GeV/c) the particle yield which is related to "soft" partonic processes is predicted to approximately scale with the number of wounded nucleons [107], N_{part}, and small values of R_{AA} are expected. The quenching effect, i.e. suppression of high-p_T yields, is represented in Fig. 7.14 by small values of the nuclear modification factor, $R_{AA} << 1$, while an enhanced production of high-p_T particles in nuclear collisions, called also the "Cronin" effect [141, 142], is related to $R_{AA} > 1$.

All experiments at RHIC performed measurements of transverse momentum distributions of charged ($h^+ + h^-$) particles to study the particle production at large p_T. In this Section mainly PHOBOS results are presented. The PHOBOS experiment measured spectra of charged hadrons produced in Au+Au collisions near mid-rapidity at the full RHIC energy of $\sqrt{s_{NN}} = 200$ GeV [7]. The invariant transverse momentum distributions were already presented in Section 6.2.1 in Fig. 6.14. The p_T spectra were obtained for 6 centrality intervals, ranging from semi-peripheral Au+Au collisions with $\langle N_{coll} \rangle = 107$ to the 6% most central interactions with $\langle N_{coll} \rangle = 1050$. The Au+Au spectra, shown in Fig. 6.14, are compared to the inelastic $p + \bar{p}$ cross section for charged particle production obtained by the UA1 experiment at the same energy of $\sqrt{s_{NN}} = 200$ GeV [143],

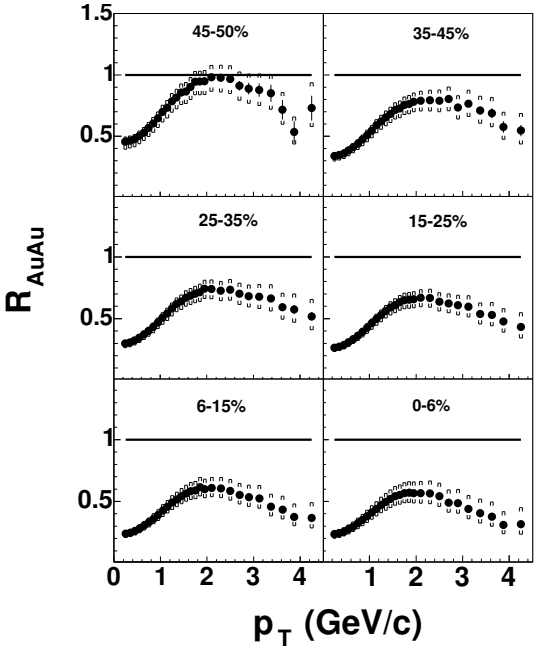

Figure 7.15: *Nuclear modification factor, R_{AuAu}, as a function of transverse momentum for Au+Au collisions at $\sqrt{s_{NN}} = 200$ GeV, for six centrality intervals. Bars (brackets) show the statistical (systematic) uncertainty. The straight line shows the expectation for N_{coll} scaling.*

by means of the nuclear modification factor, R_{AuAu}, defined as

$$R_{AuAu} = \frac{\sigma_{p\overline{p}}^{inel}}{\langle N_{coll} \rangle} \frac{d^2 N_{AuAu}/dp_T d\eta}{d^2 \sigma_{p\overline{p}}^{UA1}/dp_T d\eta}. \tag{7.3}$$

In Fig. 7.15 the nuclear modification factor is presented as a function of transverse momentum for the six centrality intervals. In each centrality range hadron production at high p_T is found to be suppressed ($R_{AuAu} < 1$) relative to the expectation based on an independent superposition of nucleon-nucleon collisions. One can see that the strongest suppression, by a factor of 4 at $p_T = 4$ GeV/c, occurs in the most central collisions.

The PHOBOS data agree with results obtained by the other RHIC experiments [7–9, 11]. The effect of high-p_T suppression was for the first time observed by PHENIX Collaboration in central Au+Au data at 130 GeV [9]. This result was rather unexpected as at SPS energies a "Cronin-like" enhancement in production of high-p_T π^0-s in central Pb+Pb collisions at energy of $\sqrt{s_{NN}} = 17.3$ GeV was observed, $R_{PbPb} > 1$ [144]. It is also interesting to note that, recent results

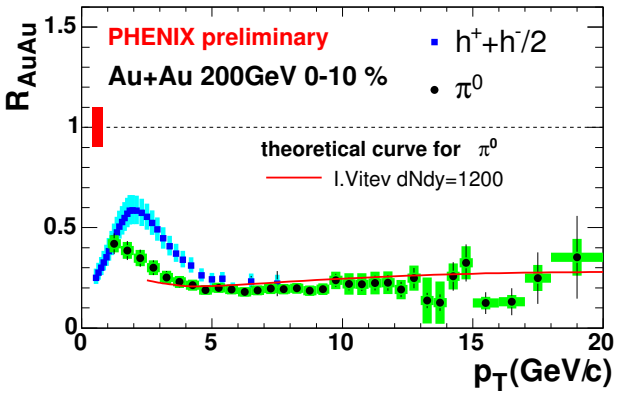

Figure 7.16: *R_{AuAu} of π^o and charged hadrons for the 10% most central Au+Au collisions at $\sqrt{s_{NN}} = 200$ GeV measured by the PHENIX experiment [145]. The solid line represents the results of a theoretical model incorporating parton energy loss in a dense medium [147].*

from PHENIX [145] show, see Fig. 7.16, that the π^0 yield at mid-rapidity in central Au+Au collisions at $\sqrt{s_{NN}} = 200\ GeV$ is still suppressed up to very large transverse momenta of 20 GeV/c.

As discussed above, this suppression can result from final state effects like induced gluon radiation from high-p_T partons moving through a dense medium. Another model [146] also tried to account for this effect by in-medium interactions of hadrons produced from partonic jets. One can see that the experimental data, shown in Fig. 7.16, are consistent with results of a theoretical model incorporating parton energy loss in a very dense medium [147].

An interesting alternative explanation of the high-p_T suppression phenomenon involving initial state effects was also proposed [148]. It was postulated that a significant modification in the gold ion wave functions through the gluon saturation effect, see Section 2.5 for more details, can lead to fewer hard partonic scatterings and consequently to a smaller number of high-p_T hadrons. The scenario incorporating initial state effects to explain the high-p_T suppression can be cross-checked by the d+Au control experiment. In nuclear collisions with one nucleus being small, like a proton or deuteron, the final state effects (after the collision) are considerably suppressed as the transverse size of the produced medium is limited. On the other hand, the initial state effects, like saturation, are still possible. In a parton saturation model [148] a decrease of 25–30% in the d+Au nuclear modification factor R_{dAu} was predicted. Therefore, if in d+Au collisions the high-p_T suppression was observed then the d+Au control experiment would suggest that the suppression is due to initial state effects, otherwise it will indicate that final state effects are responsible for the large deficit of high-p_T hadrons in central Au+Au collisions.

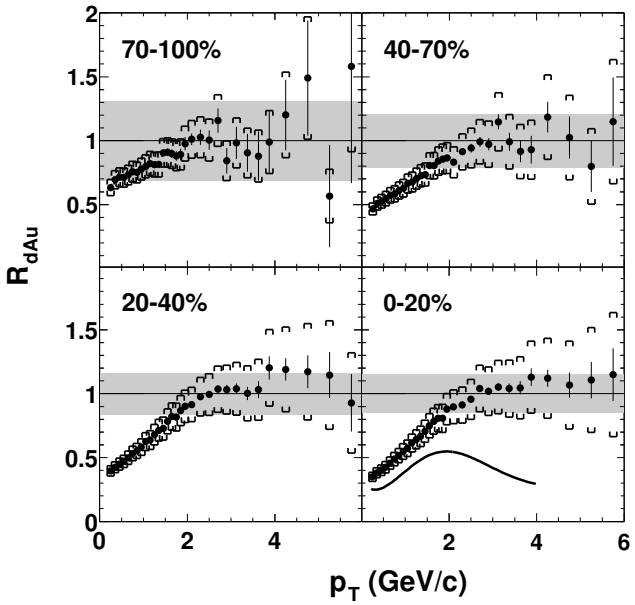

Figure 7.17: *Nuclear modification factor R_{dAu} as a function of p_T for four intervals of centrality. For the most central interval, the spectral shape for central Au+Au data relative to $p + \bar{p}$ is shown for comparison. The shaded area shows the uncertainty in R_{dAu} due to the systematic uncertainty in $\langle N_{coll} \rangle$ and the UA1 scale error. The brackets show the systematic uncertainty of the d+Au spectra measurement.*

The invariant yield of charged hadrons in d+Au collisions at $\sqrt{s_{NN}} = 200\,GeV$, shown in Fig. 6.16, was obtained by PHOBOS [12] in four centrality intervals. In Fig. 7.17 the nuclear modification factor R_{dAu} as a function of p_T for each centrality interval is shown. For all centrality intervals, we observe a rapid rise of R_{dAu} from low p_T, leveling off at p_T of $\approx$ 2 GeV/c. For comparison, we also plot the nuclear modification factor for the 6% most central Au+Au collisions at the same energy in the lower right panel of Fig. 7.17. The average number of collisions undergone by each participating nucleon in central Au+Au collision is close to 6, similar to that of each nucleon from the deuteron in a central d+Au collision. For 2 $GeV/c \leq p_T \leq$ 6 GeV/c the yield of charged particles in d+Au is consistent with N_{coll} scaling of p+p data. For central Au+Au collisions, the ratio of the spectra to $p + \bar{p}$ rises rapidly up to $p_T \approx$ 2 GeV/c, but falls far short of collision scaling at larger p_T, in striking contrast to the behavior for central d+Au collisions.

Predictions for the evolution of R_{dAu} from semi-peripheral collisions to central collisions were made in two qualitatively different models. Calculations based on perturbative QCD [147] show an increase in the maximum value of R_{dAu} at $p_T \approx$ 3.5 GeV/c by 15% (Cronin effect). In contrast, a decrease in R_{dAu} by 25–30% over the same centrality range is predicted in a parton saturation model [148]. Our data disfavor the prediction from the parton saturation model. This suggests

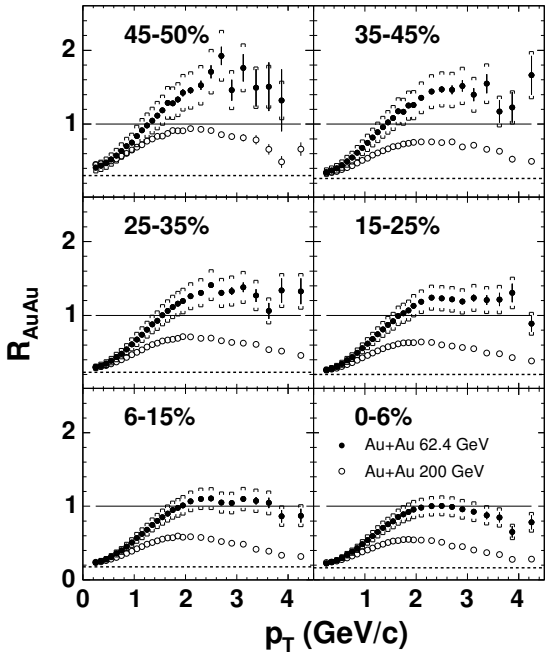

Figure 7.18: *Nuclear modification factor, R_{AuAu}, as a function of transverse momentum for Au+Au collisions at $\sqrt{s_{NN}} = 62.4$ GeV (closed symbols) and 200 GeV (open symbols), for six centrality intervals. Bars (brackets) show the statistical (systematic) uncertainty. The solid (dashed) line shows the expectation for scaling with N_{coll} ($N_{part}/2$) times p+p data.*

that the observed suppression of high-p_T hadrons in Au+Au collisions cannot be accounted for by initial state effects that should also be present in d+Au collisions.

It should be noted that the observation that the data points at higher p_T in Fig. 7.17 are similar at all centralities and all lie near unity may not be evidence for N_{coll} scaling at higher p_T in d+Au. This may be a consequence of the interplay of an "Cronin-like" enhancement [147, 149, 150] and some suppression, due to either energy loss in the final state or parton saturation effects in the initial state. Nevertheless, the data indicate, that the majority of the large difference in R_{AuAu} compared to R_{dAu} results from the impact of the high energy density matter on the yield of high-p_T particles. The results indicate that the constituents of the medium produced in central Au+Au collisions experience a significant level of interaction. We can conclude that the high energy density matter produced at RHIC interacts very strongly with high-p_T particles indicating that the medium at the early stage cannot be primarily hadronic in nature.

The SPS and RHIC results on high-p_T neutral and charged hadron production in central heavy-ion collisions show that the corresponding nuclear modification factors decrease from values greater than 1 down to about 0.2 over the energy range from $\sqrt{s_{NN}} = 17.3$ GeV to 200 GeV. Therefore, it is interesting to check whether the energy dependence of the high-p_T suppression is a smooth or abrupt function of the collision energy. To investigate this energy evolution, PHOBOS measured the yield of charged hadrons produced in collisions of gold nuclei at an energy of $\sqrt{s_{NN}} = 62.4$ GeV [127] which has been already presented in Fig. 6.15.

The centrality evolution of R_{AuAu} for 62.4 GeV data is presented in Fig. 7.18. For comparison, results from Au+Au collisions at 200 GeV are included, using the same centrality intervals. It can be seen, that R_{AuAu} reaches a maximum of

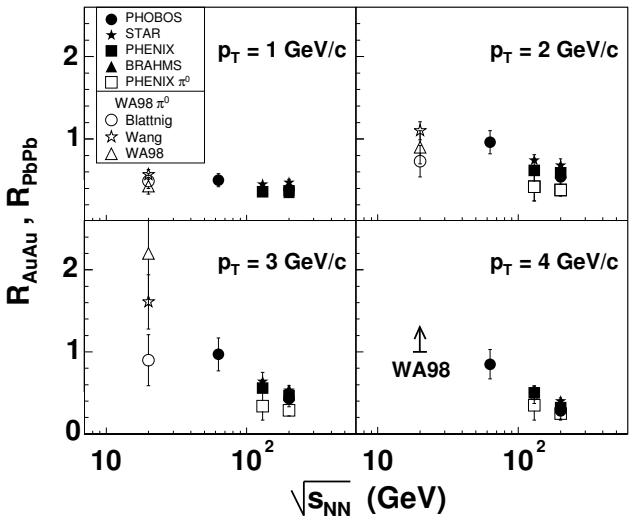

Figure 7.19: *Nuclear modification factor for charged hadrons and π^0 produced at p_T = 1, 2, 3 and 4 GeV/c near mid-rapidity in central heavy-ion collisions, as a function of collision energy. Closed symbols show R_{AuAu} for charged hadrons at RHIC energies, while open symbols show π^0 data. For the WA98 π^0 data, R_{PbPb} is shown using three different parameterizations for the p+p reference spectrum [144, 151, 152]; for p_T = 4 GeV/c, the arrow indicates the lower limit on R_{PbPb}.*

approximately 1.6 for peripheral collisions at 62.4 GeV, whereas the maximum value observed at 200 GeV is close to 1. For both data sets, a significant and systematic decrease in R_{AuAu} is observed when progressing from peripheral to central events.

Focusing on central events, Fig. 7.19 shows the nuclear modification factor R_{AuAu} for the 6% most central Au+Au collisions at $\sqrt{s_{NN}}$ = 62.4 GeV for four different values of p_T ranging from 1 to 4 GeV/c. Results from p+p collisions at the same energy [154] were used in the calculation of R_{AuAu}. The results are compared with results for charged hadrons at $\sqrt{s_{NN}}$ = 130 GeV and 200 GeV. For p_T = 2 GeV/c and above, we observe a smooth decrease of R_{AuAu} from 62.4 to 200 GeV in central Au+Au collisions. Fig. 7.19 shows R_{PbPb} for π^0 production in Pb+Pb collisions at 17.3 GeV from WA98, obtained using three p+p reference parameterizations [144, 151, 152], as well as π^0 data for 130 GeV and 200 GeV from PHENIX [9, 153]. Although the uncertainty in the 17.3 GeV reference distribution is large, the data indicate that the nuclear modification factor for π^0 production at $p_T >$ 3 GeV/c drops from $R_{PbPb} > 1$ at $\sqrt{s_{NN}}$ = 17.3 GeV to $R_{AuAu} < 0.2$ at $\sqrt{s_{NN}}$ = 200 GeV. The data show that the nuclear modification factor for neutral pions is consistently lower than for charged hadrons at the same collision energy, which can be attributed to the different p_T-dependence of meson

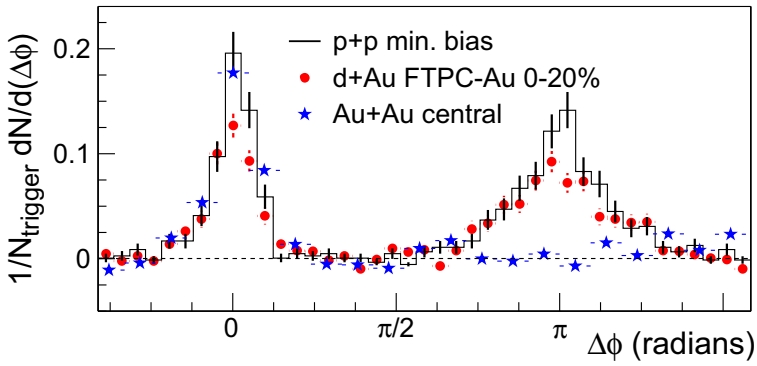

Figure 7.20: *Two-particle azimuthal correlations of high-p_T charged hadrons for p+p, central d+Au and central Au+Au collisions from the STAR experiment [14].*

and baryon spectra [101].

The Azimuthal Correlations between High-p_T Particles. Additional evidence that the medium formed in central Au+Au collisions at the full RHIC energy strongly modifies the production of high-p_T particles was provided by measurements of two-particle azimuthal correlations in the large acceptance RHIC experiments: PHENIX [15] and STAR [14, 16–18]. The azimuthal correlations of p+p, central d+Au and central Au+Au collisions at $\sqrt{s_{NN}} = 200\ GeV$, measured by STAR, are shown in Fig. 7.20. To obtain the distributions, azimuthal angle differences between trigger and associated high-p_T particles are calculated on an event-by-event basis, where the trigger and associated particle transverse momenta are contained within the range of $4\ GeV/c < p_T^{trig} < 6\ GeV/c$ and $2\ GeV/c < p_T^{assoc} < p_T^{trig}$, respectively. A two jet structure can be clearly seen in p+p and d+Au data with two spikes, one around $\phi \approx 0^o$ (near-side peak) and the other one at $\phi \approx 180^o$ (away-side peak). In contrast, in the 5% most central Au+Au collisions the away-side peak is absent, indicating that in central Au+Au the high-p_T particles belong to one jet originating near the surface of the system from the hard scattered parton moving away from the system center, see Fig. 2.4. Final state effects like induced gluon radiation lower the energy of the opposite parton and the jet moving toward the system center gets absorbed in the opaque medium. The energy loss of a parton is expected to depend on the traversed path length in the medium. This jet quenching scenario was additionally confirmed by observation of a stronger suppression of the away-side spike for particles emitted in the out-of-plane direction when compared to the suppression of the away-side correlation for particles measured in-plane in mid-central Au+Au collisions at $\sqrt{s_{NN}} = 200\ GeV$ [18]. See Fig. 5.4 for the reaction plane definition.

7.6 Scaling Properties of the p_T Spectra

The feature that the medium produced in central Au+Au collisions at the highest RHIC energy almost completely absorbs fast particles is well illustrated in Fig. 7.21 which shows the nuclear modification factor, $R_{PC}^{N_{part}}$, defined as

$$R_{PC}^{N_{part}} = \frac{N_{part}^{central}}{N_{part}} \frac{dN_{AuAu}/dp_T}{dN_{AuAu}^{central}/dp_T}, \tag{7.4}$$

where $dN_{AuAu}^{central}/dp_T$ is the p_T spectrum for the 6% most central Au+Au collisions at $\sqrt{s_{NN}} = 200\ GeV$ while dN_{AuAu}/dp_T represent all spectra at different centralty bins, shown in Fig. 6.14. Corresponding numbers of wounded nucleons are presented in Table 5.2. In Fig. 7.21, yields at a given transverse momentum in collisions of varying centrality were normalized by N_{part} and then divided by a fit to the same quantity in the most central data. Thus, $R_{PC}^{N_{part}}$ shows the variation in yield per participant relative to central Au+Au collisions. One can see that the medium modification results in charged particle yields that, over the centrality range studied here, more closely scale with N_{part} than with the number of binary nucleon-nucleon interactions, even for transverse momenta above

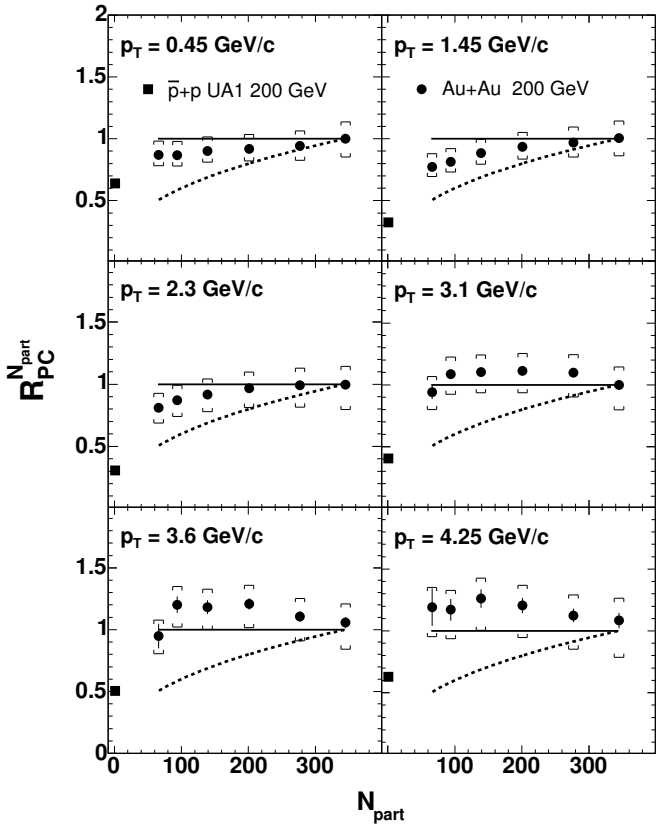

Figure 7.21: $R_{PC}^{N_{part}}$ *as a function of centrality for Au+Au collisions at* $\sqrt{s_{NN}} = 200\ GeV$, *for six transverse momentum ranges. The solid (dashed) line shows the expectation for* N_{part} *(*N_{coll}*) scaling from peripheral to central collisions. Squares show data for p+p collisions from UA1 [143] with the same normalization factor.*

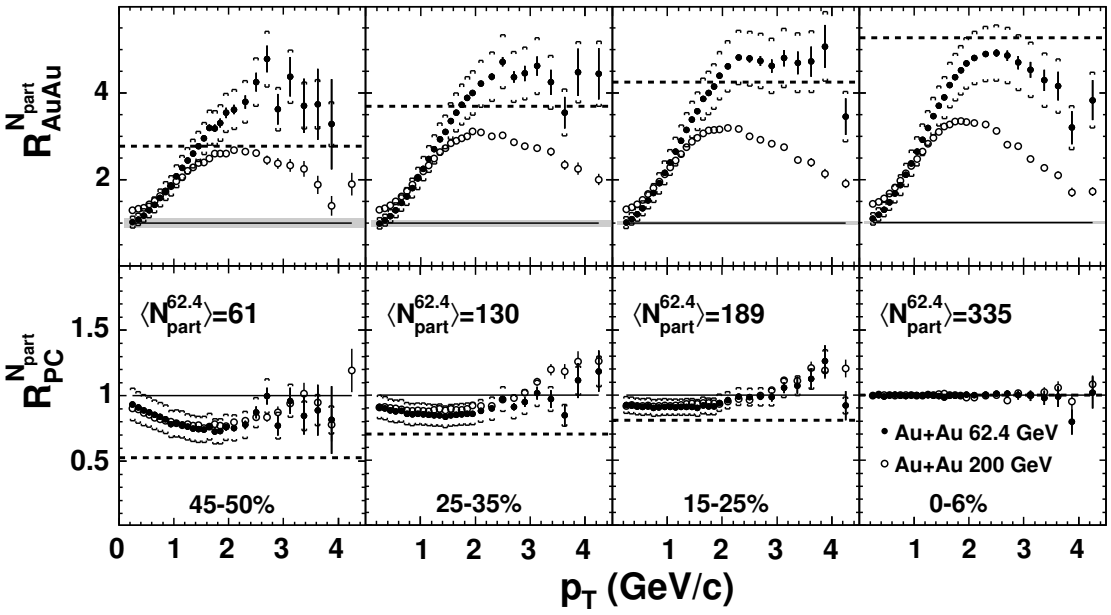

Figure 7.22: *Nuclear modification factors, $R^{N_{part}}_{AuAu}$ and $R^{N_{part}}_{PC}$ for Au+Au collisions at two energies of $\sqrt{s_{NN}}$ = 62.4 GeV (closed symbols) and 200 GeV (open symbols) versus transverse momentum and collision centrality [127]. The grey bands in the top row show the systematic error in the overall scale due to N_{part}. The solid (dashed) line shows the expectation for N_{part} (N_{coll}) scaling.*

4 GeV/c. The observation of N_{part} scaling at high transverse momentum suggests that the medium is almost completely opaque to produced fast particles. For the absorbing medium, final production originates from the surface of the collision system while the rest of the volume appears to be "black". In such a scenario, the production is suppressed by a factor of the surface to volume ratio which is similar to the ratio of N_{part} to N_{coll}.

The data from Au+Au collisions at energy of 62.4 GeV and 200 GeV, already presented in Sections 7.5 and 6.2.1, can be used to study the N_{part} scaling of the transverse momentum distributions as a function of both collision centrality and energy. In Fig. 7.22, particle production as a function of centrality and p_T is shown for these two energies in terms of $R^{N_{part}}_{AuAu}$ and $R^{N_{part}}_{PC}$. $R^{N_{part}}_{PC}$ was previously defined by Eq. 7.4 while

$$R^{N_{part}}_{AuAu} = \frac{1}{N_{part}/2} \frac{dN_{AuAu}/dp_T}{dN_{pp}/dp_T}, \tag{7.5}$$

where dN_{pp}/dp_T is transverse momentum distribution in p+p collisions, adopted from [143, 154]. $R^{N_{part}}_{AuAu}$ shows the variation in the yield per participant pair

relative to p+p collisions.

The p_T range from a few hundred MeV/c to more than 4 GeV/c is expected to be affected by very different mechanisms of particle production, from soft coherent processes to independent hard partonic scattering. Over the collision energy range from 62.4 to 200 GeV, the overall particle production in p+p increases by less than a factor 2, whereas the yield at $p_T = 4\ GeV/c$ increases by an order of magnitude. This large increase of the yield is not preserved in central Au+Au collisions. For central Au+Au collisions, the ratio of the yields at 200 GeV to the yield at 62.4 GeV for $p_T = 4\ GeV/c$ is about 4 while the ratio of p_T-integrated multiplicities is 1.6.

The top panel in Fig. 7.22 shows that $R_{AuAu}^{N_{part}}$ depends strongly on beam energy while the centrality dependence of the yield normalized to the number of participating nucleons for a given energy is weak. At both energies the yield per participant changes by less than 25% within the centrality range from 60 to 340 participants. The bottom panel of plots, shown in Fig. 7.22, also demonstrates that the variation of the yield per participant pair is the same for both energies over the full p_T and centrality range. This means that the energy and centrality dependences of particle p_T yields factorize. This is particularly interesting, as the factorization covers both the bulk particle production at low p_T, as well as rare particle production at high p_T, dominated by completely different particle production mechanisms. The N_{part} scaling present in the production of slow and fast particles over the large range of centrailies and transverse momentum indicates that at both RHIC energies a strongly coupled system, which is opaque to fast particles, is formed.

Chapter 8

The RHIC Discovery of a Strongly Coupled Quark-Gluon Plasma

The results, shown in the previous Chapter, on single particle spectra at very low, intermediate and high transverse momentum consistently demonstrate that the constituents of the medium produced in central Au+Au collisions experience a significant level of interaction. It is reasonable to expect from these results that the system created in nuclear collisions at RHIC does not behave like a weakly interacting partonic gas as was commonly stated before the RHIC era. Further evidence from the PHOBOS experiment that the medium is not primarily a hadronic state but a new one, strongly coupled Quark-Gluon Plasma (sQGP) [24, 25], is presented in this Chapter.

8.1 Initial State of Nucleus-Nucleus Collisions

The one of the key parameters describing the medium produced in relativistic heavy-ion collisions is the energy density. The energy density can be estimated using the multiplicity of produced particles. Fig. 8.1 shows the pseudorapidity density of charged particles produced in Au+Au collisions at $\sqrt{s_{_{NN}}} = 200\,GeV$ in six centrality intervals, measured by the PHOBOS experiment [112]. The pseudorapidity densities reach a maximum near mid-rapidity and increase with collision centrality. In the 6% most central Au+Au collisions $dN_{ch}/d\eta|_{|\eta|\leq 1} = 655 \pm 35$ near mid-rapidity and an average number of all produced charged particles over the whole pseudorapidity range is $N_{tot} = 5060 \pm 250$. From the pseudorapidity densities, extrapolating backward, one can estimate the energy of the medium produced in nuclear collision. It is expected that bulk of particle production near mid-rapidity originates from a system which is in equilibrium. Near mid-rapidity

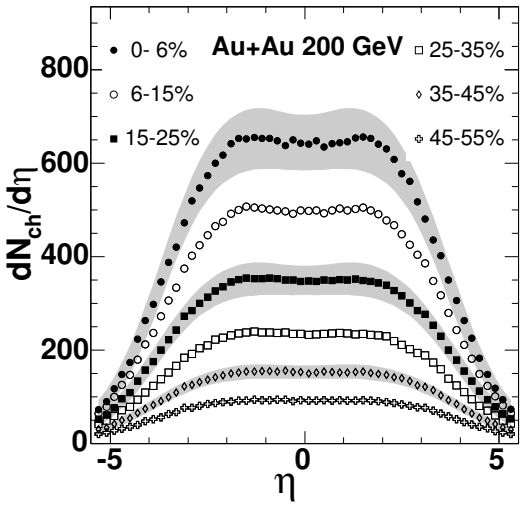

Figure 8.1: *Pseudorapidity density of charged particles produced in Au+Au collisions at* $\sqrt{s_{NN}} = 200\ GeV$ *in six centrality intervals. Grey bands plotted for selected centralities show systematic uncertainties.*

($|\eta| \leq 1$) the majority of particles have their transverse and longitudinal momenta components comparable. Assuming a spherically symmetric distribution of particles in momentum space and attributing each particle an average energy of 600 MeV (see Section 6.1.2) one can find [2] that for the 6% most central collisions the total energy carried by produced particles is about 1.6 TeV, which is approximately 4% of the total energy of the colliding nuclei (i.e. 39.4 TeV).

There have been numerous discussions in literature concerning the volume of the medium at the time when an equilibrium is attained. While the size of the transverse area of the system is easily estimated from the centrality, the longitudinal scale is difficult to determine. Typically [155], it is assumed that the time needed to form an equilibrated system after nuclear collision is of the order of $\tau \approx 1\ fm/c$ (equivalent to the longitudinal size of 2 fm). This assumption implies that for head-on Au+Au collisions with transverse area of 150 fm^2 the energy density is about $\epsilon \approx 5\ GeV/fm^3$. Elliptic flow results, discussed below, indicate that the upper limit for the time to reach equilibrium is of the order of $1 - 2\ fm/c$. Therefore, a more conservative estimation (with $\tau = 2\ fm/c$) requires that the energy density should be $\epsilon \geq 3\ GeV/fm^3$.

These estimates are in agreement with the PHENIX evaluation of the energy density based on their transverse energy measurements and Bjorken's formula [155, 156]. The value of ϵ obtained at the SPS in central lead-lead collisions at $\sqrt{s_{NN}} = 17.3\ GeV$ is around 3 GeV/fm^3 [157].

The increase of the energy density with the collision energy is accompanied by an increase of the antiproton to proton ratio, see Fig. 7.13, thus, the produced medium is approaching the net-baryon free environment. As discussed in Section 7.4, the baryochemical potential of $\mu_B = 27 \pm 2\ MeV$ was measured in central Au+Au collisions at $\sqrt{s_{_{NN}}} = \ 200\ GeV$. Therefore, the baryochemical potential at the highest RHIC energy is near the limit of $\mu_B = 0$ and at the point where lattice QCD calculations clearly show an abrupt phase transition between hadronic matter and QGP [39, 40] at the critical energy density within the range of $\epsilon_c \approx \ 0.6 - 1\ GeV/fm^3$. The experimental results for energy density indicate that the critical energy density has been far exceeded in Au+Au collisions at RHIC, thus, describing the system in terms of hadronic degrees of freedom does not seem to be appropriate.

8.2 Strongly Coupled System

Measurements at RHIC provide substantial evidence that the medium produced in central Au+Au collision at the highest RHIC energy should constitute a new state of matter with properties not expected prior to the RHIC era. For many years, it was believed that a Quark-Gluon Plasma should be composed of weakly interacting particles and that a perturbative approach can describe its properties. However, the RHIC results including single particle spectra at very low, intermediate and high $p_{_T}$, and azimuthal correlations presented in the previous Chapters, consistently demonstrate that such views cannot be sustained. Additional evidence that the medium formed at RHIC in Au+Au collisions is a strongly coupled system comes from elliptic flow measurements. The initial geometry of the interacting system in the plane perpendicular to the beam direction corresponds to the almond-shaped overlap area, shown in Fig. 5.4. Assuming that particle production in heavy-ion collisions is an independent superposition of particles produced from binary nucleon-nucleon interactions one could expect that the final azimuthal distribution of produced particles in a AA collision would be uniform. Therefore, observation of an asymmetric azimuthal distributions of detected particles in nuclear collisions, on an event-by-event basis, provides direct evidence for the level of interactions in the system. To study the azimuthal asymmetry of produced particles, it is convenient to introduce a Fourier series:

$$\frac{dN}{d(\phi - \psi_R)} = \sum_n 2v_n cos(n(\phi - \psi_R)). \tag{8.1}$$

where v_2 is the elliptic flow coefficient and ψ_R stands for the azimuthal angle of the true reaction plane. The elliptic flow of charged particles ($|\eta| < 1$), measured by the PHOBOS experiment, as a function of centrality in Au+Au collisions at

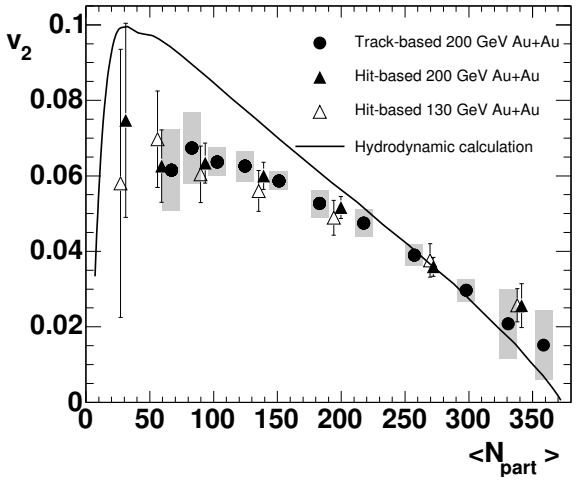

Figure 8.2: *Elliptic flow of charged particles as a function of centrality in Au+Au collisions at* $\sqrt{s_{NN}} = 200\ GeV$ *obtained with two different methods [158] (closed circles and triangles) and at* $\sqrt{s_{NN}} = 130\ GeV$ *(open triangles) [159]. The curve shows the prediction from a relativistic hydrodynamical calculation [160].*

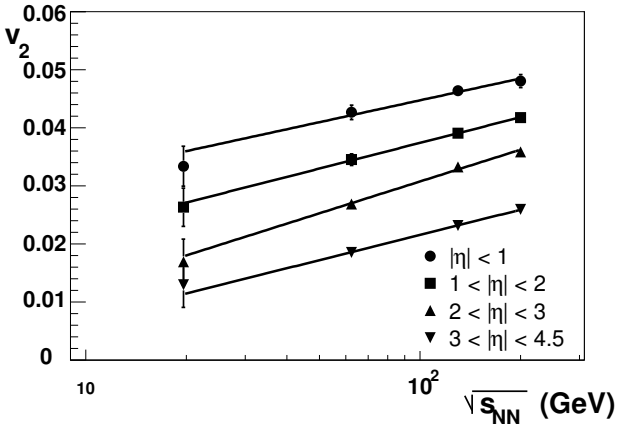

Figure 8.3: *The* $\sqrt{s_{NN}}$ *evolution of the elliptic flow in* η *bins, averaged over centrality (0-40%). The lines represent fits to the data.*

$\sqrt{s_{NN}} = 200\ GeV$ is shown in Fig. 8.2 while the energy dependence of v_2 for Au+Au collisions within 0-40% centrality bin is presented in Fig. 8.3. One can see that the highest level of interactions is observed in the system formed at the highest RHIC energy as v_2 significantly increases over the evergy interval ranging from 20 GeV up to 200 GeV.

Hydrodynamical models were used to calculate a relationship between the initial shape of the interacting system and the distribution of emitted particles [160]. The asymmetric initial shape of the interacting system, treated as an ideal fluid, leads to additional pressure gradients which in turn alter the observed particle directions. Due to the perfect nature of the fluid (ideal fluid flow is assumed in these models) the predicted final asymmetry, v_2, shown by the solid line in Fig 8.2, is usually treated as an upper limit. As one can see the model prediction is consistent with the experimental data for mid-central Au+Au collisions at $\sqrt{s_{NN}} = 200\ GeV$. The time needed for the pressure build up, was estimated in the hydrodynamical model [161] to be less than 2 fm/c, with an expected value of 0.6 fm/c, indicating that a strongly coupled system, resembling a perfect fluid in equilibrium, is already formed at early times of its evolution.

Chapter 9

Summary and Conclusions

The Relativistic Heavy Ion Collider at BNL opened a unique opportunity to study matter at the highest energy density ever produced in the laboratory. The new results from RHIC have provided evidence for the production of a new form of matter with unexpected properties, in central Au+Au collisions. Treating the system as a weakly interacting gas of quasi-particles, e.g. a weakly coupled QGP described by a perturbative weak-coupling approach, does not seem to be appropriate. The PHOBOS experiment at RHIC, designed to measure the density distributions of charged particles produced within almost the full solid angle as well as charged particle spectra near mid-rapidity in a wide range of transverse momentum, from 0.03 GeV/c up to about 5 GeV/c, has provided a vast amount of results for different types and energies of colliding nuclei. The results on charged particle densities indicate that in the most central Au+Au collisions at $\sqrt{s_{NN}} = 200\ GeV$ the energy density exceeds 3 GeV/fm^3. It is expected that at such extreme densities hadronic degrees of freedom do not seem to be relevant in describing the system. The direct evidence that a strongly coupled plasma is produced, is provided by measurements of transverse momentum distributions of charged hadrons at high p_T. The high-p_T component of the p_T spectrum probes initial/final state effects involved in the production of particles with large transverse momenta. The charged hadron spectra in Au+Au and d+Au collisions at the highest RHIC energy of $\sqrt{s_{NN}} = 200\ GeV$ were measured by PHOBOS up to about 5 GeV/c in p_T. The yield of high-p_T charged hadrons per binary nucleon-nucleon interaction is observed to be strongly suppressed in central Au+Au collisions as compared to the yield in $p + \bar{p}$. The results, together with data from the d+Au control experiment where no such suppression is observed, indicate that final state in-medium effects, e.g. energy loss of hard scattered partons through induced gluon radiation, are responsible for this suppression. Only very large energy losses in the medium, much larger than in "cold" hadronic matter, can account for the observed suppression. The data also indicate that yields of charged particles at high p_T per wounded nucleon

in Au+Au collisions show weaker dependence on centrality than the yields normalized to the number of binary nucleon-nucleon interactions. This N_{part} scaling indicates that surface emission dominates particle production at large transverse momenta. This conclusion is also strongly supported by the disappearance of the away-side azimuthal correlations of high-p_T particles in central Au+Au collisions at $\sqrt{s_{NN}} = 200\ GeV$. A smooth decrease of the nuclear modification factor at high-p_T in central Au+Au collisions within the energy range of 20 and 200 GeV is observed.

The study of particle p_T spectra at very low transverse momentum provided additional information on the properties of the new state of matter formed in central Au+Au collisions. The very low momentum reach of the PHOBOS experiment allows to search for new phenomena in central heavy-ion collisions at the highest RHIC energy. In particular, an enhancement of particle production at very low p_T was predicted provided that the medium consist of weakly interacting particles. The charged particle p_T spectra of $(\pi^+ + \pi^-)$, $(K^+ + K^-)$ and $(p+\overline{p})$ at very low transverse momenta in the 15% most central Au+Au collisions at $\sqrt{s_{NN}} = 200\ GeV$ were obtained using a new technique, developed to reconstruct and identify low-p_T particles which range out in the first silicon layers. The identified particle yields were measured at mid-rapidity in the transverse momentum ranges from 30 to 50 MeV/c for charged pions, 90 to 130 MeV/c for charged kaons and 140 to 210 MeV/c for protons and antiprotons. The low-p_T spectra have been also measured in Au+Au collisions at $\sqrt{s_{NN}} = 62.4\ GeV$ and d+Au collisions at $\sqrt{s_{NN}} = 200\ GeV$. No significant enhancement in low transverse momentum particle production is observed in Au+Au collisions as compared to extrapolations of identified particle spectra measured at intermediate p_T. The observation that there is no such excess could be a manifestation of the high pressure gradients and significant level of interactions present in the medium, which could produce large collective transverse flow ("blast wave") so that any particles initially produced with low velocity would subsequently be accelerated by the interactions. This dynamic behavior is consistent with the large magnitude of the elliptic flow signal seen at RHIC. It was found that the blast wave model well describes the particle yields at very low and intermediate p_T. Thus, the results at very low p_T provide additional indirect evidence that the constituents of the system produced in heavy-ion collisions at RHIC are strongly coupled.

Scaling of m_T spectra for different identified particles were studied in Au+Au and d+Au collisions at 200 GeV. It was predicted by saturation models that the m_T spectra should follow a single universal curve. However, the Au+Au spectral shapes at 200 GeV are only similar at higher transverse masses ($m_T > 1.7\ GeV/c$) while at low m_T a flattening of $(K^+ + K^-)$ and $(p + \bar{p})$ spectra, consistent with collective transverse expansion, is observed. The flattening of the $(p+\bar{p})$ spectrum is significantly stronger than the one observed for the spectra of charged kaons in central Au+Au collisions. In contrast, in d+Au collisions no such flattening is

present and the shapes of $m_{_T}$ spectra are similar at low and intermediate $p_{_T}$.

Various comparisons with model predictions illustrate that the experimental results on low $p_{_T}$ yields of $(\pi^+ + \pi^-)$, $(K^+ + K^-)$ and $(p + \overline{p})$ in Au+Au collisions provide an excellent handle on radial flow. In particular, the hydrodynamical models turned out to be quite successful in describing properties of the $p_{_T}$ spectra, indicating the medium may behave like a perfect fluid.

In PHOBOS, antiparticle to particle ratios have been obtained for pions, kaons, and protons near midrapidity in central Au+Au collisions at $\sqrt{s_{_{NN}}}$= 62.4, 130 and 200 GeV. The $\langle K^- \rangle / \langle K^+ \rangle$ and $\langle \bar{p} \rangle / \langle p \rangle$ ratios in Au+Au collisions at $\sqrt{s_{_{NN}}} =$ 200 GeV are consistent with a baryochemical potential μ_B of 27 MeV and temperature of chemical freeze-out of 165 MeV. The results indicate that the medium is composed of hot matter with a high level of equilibrium and close to the limit of $\mu_B = 0$ where lattice QCD calculation clearly show the phase transition between hadronic matter and QGP.

The new phenomena observed at RHIC and presented in this paper, i.e. high-$p_{_T}$ suppression, disappearance of away-side azimuthal correlations, no enhancement of very low-$p_{_T}$ particles, flattening of $m_{_T}$ spectra at very low and intermediate transverse momenta as well as large elliptic flow provide strong evidence that the dense and hot system created in central Au+Au collisions at the highest RHIC energy is a strongly coupled Quark-Gluon Plasma with properties resembling those of a perfect fluid.

Acknowledgments

First and foremost I wish to thank Prof. B. Wosiek and Prof. R. Hołyński for comments and discussions during the preparation of this report.

I owe Prof. W. Busza and Dr M. Baker a large debt of gratitude for their support and encouragement to study low-p_T physics of identified particles. I acknowledge collaboration with Prof. B. Wosiek, Dr P. Sawicki and Mgr T. Gburek. I thank the review committee of all low-p_T analyses, i.e. Prof. S. Manly, Dr C. Roland, Dr P. Steinberg and Dr A. Wuosmaa who provided many useful suggestions to the publications on low-p_T yields. I thank Dr A. Olszewski and Dr K. Woźniak for discussions.

I wish to thank Dr R. S. Hollis for English proof-reading of the manuscript and for useful comments.

I would like to thank the MIT and BNL PHOBOS heavy-ion groups for their support and for the warm hospitality during my work at the PHOBOS experiment.

I especially acknowledge co-operation with Mgr K. Gałuszka, Dr N. George, Dr K. Gulbrandsen, Mgr J. Kotuła, J. Mülmenstädt, Dr G. van Nieuwenhuizen, Dr R. Nouicer, Dr G.S.F. Stephans, Dr M. Stodulski, Dr R. Verdier, Prof. F. Wolfs, Dr K. Woźniak and Mgr P. Żychowski during work on the geometrical description of the PHOBOS detector.

Appendix A

Systematic Errors of Low-p_T Particle Yields

A.1 Systematic Errors Related to Background Corrections

The dominant contribution to the systematic errors is due to the uncertainty in the background estimates which are evaluated to be approximately 28% for $(p+\overline{p})$ and about 10% for charged pions and kaons. As already discussed in Section 6.1.2, the large systematic error of the $(p+\overline{p})$ correction is due uncertainty in fitting contributions from weak decays and secondary interactions in DCA distributions. Uncertainties in background determination for charged pions and kaons are estimated from Monte Carlo simulations based on an independent Au+Au collision model inspired by measured $p_{_T}$ spectra. The basic particles $(\pi^{\pm}, K^{\pm}, p, \overline{p}, \Lambda)$ for background estimates were generated with $p_{_T}$ spectra matching our low momentum measurements as well as the published results at higher $p_{_T}$ [65–67] with a flat distribution in the rapidity range $|y| < 2$. The particle composition was assumed to agree with the measured particle ratios. Such generated events were then run through the full GEANT simulations of the detector response and subsequently reconstructed. Although, the total number of fully simulated data-like events was restricted to 81000 due to extensive CPU time, accumulated statistics of reconstructed particles was sufficient for an independent background estimate. Comparing the results from the data-like simulations and results based on the HIJING model, presented in Section 6.1.2, gives a reasonable estimate of uncertainties in charged pions and kaons background determination, shown in Table 6.8.

A.2 Method-Related Systematic Errors

The uncertainties related to the analysis method were estimated by performing the reconstruction with varied selection criteria. For this purpose an independent reconstruction code was developed with much looser cuts on dE/dx implemented. Instead of the mass hypothesis cuts used in the standard procedure, defined by Eq. 6.1, the following much wider cuts were utilized: $|(dE/dx)_i - < dE/dx >_i | < 3\sigma_i$. In the new procedure, also the momentum hypothesis cuts (described in Section 6.1.1.F) were substituted with more detailed cuts in (M_p, E_{tot}) scatter plots, where allowed regions (contours) were defined, using reconstructed single simulated particles, to enclose points of low-p_T pions, kaons and protons, as shown in Fig. 6.5. Four separate sets of contours, were used (for each arm and the two ranges in θ). With the new procedure applied to the experimental data more tracks were reconstructed, by a factor of 3 for pions and a factor of 2 for kaons and protons. Reconstructing the Monte Carlo data showed larger contaminations by misidentified particles and ghost tracks for pion and kaon samples. The particle spectra obtained with this new method were compared to the spectra obtained with the standard procedure. Found differences of 1%, 2% and 8% for pion, kaon and proton yields, respectively, contribute to the systematics error related to the analysis method.

Another positive cross-check of the robustness of the reconstruction method comes from analyzing negatively charged pions. Negative particles, stopping in the fifth silicon layer can deposit in this layers much more energy than positively charged particles. According to Monte Carlo simulations, making a cut $(dE/dx)_5 > 7\ MeV$ one should select a rather clean sample of negative pions. Applying this cut to the experimental data together with the standard reconstruction procedure a sample of 2200 negative pions was extracted. The entire reconstruction chain was completed to obtain the spectra of negative pions. Comparing spectra of negative pions with spectra of charged pions divided by 2 only 2.4% difference was found. The chance that this agreement is accidental is small, as the number of reconstructed negative pions is a factor 7 smaller than the number of charged pions found with the standard procedure.

There are also uncertainties related to the reconstruction method which can be estimated by the analysis of Monte Carlo data. In this consistency check true HIJING momentum distributions of primary particles are compared with the acceptance and efficiency corrected yields of reconstructed primary particles using the sample of about 100000 HIJING events described in Section 6.1.2. In this method, the efficiency and acceptance corrections were obtained from embedding tracks into HIJING events. Found differences of 0.4%, 11% and 9% for pion, kaon and proton yields, respectively, were also added to the systematic errors related to the analysis method. An analogous procedure was applied to the data-like simulation (described in the previous Section). The reconstructed

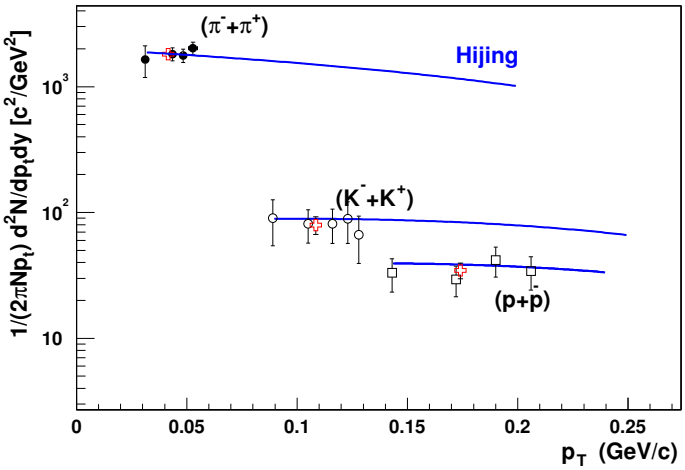

Figure A.1: *Comparison of the true (curves) and reconstructed (points) HIJING spectra. The crosses indicate the reconstructed yield averaged over the whole p_T range.*

and true HIJING spectra are depicted in Fig. A.1.

In addition, uncertainty in the p_T scale was estimated to be 5%. This error comprises the uncertainties related to the method of momentum determination (see Section 6.1.1.I) as well as the contribution from the energy scale, discussed in more details in the next Section.

The sensitivity to the GEANT energy threshold also contributes to the systematic errors related to the reconstruction method. In the detector simulations, the energy thresholds for tracking particles in GEANT are set to 0.1 MeV. To check the effect of these thresholds smaller values of 0.05 MeV were used. With E_{th} set to 0.05 MeV particle spectra were recalculated. Comparison of acceptance and efficiency corrected yields from the standard procedure (with $E_{th} = 0.1$ MeV) with that obtained by embedding tracks simulated with $E_{th} = 0.05$ MeV was done. Found differences were of the order of 1%.

A.3 Detector-Induced Systematic Errors

The dominant contributions to the detector-related systematics errors come from the differences in particle yields measured separately in the two spectrometer arms. During the reconstruction each arm of the Spectrometer is treated as a separate detector. Particle yields obtained for individual arm are later averaged. The final yields and yields of each individual arm differ by about 2%, 4% and 5% for pions, kaons and protons, respectively.

During the Physics Run-02 when the Au+Au data at 200 GeV was taken the detector experienced a large, accidental radiation dose (called "BLAST") due

to a failure in controlling the ion beams at the RHIC accelerator. Due to this extra radiation a significant fraction of channels of silicon detectors were broken. This defect is taken into account in the analysis procedure by means of two Dead Channel Maps (DCM), calculated for the data collected before and after BLAST. The effect of different DCMs on the final yields was found to be of the order of 1%, 0.5% and 2% for pions, kaons and protons, respectively.

Especially for the purpose of studying systematic uncertainties related to the magnetic field experimental data were taken with two magnetic field polarities. Before every new store when the ion beams were in collision mode in the RHIC accelerator, experimenters were setting a new magnetic field polarity just by changing the direction of the electric current in the magnet coils of the Spectrometer, while the absolute value of the current ($\sim 3000A$) was unchanged. This procedure ensured that fractions of the data taken with opposite polarities are approximately equal. Calculating the acceptance and efficiency corrected yields for both polarities and comparing them with yields obtained from the standard reconstruction gives differences of 1%, 0.5% and 2% for pions, kaons and protons, respectively.

For the reconstruction procedure of low-p_T particles it was important to verify that the measured ionization energy losses in silicon detectors are matching values obtained from GEANT simulations. Studying stopping particles gives a unique possibility to verify the energy scale used in the experimental data. As already discussed in Section A.2 a sample of negative pions can be selected requiring only that the energy deposited in the $5th$ plane (normalized to 300 μm of silicon) is larger than 7 MeV. For the purpose of setting the energy scale, all other cuts imposed in ionization energy losses (e.g. mass and momentum hypothesis cuts) cannot be used. Selecting negative pions both from experimental data and Monte Carlo sample and comparing their dE/dx distributions at the first three silicon layers indicates that Monte Carlo calculated ionization energy losses are by 11% larger than the measured one. On the other hand, GEANT predictions of low momentum proton ionization energy losses well agree with the experimental values tabulated in Ref. [122]. Thus, it is reasonable to assume that GEANT predicts ionization energy losses correctly and that PHOBOS data need additional scaling factor of $s_F = 1.11$. To estimate the systematic error related to s_F it was assumed that the scaling factor can vary between 1.09 to 1.13 as the determination of s_F is limited by the statistics of low momentum negative pions reconstructed from the Monte Carlo data. Comparing the yields corrected for the acceptance and efficiency at the two limiting values of s_F gives differences of 3%, 2% and 4% for pions, kaons and protons, respectively.

Other detector effects such as misalignment of the spectrometer layers, and the accuracy of the vertex position, were found to be negligible.

Appendix B

Invariant Inclusive p_T Distributions

Data for the invariant yields, Y (defined in Eq. 6.5), of $(\pi^+ + \pi^-)$, $(K^+ + K^-)$ and $(p + \overline{p})$ at very low $p_{_T}$ for the minimum bias d+Au events are presented in Table B.1. The yields are acceptance, efficiency and background corrected using the analysis method described in Section 6.1.2.

The low-$p_{_T}$ data, corrected for the detector effects and background, for the invariant yields in the 15% most central Au + Au collisions at $\sqrt{s_{_{NN}}} = 200\ GeV$ are presented in Table B.2.

The acceptance, efficiency and background corrected $p_{_T}$ spectra of $(\pi^+ + \pi^-)$, $(K^+ + K^-)$ and $(p + \overline{p})$ in Au+Au collisions at 62.4 GeV are presented in Tables B.3, B.4 and B.5 for three centrality intervals: 0-15%, 15-30% and 30-50%, respectively.

Table B.1: *Acceptance, efficiency and background corrected transverse momentum distributions of* $(\pi^+ + \pi^-)$, $(K^+ + K^-)$ *and* $(p + \overline{p})$ *in the minimum bias d + Au collisions at* $\sqrt{s_{_{NN}}} = 200\ GeV$.

Particle ID	$< p_{_T} >$ $[GeV/c]$	Δy	$< m_{_T} >$ $[GeV/c^2]$	$Y \pm$ *stat. err.* $\pm$ *syst. err.* $[c^2/GeV^2]$
$(\pi^+ + \pi^-)$	0.031	$0.30 \div 0.40$	0.14300	$37.5 \pm 5.4 \pm 12.7$
	0.044	$0.20 \div 0.30$	0.14620	$31.5 \pm 2.3 \pm 10.4$
	0.048	$0.10 \div 0.20$	0.14774	$35.7 \pm 2.7 \pm 11.8$
	0.053	$-0.10 \div 0.10$	0.14924	$33.1 \pm 2.7 \pm 10.9$
$K^+ + K^-$	0.104	$-0.05 \div 0.25$	0.50452	$1.70 \pm 0.19 \pm 0.6$
$p + \overline{p}$	0.172	$-0.05 \div 0.20$	0.95391	$0.406 \pm 0.042 \pm 0.11$

Table B.2: *Acceptance, efficiency and background corrected transverse momentum distributions of* $(\pi^+ + \pi^-)$, $(K^+ + K^-)$ *and* $(p + \overline{p})$ *in the 15% most central Au + Au collisions at* $\sqrt{s_{_{NN}}} =$ 200 *GeV*.

Particle ID	$< p_{_T} >$ $[GeV/c]$	Δy	$< m_{_T} >$ $[GeV/c^2]$	$Y \pm$ *stat. err.* $\pm$ *syst. err.* $[c^2/GeV^2]$
$(\pi^+ + \pi^-)$	0.031	0.30-0.40	0.14300	$1478 \pm 106 \pm 177$
	0.044	0.20-0.30	0.14620	$1288 \pm 51 \pm 155$
	0.048	0.10-0.20	0.14774	$1388 \pm 51 \pm 167$
	0.053	-0.10-0.10	0.14924	$1525 \pm 54 \pm 183$
$K^+ + K^-$	0.096	0.15-0.25	0.50298	$47.4 \pm 3.7 \pm 8.5$
	0.116	0.10-0.15	0.50709	$51.0 \pm 4.9 \pm 9.2$
	0.123	0.05-0.10	0.50875	$58.3 \pm 5.6 \pm 10.5$
	0.128	-0.05-0.05	0.51007	$62.9 \pm 6.2 \pm 11.3$
$p + \overline{p}$	0.143	0.15-0.20	0.94909	$7.5 \pm 0.9 \pm 2.4$
	0.172	0.10-0.15	0.95387	$7.1 \pm 0.8 \pm 2.3$
	0.190	0.05-0.10	0.95732	$6.5 \pm 0.8 \pm 2.3$
	0.206	-0.05-0.05	0.96055	$6.7 \pm 0.8 \pm 2.2$

Table B.3: *Centrality 0-15%. Final results on particle yields in Au+Au collisions at* 62.4 *GeV after acceptance, efficiency and background corrections.*

Particle ID	$< p_{_T} >$ $[GeV/c]$	Δy	$< m_{_T} >$ $[GeV/c^2]$	$Y \pm$ *stat. err.* $\pm$ *syst. err.* $[c^2/GeV^2]$
$(\pi^+ + \pi^-)$	0.031	$0.30 \div 0.40$	0.14300	$1284.9 \pm 78.6 \pm 293.0$
	0.044	$0.20 \div 0.30$	0.14620	$1099.0 \pm 34.7 \pm 250.6$
	0.048	$0.10 \div 0.20$	0.14774	$1154.2 \pm 38.0 \pm 263.2$
	0.053	$-0.10 \div 0.10$	0.14924	$1265.9 \pm 42.3 \pm 288.6$
$K^+ + K^-$	0.096	$0.15 \div 0.25$	0.50298	$38.6 \pm 2.8 \pm 9.7$
	0.116	$0.10 \div 0.15$	0.50709	$43.4 \pm 3.6 \pm 10.9$
	0.123	$0.05 \div 0.10$	0.50875	$46.8 \pm 4.7 \pm 11.8$
	0.128	$-0.05 \div 0.05$	0.51007	$47.4 \pm 4.5 \pm 11.9$
$p + \overline{p}$	0.143	$0.15 \div 0.20$	0.94909	$5.23 \pm 0.67 \pm 1.60$
	0.172	$0.10 \div 0.15$	0.95387	$5.49 \pm 0.55 \pm 1.68$
	0.190	$0.05 \div 0.10$	0.95732	$4.79 \pm 0.59 \pm 1.47$
	0.206	$-0.05 \div 0.05$	0.96055	$5.33 \pm 0.66 \pm 1.63$

Table B.4: *Centrality 15-30%. Final results on particle yields in Au+Au collisions at 62.4 GeV after acceptance, efficiency and background corrections.*

Particle ID	$< p_T >$ $[GeV/c]$	Δy	$< m_T >$ $[GeV/c^2]$	$Y \pm$ *stat. err.* $\pm$ *syst. err.* $[c^2/GeV^2]$
$(\pi^+ + \pi^-)$	0.031	$0.30 \div 0.40$	0.14300	$731.7 \pm 56.2 \pm 151.5$
	0.044	$0.20 \div 0.30$	0.14620	$593.9 \pm 23.4 \pm 122.9$
	0.048	$0.10 \div 0.20$	0.14774	$709.4 \pm 28.0 \pm 146.8$
	0.053	$-0.10 \div 0.10$	0.14924	$721.2 \pm 30.3 \pm 149.3$
$K^+ + K^-$	0.096	$0.15 \div 0.25$	0.50298	$24.0 \pm 2.2 \pm 4.9$
	0.116	$0.10 \div 0.15$	0.50709	$22.3 \pm 2.7 \pm 4.5$
	0.123	$0.05 \div 0.10$	0.50875	$27.2 \pm 3.6 \pm 5.5$
	0.128	$-0.05 \div 0.05$	0.51007	$32.1 \pm 3.8 \pm 6.5$
$p + \overline{p}$	0.143	$0.15 \div 0.20$	0.94909	$3.72 \pm 0.48 \pm 1.14$
	0.172	$0.10 \div 0.15$	0.95387	$4.00 \pm 0.42 \pm 1.22$
	0.190	$0.05 \div 0.10$	0.95732	$3.68 \pm 0.50 \pm 1.13$
	0.206	$-0.05 \div 0.05$	0.96055	$3.06 \pm 0.47 \pm 0.94$

Table B.5: *Centrality 30-50%. Final results on particle yields in Au+Au collisions at 62.4 GeV after acceptance, efficiency and background corrections.*

Particle ID	$< p_T >$ $[GeV/c]$	Δy	$< m_T >$ $[GeV/c^2]$	$Y \pm$ *stat. err.* $\pm$ *syst. err.* $[c^2/GeV^2]$
$(\pi^+ + \pi^-)$	0.031	$0.30 \div 0.40$	0.14300	$341.9 \pm 33.7 \pm 60.5$
	0.044	$0.20 \div 0.30$	0.14620	$317.1 \pm 14.4 \pm 56.1$
	0.048	$0.10 \div 0.20$	0.14774	$342.3 \pm 16.7 \pm 60.6$
	0.053	$-0.10 \div 0.10$	0.14924	$378.9 \pm 18.9 \pm 67.1$
$K^+ + K^-$	0.096	$0.15 \div 0.25$	0.50298	$11.7 \pm 1.3 \pm 2.4$
	0.116	$0.10 \div 0.15$	0.50709	$13.6 \pm 2.0 \pm 2.8$
	0.123	$0.05 \div 0.10$	0.50875	$17.0 \pm 2.4 \pm 3.5$
	0.128	$-0.05 \div 0.05$	0.51007	$12.9 \pm 2.1 \pm 2.6$
$p + \overline{p}$	0.143	$0.15 \div 0.20$	0.94909	$1.91 \pm 0.33 \pm 0.88$
	0.172	$0.10 \div 0.15$	0.95387	$1.40 \pm 0.23 \pm 0.65$
	0.190	$0.05 \div 0.10$	0.95732	$1.89 \pm 0.33 \pm 0.87$
	0.206	$-0.05 \div 0.05$	0.96055	$1.89 \pm 0.35 \pm 0.87$

Bibliography

[1] J. W. Harris and B. Müller, Ann. Rev. Nucl. Part. Sci. **46** (1996) 71.
[2] B. B. Back, (A. Trzupek), *et al.*, Nucl. Phys. **A757** (2005) 28.
[3] B. B. Back, (A. Trzupek), *et al.*, Nucl. Inst. Meth. **A499** (2003) 603.
[4] M. Adamczyk, *et al.*, Nucl. Inst. Meth. **A499** (2003) 437.
[5] K. Adcox, *et al.*, Nucl. Inst. Meth. **A499** (2003) 469.
[6] K. H. Ackermann *et al.*, Nucl. Inst. Meth. **A499** (2003) 624.
[7] B. B. Back, (A. Trzupek), *et al.* Phys. Lett. **B578** (2004) 297.
[8] I. Arsene, *et al.*, Phys. Rev. Lett. **91** (2003) 072305.
[9] K. Adcox, *et al.*, Phys. Rev. Lett. **88** (2002) 022301.
[10] S. S. Adler, *et al.*, Phys. Rev. **C69** (2004) 034910.
[11] J. Adams, *et al.*, Phys. Rev. Lett. **91** (2003) 172302.
[12] B. B. Back, (A. Trzupek), *et al.*, Phys. Rev. Lett. **91** (2003) 072302.
[13] S. S. Adler, *et al.*, Phys. Rev. Lett. **91** (2003) 072303.
[14] J. Adams, *et al.*, Phys. Rev. Lett. **91** (2003) 072304.
[15] S. S. Adler, *et al.*, Phys. Rev. Lett. **97** (2006) 052301.
[16] C. Adler, *et al.*, Phys. Rev. Lett. **90** (2003) 032301.
[17] C. Adler, *et al.*, Phys. Rev. Lett. **90** (2003) 082302.
[18] J. Adams, *et al.*, Phys. Rev. Lett. **93** (2004) 252301.
[19] B. B. Back, (A. Trzupek), *et al.*, Phys. Rev. **C72** (2005) 051901(R).
[20] B. B. Back, (A. Trzupek), *et al.*, Phys. Rev. Lett. **94** (2005) 122303.
[21] H. Ito, *et al.*, Nucl. Phys. **A774** (2006) 519.
[22] S. S. Adler, *et al.*, Phys. Rev. Lett. **91** (2003) 182301.
[23] J. Adams, *et al.*, Phys. Rev. **C72** (2005) 014904.
[24] E. Shuryak, Nucl. Phys. **A774** (2006) 387.
[25] M. J. Tannenbaum, Rep. Prog. Phys. **69** (2006) 2005 [nucl-ex/0603003].
[26] W. Busza, in Particle Production in Highly Excited Matter, H. H. Gutbrod, J. Rafelski, eds., (Plenum Press, Proceedings of a NATO Advanced Study Institute on Particle Production in Highly Excited Matter, 1993) p. 149.
[27] B. B. Back, (A. Trzupek), *et al.*, Phys. Rev. **C70** (2004) 051901(R).
[28] B. Wosiek, (A. Trzupek), *et al.* Nucl. Phys. **A715** (2003) 510c.
[29] A. Trzupek, *et al.*, Eur. Phys. J. **C33** (2004) S600.
[30] A. Trzupek, *et al.*, Nucl. Phys. **A774** (2006) 469.
[31] B. B. Back, (A. Trzupek), *et al.*, nucl-ex/0610001, accepted for publication

in Phys. Rev. C.
[32] E. Schnedermann, J. Sollfrank and U. Heinz, Phys. Rev. **C48** (1993) 2462.
[33] E. Schnedermann and U. Heinz, Phys. Rev. **C50** (1994) 1675.
[34] G. I. Veres, (A. Trzupek), *et al.*, J. Phys., **G30** (2004) S93.
[35] M. Gell-Mann and Y. Ne'eman, *"The Eightfold Way"*, Benjamin, 1964,
[36] R. K. Ellis, *et al.*, *"QCD and Collider Physics"* (Cambridge 1996); http://pdg.lbl.gov/2005/reviews/qcdrpp.pdf.
[37] R. P. Feynman and A. R. Hibbs, *"Quantum Physics and Path Integrals"*, New York: McGraw-Hill, 1965 [ISBN 0-070-20650-3].
[38] K. G. Wilson, Phys. Rev. **D10** (1974) 2445.
[39] F. Karsch, Lect. Notes Phys. **583** (2002) 209.
[40] F. Karsch, E. Laermann and A. Peikert, Phys. Lett. **B478** (2000) 447.
[41] F. Karsch, to be published in Quark Matter 2006 proceedings.
[42] D. J. Gross and F. Wilczek, Phys. Rev. Lett. **30** (1973) 1343.
[43] H. D. Politzer, Phys. Rev. Lett. **30** (1973) 1346.
[44] S. Bethke, J. Phys. **G26** (2000) R 27; S. Bethke, hep-ex/0407021.
[45] V. Koch, Int. J. Mod. Phys. **E6** (1997) 203-250 [nucl-th/9706075].
[46] J. Goldstone, A. Salam and S. Weinberg, Phys. Rev. **127** (1962) 965.
[47] E. Shuryak, Nucl. Phys. Rep. **61** (1980) 71.
[48] J. C. Collins and M. J. Perry, Phys. Rev. Lett. **34** (1975) 1353.
[49] N. Cabibbo and G. Parisi, Phys. Lett. **B59** (1975) 67.
[50] Z. Fodor and S. D. Katz, JHEP **0404** (2004) 050 [hep-lat/0402006].
[51] K. Rajagopal and F. Wilczek, hep-ph/0011333.
[52] S. Reddy, J. Phys. **G30** (2004) S879;
[53] B. Müller and J. Rafelski, Phys. Rev. Lett. **48** (1982) 1066.
[54] D. K. Srivastava, Eur. Phys. J. **C10** (1999) 487.
[55] R. Pisarski, Phys. Lett. **B110** (1982) 155,
[56] T. Matsui and H. Satz, Phys. Lett. **B178** (1986) 416.
[57] J. P. Blaizot and A. Krzywicki, Acta Phys. Pol. **B27** (1996) 1687.
[58] J. Bjorken, Acta Phys. Pol. **B28** (1997) 2773.
[59] T. C. Petersen and J. Randrup, Phys. Rev. **C61** (2000) 024906.
[60] J. G. Cramer, G. A. Miller, Jackson M. S. Wu and Jin-Hee Yoon, Phys. Rev. Lett. **94** (2005) 102302 and Erratum: Phys. Rev. Lett. **95** (2005) 139901(E).
[61] H. Heiselberg and A-M. Levy, Phys. Rev. **C59** (1999) 2716.
[62] I. G. Bearden, *et al.*, Phys. Rev. Lett. **11** (1997) 2080.
[63] T. Csörgo and B. Lörstad, Phys. Rev. **C54** (1996) 1390.
[64] M. van Leeuwen, *et al.*, Nucl. Phys. **A715** (2003) 161c.
[65] I. Arsene *et al.*, Phys. Rev. **C72** (2005) 014908.
[66] S. S. Adler, *et al.*, Phys. Rev. **C69** (2004) 034909.
[67] J. Adams *et al.*, Phys. Rev. Lett. **92** (2004) 112301.
[68] A. Baran, W. Broniowski and W. Florkowski, Acta Phys. Pol. **B35** (2004) 779.

[69] U. Heinz and P. Kolb, Nucl. Phys. **A702** (2002) 269.
[70] P. Kolb and R. Rapp, Phys. Rev. **C67** (2003) 044903.
[71] M. A. Braun, F. del Moral and C. Pajares, Nucl. Phys. **A715** (2003) 791.
[72] J. Schaffner-Bielich, D. Kharzeev, L. McLerran and R. Venugopalan, Nucl. Phys. **A705** (2002) 494.
[73] H. Sorge, Phys. Rev. **C52** (1995) 3291.
[74] X. N. Wang and M. Gyulassy, Phys. Rev. Lett. **68** (1992) 1480.
[75] L. D. McLerran and R. Venugopalan, Phys. Rev. **D49** (1994) 2233; Phys. Rev. **D50** (1994) 2225; Phys. Rev. **D50** (1994) 3352.
[76] A. De Rujula, S. L. Glashow, H. D. Politzer, S. B. Treiman, F. Wilczek and A. Zee, Phys. Rev. **D10** (1974) 1649.
[77] K. Long, R. Nisius and W. L. Stirling, hep-ph/0109092.
[78] L. V. Gribov, E. M. Levin and M. G. Ryskin, Phys. Rep. **100** (1983) 1.
[79] K. Golec-Biernat, Acta Phys. Pol. **B35** (2004) 3103.
[80] L. Ahle, *et al.*, Phys. Rev. **C57** (1998) R466; L. Ahle, *et al.*, Phys. Rev. Lett. **81** (1998) 2650.
[81] L. Ahle, *et al.*, Phys. Rev. **C60** (1999) 064901.
[82] I. G. Bearden, *et al.*, Phys. Lett. **B388** (1996) 431.
[83] H. Appelshäeuser, *et al.*, Phys. Rev. Lett. **82** (1999) 2471.
[84] F. Siklér, *et al.*, Nucl. Phys. **A661** (1999) 45.
[85] For a review, see H. Satz, Nucl. Phys. **A715** (2003) 3c.
[86] W. Retyk, *et al.*, J. Phys. **G23** (1997) 1845; I. Bearden, *et al.*, Phys. Lett. **B471** (1999) 6; K. Fanebust *et al.*, J. Phys. **G28** (2002) 1607.
[87] M. C. Abreu, *et al.*, Phys. Lett. **B477** (2000) 28.
[88] M. M. Aggarwal, *et al.*, Phys. Rev. Lett. **85** (2000) 3595.
[89] G. Agakichiev, *et al.*, Phys. Rev. Lett. **75** (1995) 1272; G. Agakichiev, *et al.*, Phys. Lett. **B422** (1998) 405; B. Lenkeit, *et al.*, Nucl. Phys. **A661** (1999) 23c; H. Appelshaeuser, *et al.*, Nucl. Phys. **A698** (2002) 253.
[90] M. C. Abreu, *et al.*, Eur. Phys. J. **C14** (2000) 443.
[91] P. Braun-Munzinger, I. Heppe, J. Stachel, Phys. Lett. **B465** (1999) 15; P. Braun-Munzinger, K. Redlich and J. Stachel, nucl-th/0304013.
[92] M. Gaździcki, *et al.*, J. Phys. **G30** (2004) S710.
[93] M. Gaździcki and M. Gorenstein, Acta Phys. Pol. **B30** (1999) 2705.
[94] E. L. Bratkovskaya, *et al.*, Phys. Rev. **C69** (2004) 054907.
[95] J. Cleymans and K. Redlich, Phys. Rev. **C60** (1999) 054908.
[96] M. Jacob, U. Heinz, nucl-th/0002042.
[97] N. Armesto, A. Capella, E. G. Ferreiro, A. Kaidalov and D. Sousa, Nucl. Phys. **A698** (2002) 583c.
[98] D. Zschiesche, *et al.*, Nucl. Phys. **A681** (2001) 34c; H. Stcker, *et al.*, AIP Conference Proceedings, **Vol. 631** (2002) p. 553.
[99] http://www.bnl.gov/rhic.
[100] I. Arsene *et al.*, Nucl. Phys. **A757** (2005) 1.

[101] K. Adcox, *et al.*, Nucl. Phys. **A757** (2005) 184.
[102] J. Adams, *et al.*, Nucl. Phys. **A757** (2005) 102.
[103] (PHOBOS Collab.), "A Letter of Intent to Study Very Low p_T Phenomena at RHIC", 1993.
[104] (PHOBOS Collab.), "Proposal to Study Very Low p_T Phenomena at RHIC", 1993.
[105] (PHOBOS Collab.), "PHOBOS Detector Conceptual Design", Conceptual Design Report (CDR), 1994.
[106] K. Woźniak, (A. Trzupek), *et al.*, Nucl. Inst. and Meth. **A566** (2006) 185.
[107] A. Białas, B. Bleszyński and W. Czyż, Nucl. Phys. **B111** (1976) 461.
[108] B. B. Back, (A. Trzupek), *et al.*, Phys. Rev. **C65** (2002) 031901(R).
[109] J. Katzy, (A. Trzupek), *et al.*, Nucl. Phys. **A698** (2002) 555.
[110] M. Gyulassy and X. N. Wang, Phys. Rev. **D44** (1991) 3501.
[111] GEANT 3.2.1, CERN Program Library.
[112] B. B. Back, (A. Trzupek), *et al.*, Phys. Rev. Lett. **91** (2003) 052303.
[113] S. Edelman, *et al.*, Phys. Lett. **B592** (2004) 1.
[114] B. B. Back, (A. Trzupek), *et al.*, Phys. Rev. **C67** (2003) 021901(R).
[115] B. Andersson, G. Gustafson and B. Nilsson-Almqvist, Nucl. Phys. **B281** (1987) 289.
[116] T. Sjöstrand, Comput. Phys. Commun. **82** (1992) 15.
[117] K. J. Eskola, V. J. Kolhinen and C. A. Salgado, Eur. Phys. J. **C9** (1999) 61.
[118] Z. W. Lin, *et al.*, Phys. Rev. **C64** (2001) 011902; B. Zhang, *et al.*, Phys. Rev. **C61** (2000) 067901.
[119] Bao-An Li and Che Ming Ko, Phys. Rev. **C52** (1995) 2037.
[120] S. A. Bass, *et al.*, Prog. Part. Nucl. Phys. **41** (1998) 225 [nucl-th/9803035].
[121] B. Andersson, G. Gustafson, G. Ingelman and T. Sjöstrand, Phys. Rep. **97** (1983) 31; T. Sjöstrand, Comput. Phys. Commun. **39** (1986) 347.
[122] http://physics.nist.gov/PhysRefData/Star/Text/PSTAR.html.
[123] ICRU (International Commission on Radiation Units and Measurements) Report 49, Stopping Powers and Ranges for Protons and Alpha Particles, (1993).
[124] G. I. Veres, (A. Trzupek), *et al.*, J. Phys. **G30** (2004) S1143-S1147.
[125] B. B. Back, (A. Trzupek), *et al.*, Phys. Rev. Lett. **87** (2001) 102301.
[126] K. Adcox, *et al.*, Phys. Rev. Lett. **89** (2002) 092302.
[127] B. B. Back, (A. Trzupek), *et al.*, Phys. Rev. Lett. **94** (2005) 082304.
[128] D. Prorok, Phys. Rev. **C73** (2006) 064901.
[129] K. J. Eskola, H. Honkanen, H. Niemi, P. V. Ruuskanen and S. S. Rasanen, Phys. Rev. **C72** (2005) 044904.
[130] J. Dias de Deus, E. G. Ferreiro, C. Pajares and R. Ugoccioni, Eur. Phys. J. **C40** (2005) 229.
[131] F. Cooper and G. Frye, Phys. Rev. **D10** (1974) 186.

[132] W. Broniowski and W. Florkowski, Phys. Rev. Lett. **87** (2001) 272302.
[133] W. Broniowski and W. Florkowski, A. Kisiel and T. Tałuć, Comput. Phys. Commun. **174** (2006) 669.
[134] B. B. Back, (A. Trzupek), *et al.*, nucl-ex/0506008, J.G. Cramer, 2005, (private communication).
[135] C. Adler, *et al.*, Phys. Rev. Lett. **87** (2001) 082301.
[136] K. Adcox, *et al.*, Phys. Rev. Lett. **88** (2002) 192302.
[137] B. B. Back, (A. Trzupek), *et al.*, Phys. Rev. **C73** (2006) 031901.
[138] D. Magestro, *et al.*, J. Phys. **G28** (2002) 1745.
[139] F. Becattini, J. Cleymans, A. Keränen, K. Redlich and E. Suhonen Phys. Rev. **C64** (2001) 024901.
[140] L. Ahle, *et al.*, Phys. Lett. **B490** (2000) 53.
[141] J. P. Boymond, J. W. Cronin, H. J. Frisch, P. A. Piroué, M. J. Shochet and R. L. Sumner, Phys. Rev. **D11** (1975) 3105.
[142] D. Antreasyan, J. W. Cronin, H. J. Frisch, L. Kluberg, P. A. Piroué, M. J. Shochet and R. L. Sumner, Phys. Rev. **D19** (1979) 764.
[143] C. Albajar, *et al.*, Nucl. Phys. **B335** (1990) 261.
[144] D. d'Enterria, Phys. Lett. **B596** (2004) 32.
[145] M. Shimomura, *et al.*, Nucl. Phys. **A774** (2006) 457.
[146] K. Gallmeister, C. Greiner and Z. Xu, Phys. Rev. **C67** (2003) 044905.
[147] I. Vitev and M. Gyulassy, Phys. Rev. Lett. **89** (2002) 252301; I. Vitev, Phys. Lett. **B562** (2003) 36.
[148] D. Kharzeev, E. Levin and L. McLerran, Phys. Lett. **B561** (2003) 93.
[149] A. Accardi, hep-ph/0212148.
[150] A. Accardi, Acta Phys. Hung. **A22** (2005) 289.
[151] M. M. Aggarwal, *et al.*, Eur. Phys. J. **C23** (2002) 225; M. M. Aggarwal, *et al.*, Phys. Rev. Lett. **81** (1998) 4087, Erratum-ibid. **84** (2000) 578.
[152] X-N. Wang, Phys. Rev. Lett. **81** (1998) 2655; X-N. Wang, Phys. Rev. **C61** (2000) 064910; E. Wang and X.-N. Wang, Phys. Rev. **C64** (2001) 034901.
[153] S. S. Adler, *et al.*, Phys. Rev. Lett. **91** (2003) 072301.
[154] A. Breakstone, *et al.*, Z. Phys. **C69** (1995) 55; D. Drijard *et al.*, Nucl. Phys. **B208** (1982) 1.
[155] J. D. Bjorken, Phys. Rev. **D27** (1983) 140.
[156] A. Bazilevsky, *et al.*, Nucl. Phys. **A715** (2003) 486c; K. Adox, *et al.*, Phys. Rev. Lett. **87** (2001) 052301.
[157] T. Alber, *et al.*, Phys. Rev. Lett. **75** (1995) 3814.
[158] B. B. Back, (A. Trzupek), *et al.*, Phys. Rev. **C72** (2005) 051901(R).
[159] B. B. Back, (A. Trzupek), *et al.*, Phys. Rev. Lett. **94** (2005) 122303.
[160] P. Huovinen, private communication; P. F. Kolb, P. Huovinen, U. W. Heinz and H. Heiselberg, Phys. Lett. **B500** (2001) 232.
[161] P. F. Kolb and U. Heinz, nucl-th/0305084.